

ABSTRACT

Title of dissertation:

DIRECT NUMERICAL SIMULATION OF
INCOMPRESSIBLE MULTIPHASE FLOW
WITH PHASE CHANGE

Moon Soo Lee, Doctor of Philosophy, 2015

Dissertation directed by:

Professor Amir Riaz
Department of Mechanical Engineering

Phase change problems arise in many practical applications such as air-conditioning and refrigeration, thermal energy storage systems and thermal management of electronic devices. The physical phenomenon in such applications are complex and are often difficult to be studied in detail with the help of only experimental techniques. The efforts to improve computational techniques for analyzing two-phase flow problems with phase change are therefore gaining momentum.

The development of numerical methods for multiphase flow has been motivated generally by the need to account more accurately for (a) large topological changes such as phase breakup and merging, (b) sharp representation of the interface and its discontinuous properties and (c) accurate and mass conserving motion of the interface. In addition to these considerations, numerical simulation of multiphase flow with phase change introduces additional challenges related to discontinuities in the velocity and the temperature fields. Moreover, the velocity field is no longer divergence free. For phase change problems, the focus of developmental

efforts has thus been on numerically attaining a proper conservation of energy across the interface in addition to the accurate treatment of fluxes of mass and momentum conservation as well as the associated interface advection.

Among the initial efforts related to the simulation of bubble growth in film boiling applications the work in [1] was based on the interface tracking method using a moving unstructured mesh. That study considered moderate interfacial deformations. A similar problem was subsequently studied using moving, boundary fitted grids [2], again for regimes of relatively small topological changes. A hybrid interface tracking method with a moving interface grid overlapping a static Eulerian grid was developed [3] for the computation of a range of phase change problems including, three-dimensional film boiling [4], multimode two-dimensional pool boiling [5] and film boiling on horizontal cylinders [6]. The handling of interface merging and pinch off however remains a challenge with methods that explicitly track the interface. As large topological changes are crucial for phase change problems, attention has turned in recent years to front capturing methods utilizing implicit interfaces that are more effective in treating complex interface deformations.

The VOF (Volume of Fluid) method was adopted in [7] to simulate the one-dimensional Stefan problem and the two-dimensional film boiling problem. The approach employed a specific model for mass transfer across the interface involving a mass source term within cells containing the interface. This VOF based approach was further coupled with the level set method in [8], employing a smeared-out Heaviside function to avoid the numerical instability related to the source term. The coupled level set, volume of fluid method and the diffused interface approach was used for film boiling with water and R134a at the near critical pressure

condition [9]. The effect of superheat and saturation pressure on the frequency of bubble formation were analyzed with this approach. The work in [10] used the ghost fluid and the level set methods for phase change simulations. A similar approach was adopted in [11] to study various boiling problems including three-dimensional film boiling on a horizontal cylinder, nucleate boiling in microcavity [12] and flow boiling in a finned microchannel [13]. The work in [14] also used the ghost fluid method and proposed an improved algorithm based on enforcing continuity and divergence-free condition for the extended velocity field. The work in [15] employed a multiphase model based on volume fraction with interface sharpening scheme and derived a phase change model based on local interface area and mass flux.

Among the front capturing methods, sharp interface methods have been found to be particularly effective both for implementing sharp jumps and for resolving the interfacial velocity field. However, sharp velocity jumps render the solution susceptible to erroneous oscillations in pressure and also lead to spurious interface velocities. To implement phase change, the work in [16] employed point mass source terms derived from a physical basis for the evaporating mass flux. To avoid numerical instability, the authors smeared the mass source by solving a pseudo time-step diffusion equation. This measure however led to mass conservation issues due to non-symmetric integration over the distributed mass source region. The problem of spurious pressure oscillations related to point mass sources was also investigated by [17]. Although their method is based on the VOF, the large pressure peaks associated with sharp mass source was observed to be similar to that for the interface tracking method. Such spurious fluctuation in pressure are essentially undesirable because the effect is globally

transmitted in incompressible flow. Hence, the pressure field formation due to phase change need to be implemented with greater accuracy than is reported in current literature.

The accuracy of interface advection in the presence of interfacial mass flux (mass flux conservation) has been discussed in [14, 18]. The authors found that the method of extending one phase velocity to entire domain suggested by Nguyen et al. in [19] suffers from a lack of mass flux conservation when the density difference is high. To improve the solution, the authors impose a divergence-free condition for the extended velocity field by solving a constant coefficient Poisson equation. The approach has shown good results with enclosed bubble or droplet but is not general for more complex flow and requires additional solution of the linear system of equations.

In current thesis, an improved approach that addresses both the numerical oscillation of pressure and the spurious interface velocity field is presented by featuring (i) continuous velocity and density fields within a thin interfacial region and (ii) temporal velocity correction steps to avoid unphysical pressure source term. Also I propose a general (iii) mass flux projection correction for improved mass flux conservation. The pressure and the temperature gradient jump condition are treated sharply. A series of one-dimensional and two-dimensional problems are solved to verify the performance of the new algorithm. Two-dimensional and cylindrical film boiling problems are also demonstrated and show good qualitative agreement with the experimental observations and heat transfer correlations. Finally, a study on Taylor bubble flow with heat transfer and phase change in a small vertical tube in axisymmetric coordinates is carried out using the new multiphase, phase change method.

DIRECT NUMERICAL SIMULATION OF
INCOMPRESSIBLE MULTIPHASE FLOW WITH PHASE CHANGE

by

Moon Soo Lee

Dissertation submitted to the Faculty of the Graduate School of the
University of Maryland, College Park in partial fulfillment
of the requirements for the degree of
Doctor of Philosophy
2015

Advisory Committee:

Prof. Amir Riaz (Advisor)

Prof. Reinhard Radermacher (Co-advisor)

Prof. Yunho Hwang

Prof. Bao Yang

Prof. James Baeder

© Copyright by
Moon Soo Lee
2015

Dedicated

To my parents

Cheol Won Lee and Hae Ja Kim

To my sister

Sang Hyun Lee

Thank you for your love and prayers.

Acknowledgments

The completion of this thesis would not have been possible without the guidance and support from many people. I would first like express my sincere gratitude my advisor, Professor Amir Riaz, for his tremendous assistance with my research and guidance in overcoming numerous obstacles during my graduate study. He has always been open to new ideas and gave me invaluable insights into many numerical and physical aspects of two-phase flows. I am also very grateful to my co-advisor, Professor Reinhard Radermacher, for his continuous support. He has been extremely patient throughout the course of my doctoral study and been considerate for the long-term effort. I would like to thank Professor Yunho Hwang for helping me through one of the projects that I have work on for a year in CEEE. He has also shown a great deal of care and interest in my Ph.D. dissertation as well and offered many constructive advices. I am very thankful to the other members of my committee, Professor Bao Yang and Professor James Baeder, for the time and efforts in reviewing this dissertation. In addition to my committee members, I would like to thank Dr. Vikrant Aute from whom I have been guided the most during my first two years in the Ph.D. program. He and the other members in CEEE have not only given me many opportunities to improve my research and presentation skills but also widen my perspective in the application of numerical heat transfer.

My life in Maryland has been enriched by many friends and colleagues without whom it would not have been the same. I would like to thank Dr. Hoseong Lee for being a mentor and a friend. He was like an older brother to me. My many colleagues, Zohreh Ghorbani,

Abishek Gopal, Don Daniel, Nils Tilton, Zhipeng Qin, Mohammad Alizadeh Nomeli, Long Huang, Hongtao Qiao and Daniel Bacellar deserve my deepest gratitude for many useful discussions and brainstormings, but even more for sharing the difficulties in graduate life and for their friendship. I thank all my Korean friends, some of whom have already left and some of whom are still here. Because of them, I have felt home and not alone here in Maryland. I cannot finish this section without thanking my family for their love and prayers from thousands of miles away, and God whom I believe.

Contents

1	Introduction	1
1.1	Motivation	1
1.2	Pool Boiling Regime	2
1.3	Literature Review on Direct Numerical Simulation Method for Two-Phase Flow	5
1.3.1	Volume of Fluid Method	8
1.3.2	Level Set Method	9
1.3.3	On the Interface Jump Capturing Scheme	11
1.3.4	On the Mass Conservation of the Level Set Method	13
1.4	Literature Review on the Numerical Studies of Multiphase Flow with Phase Change	15
1.4.1	Problem Statement for Phase Change Modeling	17
1.5	Research Objectives	18
2	Formulation of Governing Equations	20
2.1	Energy Conservation and Heat Flux	20
2.2	Mass Flux and the Velocity Jump Condition	22
2.3	Momentum Conservation Across Interface	23
2.4	Interface Velocity and Advection	24
2.5	Non-dimensionalization	25
3	Numerical Formulations	26
3.1	Diffused Interface for Velocity Jump Condition	28
3.2	Mass Flux Projection Correction	34
3.3	Asymmetric Interface Diffusion	36
3.4	Velocity Correction for Updated Density Field	37
3.5	Interface Advection and Reinitialization	39

3.6	Discretization of the Energy Equation and the Temperature Gradient Jump Condition	44
3.7	Discretization of the Momentum Equation	46
3.8	Viscous Term	47
3.9	Time Step Size Restrictions	47
3.10	Solution Algorithm	49
4	Verification Cases: One-dimensional Interface and Two-dimensional Bubble	51
4.1	Case 1. One-dimensional Phase Change with Constant Mass Flux	52
4.2	Case 2. One-dimensional Stefan Problem	53
4.3	Case 3. One-dimensional Sucking-interface Problem	54
4.4	Cases 4.1-4.5. Two-dimensional Bubble Phase Change with Constant Mass Flux	58
4.5	Case 5. Two-dimensional Bubble Evaporation in Superheated Liquid	63
4.6	Conclusion	74
5	Validation Cases: Film Boiling	78
5.1	Cases 6.1-6.3. Two-Dimensional Cases	78
5.2	Cases 7.1-7.3. Axisymmetric Cases	83
5.3	Conclusions	103
6	Numerical Study on Taylor Bubble Flow with Heat Transfer and Phase Change	105
6.1	Introduction	105
6.2	Literature Review	106
6.3	Scaling Factors and Dimensionless Parameters	109
6.4	Numerical Methods	110
6.5	Validation with Adiabatic Taylor Bubble Flow in Vertical Tube	112
6.6	Results and Discussion	116

6.6.1	Reference Case	116
6.6.2	Effect of the capillary number	119
6.6.3	Effect of the Reynolds number	121
6.6.4	Effect of the Froude number and Other Parameters	129
6.7	Conclusions	129
7	Conclusions	133
7.1	Summary of Research Contributions	133
7.2	Publications and Presentations	137
7.3	Future Work	138

Nomenclature

Roman Symbols

a, C	Constants
c	Specific heat, J/kgK
C_p	Specific heat at constant pressure, J/kgK
\mathbf{d}	Distance function
D	Diameter, m
\mathbf{g}	Body force, m/s ²
h_{lg}	Latent heat, J/kg
H_ϵ	Heaviside function
k	Thermal conductivity, m ² /s ²
L	Reference length, m
\dot{m}_Γ	Mass flux, kg/m ² s
\mathbf{n}	Interfacial normal vector
N	Mesh size
P	Pressure, Pa
\mathbf{q}	Heat flux, W/m ²
R	Radius, m
R_0	Gas constant, J/kgK
S	Source term
S_r	Sign function
\mathbf{t}	Interfacial tangent vector
T	Temperature, K
\mathbf{u}, u, v	Fluid velocity vector and its components, m/s
\mathbf{u}_Γ	Interface velocity vector, m/s
U_o	Reference velocity, m/s
V	Magnitude of velocity, m/s

x Position vector

Greek Symbols

$\tilde{\beta}$	Smoothed inverse of the density
δ	Boundary layer thickness, m
ϵ	Coefficient for diffused interface thickness, a small positive quantity, error
θ	Angle of mass flux projection, rad
θ_x, θ_y	Subcell grid fraction in x and y -direction
ϑ_l	Dynamic liquid hold-up
κ	Curvature, $1/m$
λ	Reference length for film boiling cases, m
λ_d	Most unstable Taylor wavelength, m
μ	Dynamic viscosity, $\text{Pa}\cdot\text{s}$
ν	Specific volume, m^3/kg
ρ	Density, kg/m^3
σ	Surface tension coefficient, N/m
τ	Deviatoric stress tensor, Pa
τ_r	Fictitious time step
ϕ	Level set function
φ	Kinetic mobility
χ	Evaporation coefficient
Ω	Computational domain

Dimensionless Parameters

α' Thermal diffusivity ratio, $\frac{\alpha_g}{\alpha_l}$

C'_p Specific heat capacity ratio, $\frac{C_{p,g}}{C_{p,l}}$

k' Thermal conductivity ratio, $\frac{k_g}{k_l}$

μ'	Viscosity ratio, $\frac{\mu_g}{\mu_l}$
ρ'	Density ratio, $\frac{\rho_g}{\rho_l}$
Fr	Froude number, $\frac{U_o}{\sqrt{gL}}$
Gr	Grashof number, $\frac{\rho_g(\rho_l - \rho_g)g\lambda^3}{\mu_g^2}$
Nu	Nusselt number, $\frac{qL}{k_l(T_{wall} - T_b)}$
Pr	Prandtl number, $\frac{\mu_l C_{p,l}}{k_l}$
Re	Reynolds number, $\frac{\rho_l U_o L}{\mu_l}$
St	Stefan number, $\frac{C_{p,l}(T_{wall} - T_{sat})}{h_{gl}}$
We	Weber number, $\frac{\rho_l U_o^2 L}{\sigma}$

Subscript

av	Averaged
Γ	Interface
CFL	CourantFriedrichsLewy number
d	Computational domain
g	Gas
in	Inlet
l	Liquid
ln	piecewise linear
max	Maximum
pw	piecewise polynomial
s	Liquid slug
sl	Superficial liquid

sat Saturated fluid

sup Superheated

sub Subcooled

tb Taylor bubble

th Thermal

uc Unit cell

wall Wall

∞ Ambient

Superscript

G Ghost fluid cell

',' Intermediate steps in velocity correction scheme

*** Intermediate step in projection method

Acronym

CFL CourantFriedrichsLewy

CICSAM Compressive Interface Capturing Scheme for Arbitrary Meshes

CLSVOF Coupled Level-Set and Volume Of Fluid

CSF Continuum Surface Force model

DGFM/MPCC Diffused interface with Ghost Fluid Method / Mass flux Projection Correction with Curvature

DNS Direct Numerical Simulation

ENO Essentially Non-Oscillatory

HF Height Function

HPLS Hybrid ParticleLevel Set method

LSM Level Set Method

MAC Marker-And-Cell method

PARDISO a parallel direct sparse solver interface

PDE Partial Differential Equation

SDI Simple Diffused Interface

SGFM Sharp Ghost Fluid Method

SURFER VOF based method with surface tension

VOF Volume Of Fluid method

WENO Weighted Essentially Non-Oscillatory

1 Introduction

1.1 Motivation

Multiphase flow (e.g., gas and liquid or oil and refrigerant) and phase change (evaporation or condensation) problems arise in many thermal engineering fields such as in air-conditioning and refrigeration industries, thermal energy storage systems, electronics heat management and cryogenic fluid flow to name a few. The primary motivation for studying flow involving phase change comes from the fact that it is one of the most effective means of heat transfer. Phase changing also occurs as an essential stage of manufacturing processes such as quenching of metals. In many situations, phase change can lead to engineering anomalies, for instance, degradation of performance and efficiency in the flow and mal-distribution of pressure within heat exchangers and water droplet formation and retention on fin surfaces.

However, much of the hydrodynamics and heat transfer aspects of two-phase flows and phase change are still not well known. The analysis of such flows is often quite complicated because of different modes of boiling and interaction with solid surface that affects the overall heat transfer rate as understood on the basis of studied by analytical or experimental methods. Engineering applications rely on empirical correlations developed for specific operating conditions. On the other hand, the advancement in modern heat exchanger designs involve new operating conditions that do not fall within the range of validity associated with existing correlations. Attempts to come up with more general mechanistic models exist for alleviating the dependence on empirical correlation but has had limited success.

At the same time, the use of computational fluid dynamics has been gaining popularity in the analysis of these phenomenon due to advancements in computational power and concerted efforts made in the development of new numerical methods over the past few decades. Specific simulation methods have been developed to account for different situations. For example,

one of the simplest models of multiphase flow is based on the assumption of a homogeneously dispersed phase with constant bubble or droplet size and a local equilibrium condition. This assumption is very useful under the high flow rate condition. However, many cases of the multiphase flows with phase change exhibit distinctive phase boundaries that arbitrarily deform and undergo topology changes, and a direct numerical simulation (DNS) is needed to resolve the complete interfacial physics. The DNS methods for multiphase flow aim to consider (a) large topological changes such as phase breakup and merging, (b) sharp representation of the interface and its discontinuous properties and (c) accurate and mass conserving motions of the interface. In addition to the challenges faced by the multiphase flow, the phase change introduces the need to account for discontinuities related to the velocity field and the temperature field. Moreover, the motion of the interface can no longer be described by a divergence free fluid velocity field. Thus, the focus of phase change scheme has been on (a) the calculation of the energy balance across the interface, (b) the implementation of the mass flux in the mass and momentum conservation equations and (c) the corresponding interface advection.

DNS of multiphase flow and phase change has received considerable attention and has become a powerful approach to study and understand the fundamental physics of flow and heat transfer involving droplets and films. However, limitations still exist in the capability of computational methods that makes it difficult to address a wide range of practical applications. In this thesis, I will explore the critical aspects of the direct numerical simulation methods for phase change simulation and propose improved methods that can assist the robustness of simulation as well as the accuracy of the solution.

1.2 Pool Boiling Regime

Boiling occurs in refrigeration evaporators, either in a flooded evaporator with low fluid velocity or in a dry expansion shell-and-tube evaporator with considerable fluid flow. For

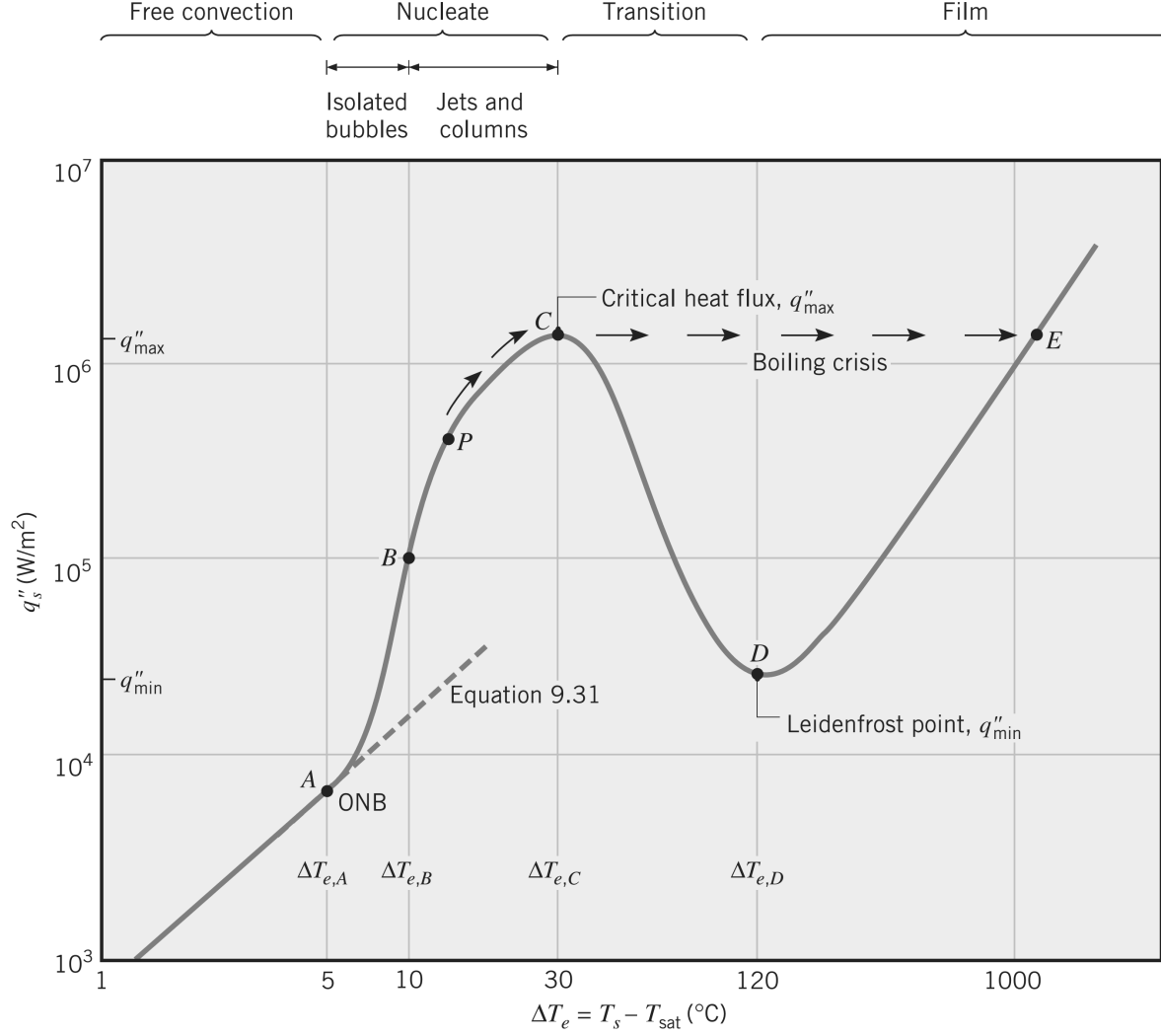


Figure 1: Characteristic boiling curve for water at 1 atm. [20]

both natural convection and forced flow, the boiling characteristics depend on thermodynamic, transport and material properties of the heated surface(roughness and wettability). One of the most basic mode of boiling heat transfer is the pool boiling and its regimes are described using the characteristic boiling curve as shown in Fig. 1. The first region until point (A) refers to heat transfer by convection and evaporation of superheated liquid at the free surface. When the surface temperature exceeds the saturation temperature by a few degrees, nucleate boiling initiates. As the temperature increases further, the number of nucleation sites increases due to the formation of thin superheated liquid films, resulting in

more bubbles. Beyond point (B), the higher density and frequency of bubbles leads to their close interaction such that they merge to form vapor columns and slugs that degrades the liquid contact with the heated surface thus decreasing the slope of the boiling curve. This eventually leads to the critical (maximum) heat flux (C) where the vapor bubbles eventually cover the entire surface area. The maximum heat flux is called the burnout heat flux because further increases in the heat flux past this point creates a jump in the temperature difference and reaches point (E) causing melting of the heating material. When the temperature is allowed to exceed the maximum heat flux point, the heat flux starts to decrease due to the formation of a vapor film which substantially increases thermal resistance. This unstable regime is called the transitional boiling regime. When the temperature is increased even further, past point (D), a stable vapor film is formed and the heat flux rises again due to conduction and radiation but the heat flux in this film boiling region is much lower than the nucleate boiling region.

The fact that the nucleate boiling regime exhibits the highest heat transfer coefficient at a relatively low temperature, has led to a broad interest in its detailed analysis. However the physical mechanism of nucleate boiling is quite complex due to its dependence on the properties of the heated surface. Specifically, nucleate boiling depends on the number, shape and surface roughness of the nucleation sites which are microscopic cavities or crevices where air can be trapped. Nucleation sites are also formed from spots with lower wettability. These nucleation sites provide a free gas-liquid interface through which the superheated liquid can evaporate. Due to the complexity, both the empirical and the mechanistic models have not been able to provide accurate predictions for general conditions.

The transitional boiling regime is fundamentally unstable and the phenomena depends on the history of surface temperature evolution. The irregular contact and dryout of the liquid at the solid surface need to be considered. Consequently, the current understanding of the transitional boiling regime is still limited. The stable film boiling regime is relatively easier to

analyze since the effect of the heated surface is minimal. Thus, correlations and mechanistic models have had the most success in predicting the behavior of film boiling. However, it is more difficult to set up an experiment for study of a single bubble formation. In this study, the film boiling is used to validate the numerical simulations.

1.3 Literature Review on Direct Numerical Simulation Method for Two-Phase Flow

In general, the numerical methods for simulating multiphase flow need to account for the interfacial physics at the scale of continuum mechanics as well as the arbitrary interface deformation and topology changes.

The numerical solution of moving interface in a full Navier-Stokes flow has been proven to be considerably difficult and the development of the DNS multiphase methods has been driven by following aspects that represent the major challenges.

1. Interface deformation and topological changes such as phase breakup and merging.
2. Modeling of the interaction of the liquid-gas interface such as surface tension.
3. Accurate and robust representation of the interfacial discontinuity.
4. Phase change and mass transfer between solid and liquid or solid and gas.
5. Accurate and mass conserving advection of the interface.
6. Contact angle and complex geometry.
7. Computational efficiency.

The multiphase numerical methods can be classified into the Lagrangian type methods, the Eulerian type methods and hybrid methods. In the Lagrangian type methods, the interface

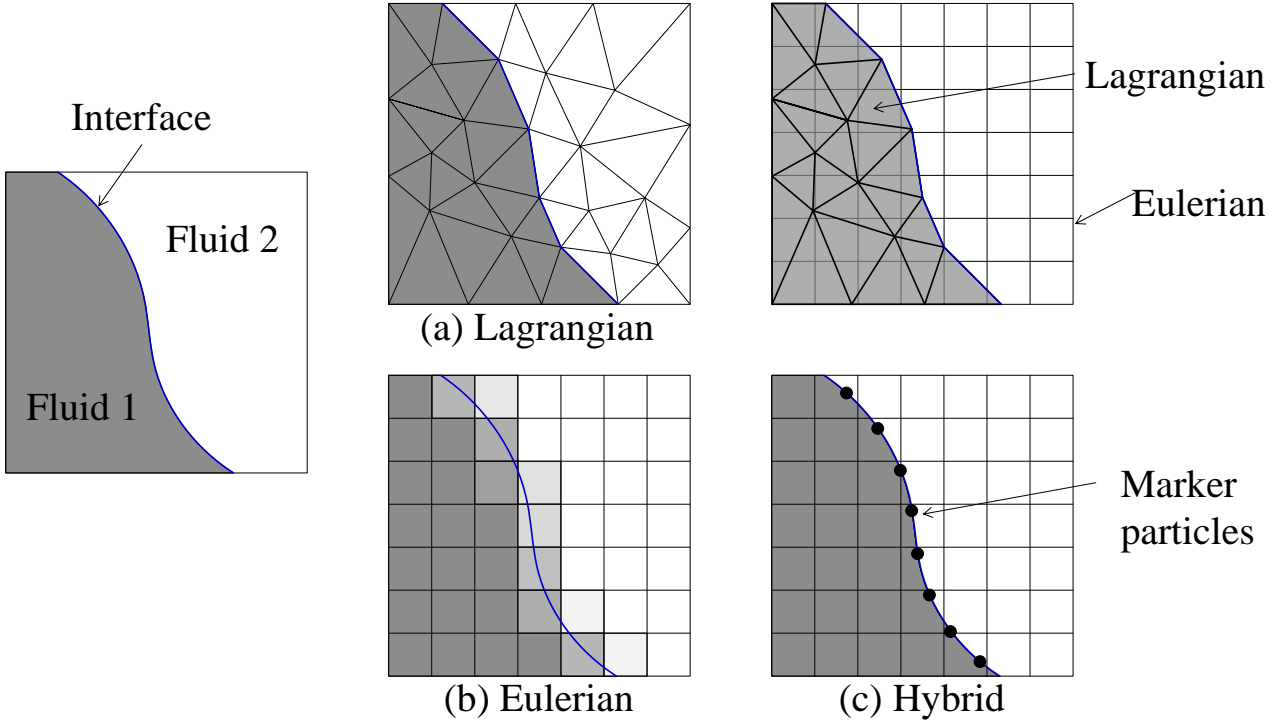


Figure 2: Illustration of (a) Lagrangian type method, (b) Eulerian type method and (c) hybrid method

is explicitly tracked by a computational element, for example, moving girds or markers cells. Fig. 2 (a) gives an illustration of a Lagrangian grid for a phase interface. The main advantage of this type of method is the accuracy in locating the interface position and the absence of numerical error in representing the interface dynamics and the phase boundary condition. One of the most accurate methods was presented by Ryskin and Leal [21, 22, 23] using boundary fitted, curvilinear grids for each phase to study the deformation of a steady rising bubble. A similar approach where the grid follows the fluid is shown in the work of Oran and Bois [24] and Feng [25]. Another form of Lagrangian type methods is the front tracking method developed in the series of work by Glimm et al. [26] where interface markers are used to modify a fixed grid only when it is close to the interface front.

Harlow and Welch in [27] developed the well known marker and cell method to study incompressible flow with free surface which uses a set of marker particles that fill up one of the phases and moves with the flow. However, the method requires a large number of parti-

cles and the interface location is not accurately described. Peskin developed a hybrid type method in [28], where the fluid is represented in Eulerian coordinates while the interface structure is represented with Lagrangian coordinates as illustrated in Fig. 2 (c). In the work of Unverdi and Tryggvason [29], a similar hybrid scheme named the front tracking method was developed where a combination of fixed grid was used for the governing equations and a Lagrangian moving grid was used to track the interface. Accurate solutions were obtained, for example in Tryggvason et al. [30] and in Esmaeeli and Tryggvason [5]. An accurate description of surface tension terms and the associated pressure jump was demonstrated in [31].

Although the Lagrangian representation of the interface results in high accuracy, it has been used much less in recent years compared to Eulerian grid methods due to several limitations. First, the Lagrangian approach is more complicated especially for higher dimensions. Secondly, grid generation is required at each time step to describe interface deformation and to maintain a well defined mesh which is computationally intensive. Moreover, the treatment of large topological changes such as merging and breakup of bubbles is restricted. Techniques for handling large interface deformations as well as breakup and merging are manual in nature. Consequently, their applications have been mostly limited to simple cases such as for a single or a few bubbles with minor topological changes.

In view of the limitations associated with the Lagrangian approach, Eulerian type methods of interface capturing schemes have become popular in recent implementations. The front capturing methods are generally easy to implement with implicit representation of the interface as shown in Fig. 2 (b) and large changes in the interface topologies are naturally taken care of. Examples of Eulerian type methods include the volume of fluid method (VOF), the level set method (LSM) and the phase field method [32]. In particular, the volume of fluid method and the level set method have gained the most attention and have been actively adopted and improved for evaporation and boiling problems while the phase field method

has been more popular among studies of solidification dynamics. To facilitate the discussion of phase change simulation and associated methods, the two methods (VOF and LSM) will be briefly described. For interested readers, further details on the Lagrangian type methods are provided by Tryggvason et al. [30].

1.3.1 Volume of Fluid Method

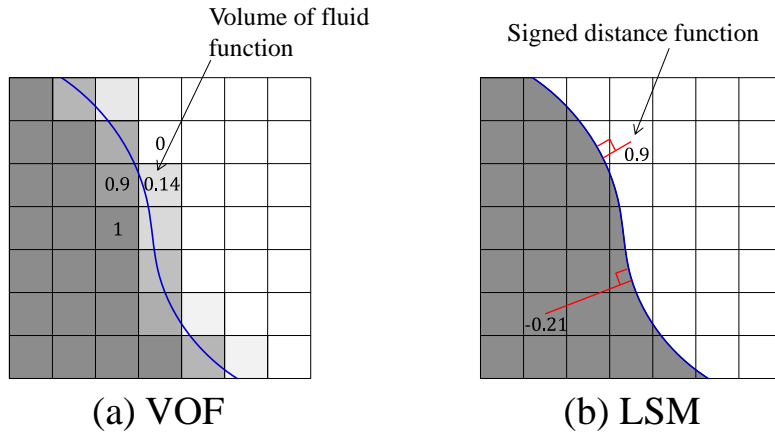


Figure 3: Illustration of the (a) volume of fluid method and (b) level set method.

The volume of fluid method is arguably the most well-known and widely used direct multi-phase method. The method originates from the marker and cell methods and was introduced by Hirt and Nichols [33] using the volume of fluid function or the so-called color function, C that represents the phase fraction. The volume of fluid function in the cells completely occupied by one phase is unity ($C = 1$) whereas in the cells completely occupied by the other phase is zero ($C = 0$). The fluid interface location is thus interpreted somewhere in the cells with the color function value between these limits as shown in Fig. 3 (a) and the function is semi-discontinuous over the interface. The volume of fluid method is considered to be the natural choice for finite volume framework and has the advantage of solving the interface advection equation without mass loss using conservative schemes. In order to obtain the interface shape using the volume of fluid function, piecewise constant schemes or piecewise

linear schemes [34] are applied to track a linear surface and its orientation. However, reconstruction of the interface from volume of fluid elements is not accurate, which negatively affects the calculation of the interface normals and curvature. Also, implementation of the algorithm is known to be complicated because of many possible surface orientations especially in three dimensional cases. Instead of interface reconstruction, alternative approaches are available such as the compressive VOF methods or interface sharpening techniques which ensure the boundedness of the volume fraction during its advection. The compressive VOF methods introduces a controlled amount of numerical dispersion near the phase interfaces, for instance the SURFER scheme [35] and CICSAM scheme [35] in order to ensure the boundedness of the volume fraction. These methods, compared to geometric interface reconstruction, are computationally efficient and simplify the implementation to arbitrary meshes but fail to match in accuracy. For further details on VOF, Scardovelli and Zaleski provide a review in [36].

1.3.2 Level Set Method

The level-set method was introduced by Osher and Sethian [37] and has been applied not only in multiphase flow but in a wide range of problems involving moving interfaces such as crystal growth, flame front propagations, fluidstructure interactions and image processing. As in the volume of fluid method, the interface is represented implicitly on the Eulerian grid points. The difference is that the scalar function representing the interface in the level set method is a continuous level set function ϕ . The most common level set function is the distance function. In this case, each cell contains a distance function with a positive or a negative sign for each of the two-phases or fluids and the magnitude is equal to the distance to the closest interface as shown in Fig. 3 (b). Thus the contour of the level set function cut by the zero level set plain defines the location of the interface and the topological changes are handled automatically.

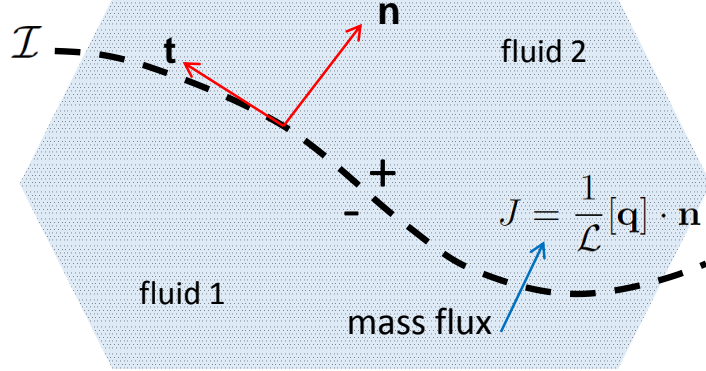


Figure 4: Illustration of the interfacial jump conditions.

The level set method has clear advantages and disadvantages compared to the volume of fluid method. The interface is always sharply defined so that there is no need for an interface sharpening scheme. Moreover, the smooth scalar function allows an accurate calculation of its gradient and therefore, the interface curvature and normal, as well. The advection of the level set function is governed by a partial differential equation. A high order of accuracy is achievable using a high resolution scheme, in particular the essentially non-oscillatory (ENO) or the weighted essentially non-oscillatory (WENO) scheme. However, since the distance function is not conservative in nature, it is prone to mass loss when the interface is under-resolved. Another on going issue is the reinitialization of the level set function to the distance function. Because the advection of the level set function does not guarantee that it stays as a distance function, a reinitialization (or redistancing) step is required at each time step. However, the traditional reinitialization scheme artificially moves the sharp interface location and changes the volume of a phase. Obviously, numerous approaches have been addressed in improving the level set mass conservation and a thorough discussion will be presented in section 1.3.4.

1.3.3 On the Interface Jump Capturing Scheme

The actual two-phase interface is not a geometric boundary but a thin region where transition of molecular density occurs over a several Angstrom units. However, at the scale of continuum mechanics, interfacial thickness is assumed to be sharp and the properties material properties are taken to be discontinuous across the interface.

Fig. 4 shows an illustration of the interface and the interfacial physics across the interface. Here, \mathbf{n} is the unit normal and \mathbf{t} is the unit tangent to the interface. Apart from the discontinuous difference in the thermodynamic properties in the bulk phase, there exists a jump in the transfer variables. For multiphase flow with heat transfer and phase change, the balance of the governing equations (namely mass, momentum and energy) over an interfacial area yields the jump conditions in the normal momentum, tangential momentum, velocity and thermal energy at the interface.

Although it is more realistic to consider the these jump conditions in a sharp manner, in practical implementations, a continuous interface is more feasible. Moreover, a discontinuous interface treatment still remain a formidable challenge for the Eulerian type methods. An example of a rigorous approach to the continuous treatment of interfacial force is the continuum surface force (CSF) model developed by Brackbill [38].

One of the most successful efforts to avoid the diffused interface approach used by a number of the front capturing methods is the so called ghost fluid method developed by Fedkiw et al. in [39]. To understand the idea of the ghost fluid method, consider a sharp interface of phase 1 and phase 2 in Fig. 5. The fluid properties and flow variables exhibit sharp changes as illustrated by the cell colors. Given a jump condition across the interface, the ghost fluid method projects the jump value across the interface in a new ghost fluid cell for each phase so that each phase can be discretized with corresponding phase cells.

The method was originally applied for the inviscid Euler equation in [39] and has been ex-

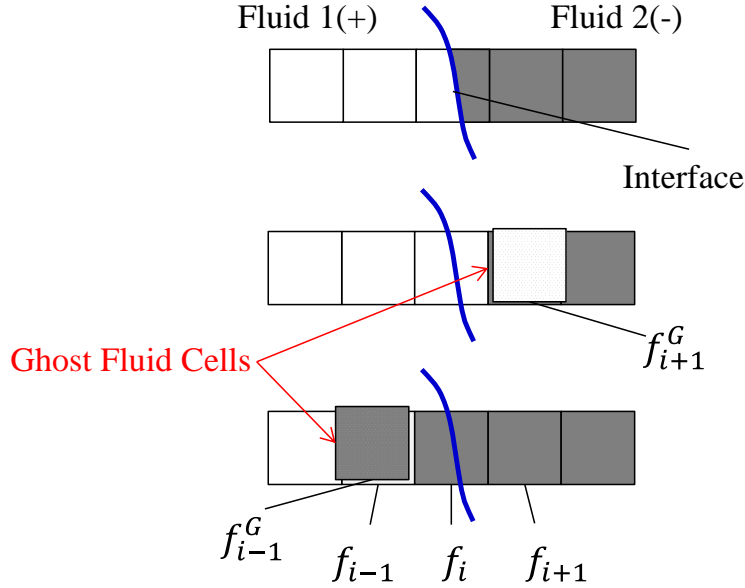


Figure 5: Illustration of the ghost fluid method. (Top) two-phases divided by an interface, (Middle and bottom) discretization using ghost fluid cells denoted by superscript G .

tended through several papers for treating shock and deflagration in [40], variable Poisson equation on irregular domain in [41, 42], multiphase incompressible flow with sharp representation of viscosity and surface tension in [43], incompressible flame discontinuity in [44] and for the multiphase incompressible flow with phase change in [10]. Similar methods have been adopted using level set method by Lou et al. [45] and by Son and Dhir in [46].

An important aspect in the development of the ghost fluid method is the symmetric formation of the linear system of equation for the variable coefficient Poisson equations where the benefits are in the solution time and efficiency. Readers can refer to a review by Osher and Fedkiw [47] for more details on the level set method and ghost fluid method.

The ghost fluid method has showed very promising results in coupling the interface jump condition sharply without numerical oscillation. When the pressure jump from the surface tension is smeared out as in the CSF method, it has been known to create large spurious currents around the interface due to an incorrect balance of interfacial stress forces. The ghost fluid method has been quite effective in reducing this parasitic current.

However, application to engineering problems with stringent physical conditions does not always seem to work as well. Especially for a sharp velocity jump condition, the large difference in the density creates orders of magnitude different velocities across the interface and the large local source terms in the velocity divergence easily lead to pressure oscillation and parasitic currents around the interface.

The sharp interface method has been distinctively strong in describing the interface velocity using the velocity jump condition where as in some of the previous models the interface is advected using an averaged fluid velocity which is somewhat vaguely derived. However, the introduction of the velocity jump condition has shown issue of its own in its computation and the method has often shown to suffer from unstable pressure and anisotropic interface velocity for problems involving mass transfer. Therefor, there is a need to improve the numerical scheme to eliminate the numerical error caused by the sharp interface while preserving the accurate physical model. In this work, an improved approach using diffused fluid velocity has been developed.

1.3.4 On the Mass Conservation of the Level Set Method

Another issue, particularly concerning the level set formulation, is that the total mass conservation is not satisfied in both the level set advection and the re-initialization step. Many efforts have been made to tackle this issue. Sussman et al. [48] modified the level set formulation by introducing another iterative procedure for better mass conservation and Chang et al. [49] proposed a correction to the level set function by a normal motion proportional to its local curvature and the deviation of the total mass. This correction procedure had to be stabilized by adding a certain constant and to be iterated by several steps. Subsequently, Son [50] improved his previous phase change method to achieve global mass conservation during the calculation procedure by adding a volume-correction step. However, this approach does not ensure conservation of mass in each bubble or droplet and its implementation to phase

change problems is not clearly defined. Further efforts to enhance the mass conservation have been made by combining two front capturing methods. In order to incorporate advantages of both the volume of fluid method and the level set method, namely the conservation of mass and the accurate curvature property a coupled level-set and volume of fluid (CLSVOF) method was introduced by Bourlioux [51]. This method was further developed by Sussman and Puckett [52] for computing incompressible two-phase flows. In this method, the interface is reconstructed from the volume of fluid function and the interface normal is evaluated from the smooth level set function. The reconstructed interface is used to calculate the fluid volume fluxes and to reinitialize the LS function for mass conservation. Tomar et al. [9] utilized this method in the phase change simulation. Enright et al. [53] came up with a hybrid particlelevel set method (HPLS) using Lagrangian particles and level set method to correct interface advection and conserve mass.

In current research, the 5th order weighted essentially non-oscillatory (WENO) scheme is used for the interface advection equation and the level set reinitialization is performed with an advanced method called the geometric projection method recently developed by Zhipeng and Riaz [54]. In their work, it has been shown that their method along with the high order advection scheme result in good mass conservation. During my research, I have found that there is an intrinsic source of error in the interface velocity calculation which can easily lead to an additional loss of mass. The source of this error has been identified to be the mass flux projection from the interface to the local staggered grid points. A general correction method for improved mass flux conservation during interface advection is proposed in this thesis.

1.4 Literature Review on the Numerical Studies of Multiphase Flow with Phase Change

The advances in numerical methods for multiphase flow can be used naturally as a starting point for the implementation of phase change algorithms. Apart from the challenges faced by non phase change multiphase flow methods, phase change introduces new challenges related to jumps at the interface and the additional consideration of interface velocity. In order to accurately simulate the physical process of phase change, a numerical method must include:

1. Accurate calculation of the heat flux across the interface driven by the jump in temperature gradient at the interface
2. Accurate calculation of mass flux that results from the heat flux and the latent heat of evaporation at the saturation temperature as well, in some case, as the difference between the saturation and interface temperatures.
3. The movement of the interface caused by both phase change and the fluid flow.
4. Stable and robust numerical method that can endure high density differences and high heat fluxes across the sharp interface and to also be able to withstand large topological changes related to break up and merging.

To implement the above noted features related to the phase change process, mass flux is typically added as a source term in the continuity equation in terms of heat flux and the latent heat of evaporation. It needs to be correctly applied in the spatial distribution near the interface such that it is positive in the gas phase and negative in the liquid phase and the total mass is conserved.

One of the earliest works of deformable bubble growth on film boiling was carried by Welch [1] using the interface tracking method with a moving unstructured mesh. However, this

study was limited to moderate interfacial distortions. A study by Son and Dhir [2] with a moving boundary fitted grid was similarly restricted in large topological changes. A hybrid interface tracking method with moving interface grid on a static Eulerian grid was utilized in Juric and Tryggvason [3] for computation of phase change problems. Their method was extended later by Esmaeeli and Tryggvason to study three-dimensional film boiling in [4], multimode two-dimensional pool boiling in [5] and film boiling on horizontal cylinders in [6]. While these studies are pioneering, the manual handling of interface merging and pinching off still remains the major limitation with explicit interface grids. As large topological changes are crucial for phase change problems, many researchers have turned to the front capturing methods due to their versatility in complex interface deformation. In [7], Welch and Wilson adopted the VOF (Volume of Fluid) method with a mass transfer model to simulate the one dimensional Stefan problem and the two-dimensional film boiling problem. Son and Dhir simulated film boiling using the VOF in [2] and the level set method in [8]. They have implemented a smeared-out Heaviside function to avoid the numerical instability related to the source term. Tomar et al. [9] used the coupled level set, volume of fluid method and diffused interfacial properties for simulation of film boiling with water and R134a at near critical pressure. The effect of superheat and saturation pressure on the frequency of bubble formation has been analyzed. In [10], Gibou et al. assembled the developments of the ghost fluid method and the level set method to demonstrate the capability of their sharp interface schemes for the incompressible phase change simulations. Similar approaches have been adopted by Son and Dhir along with the immersed boundary method to include solid components and they studied various boiling problems such as three-dimensional film boiling on a horizontal cylinder [11], nucleate boiling in microcavity [12] and flow boiling in a finned microchannel [13]. Gada and Sharma [55] proposed a method called a dual-grid level set method that uses two mesh sizes. They argued that the method is capable of gaining high accuracy with substantially less computational expense. Some others have also formulated a sharp phase change scheme for a different interface capturing method. In [15], Sato et al.

employed a multiphase model based on volume fraction with an interface sharpening scheme and the marching cube algorithm to calculate the local interface area and mass flux. They emphasized the good mass conservation results in their verification problems and nucleate boiling simulations.

1.4.1 Problem Statement for Phase Change Modeling

Among the front capturing type methods, the sharp interface methods have been quite useful in being able to accurately model the sharp jump in fluid velocity and the interface velocity. However, the introduction of the sharp velocity jump is susceptible to oscillatory pressure and spurious interface velocity. In [16], Hart et al. reported numerical instability in a mass source term localized in a very narrow interfacial region. To avoid the instability they smeared the mass source by solving a pseudo time-step diffusion equation. However, violation of mass conservation was reported when the interface was not flat due to non-symmetric integration over the distributed mass source region. Schlottke et al. [17] investigated the oscillating pressure associated with the mass source term that appears from the sharp velocity jump condition. Although their method is based on the VOF, the large pressure peak from a sharp mass source is common to other interface tracking methods. The fluctuation of pressure is undesirable because the effect is globally transmitted and can be a critical issue for pressure dependent terms in the non-constant interface temperature problems. Hence, the pressure field formation due to phase change has not been sufficiently evaluated in past literature.

The accuracy of interface advection in the presence of interfacial mass flux (mass flux conservation) has been discussed in [14, 18]. They found that the method of extending one phase velocity to the entire domain described in [19] suffers from a lack of mass flux conservation when the density difference is high. To improve the solution, the authors imposed a divergence free condition for the extended velocity field by solving a constant coefficient Poisson equation. The approach has shown good results with an enclosed bubble or droplet but is

not general for more complex flow and requires additional solution of the linear system of equations.

In present thesis, an improved approach that tackles both the numerical oscillation of pressure and the spurious interface velocity field is presented by featuring (i) continuous velocity and density fields within a thin interfacial region and, (ii) temporal velocity correction steps to avoid unphysical pressure source term. Also, a general (iii) mass flux projection correction scheme is proposed for improved mass flux conservation. The pressure and the temperature gradient jump conditions are treated sharply. Detailed research objectives and achieved contributions are given in the following section.

1.5 Research Objectives

The work in present thesis is divided into two sections. The first section consists of two main objectives: (1)the development of a new numerical method for simulating multiphase flow with phase change, and (2) verification/validation of the new numerical method. The second section deals with developing an understanding of heat transfer phenomena associated with flow boiling regime, namely, the transient heat transfer and phase change aspects in a slug flow through a small vertical tube coupled with the dynamics of a Taylor bubble separated by liquid slugs. The detailed objectives of each section are listed.

1. Development of multiphase, phase change numerical methods
 - (a) Literature review of the state of the art numerical methods for DNS of multiphase flow with phase change and their applicability in thermal engineering.
 - (b) Implementation of implicit interface multiphase flow method (Level Set method), sharp interface jump condition method (Ghost Fluid method) and identification of existing issues.

- (c) Implementation of constituent schemes such as PDE based extrapolation schemes, essentially non-oscillatory schemes, Crank-Nicolson Scheme, etc.
- (d) Development of a robust and accurate numerical scheme for the multiphase, phase change simulation with particular interest in overcoming issues faced by existing methods
- (e) Improving the capability for resolving large density contrasts while maintaining high accuracy.

2. Verification and validation.

- (a) Verification and validation using a series of one-dimensional and two-dimensional test cases.
 - (b) Validation with respect to the well characterized film boiling problem in two-dimensional and cylindrical, axisymmetric coordinates and comparison with previous numerical results, correlations and experimental figures.
3. Numerical study of Taylor bubble flow in a small vertical tube with heat transfer and phase change
- (a) Implementation of an axisymmetrical domain with moving frame of reference.
 - (b) Perform validation using adiabatic Taylor bubble flow.
 - (c) Investigation on the effects of various dimensionless parameters.

2 Formulation of Governing Equations

Three governing equations, the mass, momentum and energy conservation equations coupled with the interfacial jump conditions are considered to obtain solutions for the pressure, velocity and temperature field. The interfacial conditions consist of the pressure jump condition due to surface tension force and the phase change, the temperature gradient jump condition due to different thermal conductivity and the velocity jump condition due to the mass transfer and the difference in densities.

2.1 Energy Conservation and Heat Flux

The internal energy e conservation equation is written as

$$\rho \left(\frac{\partial e}{\partial t} + \mathbf{u} \cdot \nabla e \right) = \nabla \mathbf{q} + \tau : \nabla \mathbf{u} - P \nabla \cdot \mathbf{u} + \rho S , \quad (1)$$

where \mathbf{q} is the heat flux, \mathbf{u} the velocity, P the pressure, S an energy source term and τ the stress tensor. $-P \nabla \cdot \mathbf{u}$ is the pressure work term and $\tau : \nabla \mathbf{u}$ is the viscous dissipation term. The energy equation can be simplified with negligible viscous work compared to the convective and conductive heat transfer and no pressure work due to incompressible flow. These assumptions have been common in many literatures concerning incompressible multiphase boiling simulations [2, 3, 7, 8, 9, 10, 16, 56].

The heat flux is given by Fourier's law, $\mathbf{q} = -k \nabla T$ where k is the thermal conductivity. The energy source related to phase change process appears at the phase boundary and is canceled out in this formulation through the Dirichlet interfacial temperature boundary condition, $T_l = T_g = T_\Gamma$ where the subscript Γ denotes the interface. In other words, all the energy from heat flux across the interface is transformed to evaporation and condensation heat instantly and there is no excess energy left behind. With constant specific heat, c and

density, ρ within each phase, the energy equation is rewritten in terms of temperature as

$$\rho c \left(\frac{\partial T}{\partial t} + \mathbf{u} \cdot \nabla T \right) = -\nabla \cdot \mathbf{q} + \rho S , \quad (2)$$

The interface temperature can be derived as given by [3]

$$T_\Gamma - T_{sat} = \frac{T_{sat}(P_\Gamma - P_\infty)}{h_{gl}} \left(\frac{1}{\rho_g} - \frac{1}{\rho_l} \right) + \frac{(c_g - c_l)(T_\Gamma - T_{sat})^2}{h_{gl}} - \frac{\sigma T_{sat} \kappa}{2h_{gl}} \left(\frac{1}{\rho_g} + \frac{1}{\rho_l} \right) + \frac{\dot{m}_\Gamma}{\varphi} , \quad (3)$$

where the subscripts sat and ∞ refer to the saturated fluid and the ambient condition respectively. Subscript g and l denotes gas and liquid phase, \dot{m}_Γ is the mass flux, h_{lg} is the latent heat of evaporation, κ is the curvature and σ is the surface tension coefficient. φ is kinetic mobility defined as

$$\varphi = \frac{2\chi}{2-\chi} \frac{h_{gl}}{\sqrt{2\pi R T_{sat}}} \frac{1}{(\nu_g - \nu_l) T_{sat}} , \quad (4)$$

interpreted as the resistance to mass transfer across the interface. Here χ is the evaporation coefficient, R the gas constant and ν the specific volume. The constant interface temperature assumption may not be adequate for cases such as in microscale problems. From the scale analysis performed in [3], the two largest terms, the first and the third terms, are taken into account in the validation cases. The interfacial pressure P_Γ on the other hand is not continuous and is taken as the average, $P_g + P_l = P_\Gamma$ to be used to account for the interface temperature dependence on the pressure.

2.2 Mass Flux and the Velocity Jump Condition

With the negligible kinetic and viscous energy dissipation assumptions, the mass flux \dot{m} is determined simply from the heat flux difference across the interface and the latent heat of phase change as

$$\dot{m}_\Gamma = \frac{(-\mathbf{q}_g + \mathbf{q}_l) \cdot \mathbf{n}}{h_{lg}} = \frac{(k_g \nabla T_g - k_l \nabla T_l) \cdot \mathbf{n}}{h_{lg}} . \quad (5)$$

The mass conservation across the interface gives the relation between the mass flux, fluid velocity and the interface velocity by

$$\rho_l(V_\Gamma - \mathbf{u}_l \cdot \mathbf{n}) = \rho_g(V_\Gamma - \mathbf{u}_g \cdot \mathbf{n}) = \dot{m}_\Gamma , \quad (6)$$

where V_Γ is the magnitude of the interface velocity in the interfacial normal, \mathbf{n} direction. Above relation implies that the velocity jump condition is reflected only in the interface normal direction, in other words, a no-slip boundary condition along the interface,

$$\mathbf{u}_g \cdot \mathbf{t} = \mathbf{u}_l \cdot \mathbf{t} = \mathbf{u}_\Gamma \cdot \mathbf{t} , \quad (7)$$

where \mathbf{u}_Γ is the interface velocity and \mathbf{t} is the interface tangent vector. Reorganizing this equation, the velocity jump condition at the interface can be obtained as

$$(\mathbf{u}_g - \mathbf{u}_l) \cdot \mathbf{n} = \left(\frac{1}{\rho_l} - \frac{1}{\rho_g} \right) \dot{m} , \quad (8)$$

and owing to Eq. 7, it can be written more conveniently in terms of the fluid velocity jump as

$$\mathbf{u}_g - \mathbf{u}_l = \left(\frac{1}{\rho_l} - \frac{1}{\rho_g} \right) \dot{m} \mathbf{n} . \quad (9)$$

2.3 Momentum Conservation Across Interface

Analogous to the phase change source term in the energy equation, the jump condition in Eq. 9 provides the interfacial velocity boundary condition for the governing equations. As a result, the phase change related source term does not appear in the incompressible Navier-Stokes equations and is given by

$$\rho \left(\frac{\partial \mathbf{u}}{\partial t} + \mathbf{u} \cdot \nabla \mathbf{u} \right) = -\nabla P + \nabla \cdot \tau + \rho \mathbf{g} , \quad (10)$$

$$\nabla \cdot \mathbf{u} = 0 . \quad (11)$$

Here \mathbf{g} is the body force, e.g. gravity and the deviatoric stress tensor τ is given by $\tau = \mu(\nabla \mathbf{u} + (\nabla \mathbf{u})^T)$ where μ is the dynamic viscosity. The thermodynamic properties of the fluids are assumed to be constant within the bulk phases. The surface tension force, the normal tangential stress jump and the mass flux all contribute to the jump in the pressure

$$P_l - P_g = \sigma(T_\Gamma)\kappa + (\mathbf{n} \cdot \tau_l - \mathbf{n} \cdot \tau_g) - \left(\frac{1}{\rho_g} - \frac{1}{\rho_l} \right) \dot{m}_\Gamma^2 , \quad (12)$$

where the surface tension coefficient in general depends on the interface temperature but is assumed in this work to take on a constant value corresponding to the saturation temperature. Also the normal stress jump term is treated by smoothing the viscosity across the interface.

2.4 Interface Velocity and Advection

From Eq. 6 and Eq. 7, the interface velocity vector is given

$$\begin{aligned}\mathbf{u}_\Gamma &= V_\Gamma \mathbf{n} + [\mathbf{u}_l - (\mathbf{u}_l \cdot \mathbf{n})\mathbf{n}] = \frac{\dot{m}\mathbf{n}}{\rho_l} + \mathbf{u}_l \\ &= V_\Gamma \mathbf{n} + [\mathbf{u}_g - (\mathbf{u}_g \cdot \mathbf{n})\mathbf{n}] = \frac{\dot{m}\mathbf{n}}{\rho_g} + \mathbf{u}_g ,\end{aligned}\quad (13)$$

which is used to advect the interface. The interface, Γ is represented using the zero level of a continuous surface level set function ϕ

$$\Gamma(t) = \{\mathbf{x} \in \Omega : \phi(\mathbf{x}, t) = 0\} . \quad (14)$$

It is advantageous to build the level set function as the signed distance to the closest zero level set

$$\phi(\mathbf{x}, t) = \pm |\mathbf{d}|, \quad (15)$$

and the signs naturally correspond to two different phases, in current cases, gas ($\phi < 0$) and liquid ($\phi > 0$). The advection the level set function is performed by

$$\frac{\partial \phi}{\partial t} + \mathbf{u}_\Gamma \cdot \nabla \phi = 0 . \quad (16)$$

The interface velocity is physically valid only on the interface Γ and but is needed within a finite region around the interface in order to advect ϕ according to Eq. 16. While the construction of \mathbf{u}_Γ through Eq. 13 is continuous at the interface, it is not necessarily divergence free or smooth. Because the interface, ϕ is an implicit representation, it is important to construct a smooth and uniform interface velocity field.

2.5 Non-dimensionalization

The governing equations, fluid properties and the transport variables are non-dimensionalized primarily based on the liquid phase and the gas-liquid ratios are used to write the gas phase equations. The liquid and gas phase Navier-Stokes equation are given in dimensionless form as

$$\frac{\partial \mathbf{u}}{\partial t} + \mathbf{u} \cdot \nabla \mathbf{u} = -\nabla P + \nabla \cdot \left[\frac{1}{\text{Re}} (\nabla \mathbf{u} + (\nabla \mathbf{u})^T) \right] + \frac{1}{\text{Fr}^2} \hat{k} , \quad (17)$$

$$\frac{\partial \mathbf{u}'}{\partial t} + \mathbf{u}' \cdot \nabla \mathbf{u}' = -\frac{1}{\rho'} \nabla P + \nabla \cdot \left[\frac{\mu'}{\rho'} \frac{1}{\text{Re}} (\nabla \mathbf{u}' + (\nabla \mathbf{u}')^T) \right] + \frac{1}{\text{Fr}^2} \hat{k}' , \quad (18)$$

and for the temperature equation, they are

$$\frac{\partial T}{\partial t} + \mathbf{u} \cdot \nabla T = \nabla \cdot \left(\frac{1}{\text{RePr}} \nabla T \right) , \quad (19)$$

$$\frac{\partial T'}{\partial t} + \mathbf{u}' \cdot \nabla T' = \nabla \cdot \left(\frac{\alpha'}{\text{RePr}} \nabla T' \right) , \quad (20)$$

omitting the notion ' for the dimensionless transport variables. The mass flux is expressed with the Stefan number and the Peclet number as,

$$\dot{m}_\Gamma = -\frac{\text{St}}{\text{RePr}} k' \nabla T_g \cdot \mathbf{n} + \frac{\text{St}}{\text{RePr}} \nabla T_l \cdot \mathbf{n} . \quad (21)$$

and the pressure jump

$$P_l - P_g = \kappa \text{We} + \left(\frac{1}{\rho'} - 1 \right) \dot{m}_\Gamma^2 , \quad (22)$$

3 Numerical Formulations

The MAC staggered grid method [57] is used for the discretization of the governing equations. The velocity components are located at the cell edges while scalar variables (pressure, temperature, level set function) and thermodynamic properties (density, viscosity, thermal conductivity, heat capacity) are computed at the cell center as shown in Fig. 6.

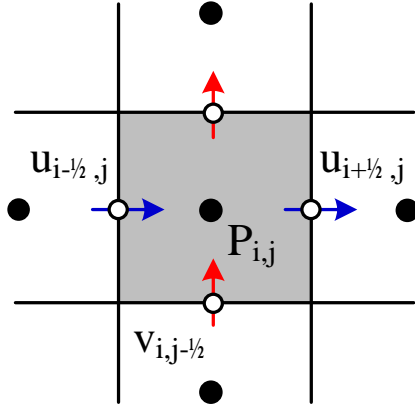


Figure 6: Illustration of staggered grids where pressure P is located at the cell center and the velocity components, u and v , are on the cell faces.

The time-dependent incompressible Navier-Stokes equations are solved explicitly in time using the standard projection method [58]. For the velocity jump condition, an improved approach using diffused interface properties and a temporal velocity correction procedure to increase the robustness of the phase change solution is proposed. Furthermore, a correction to the standard mass flux projection procedure is developed using the interface curvature information close to the interface. I start by describing the new approach for the velocity jump condition and the velocity correction steps.

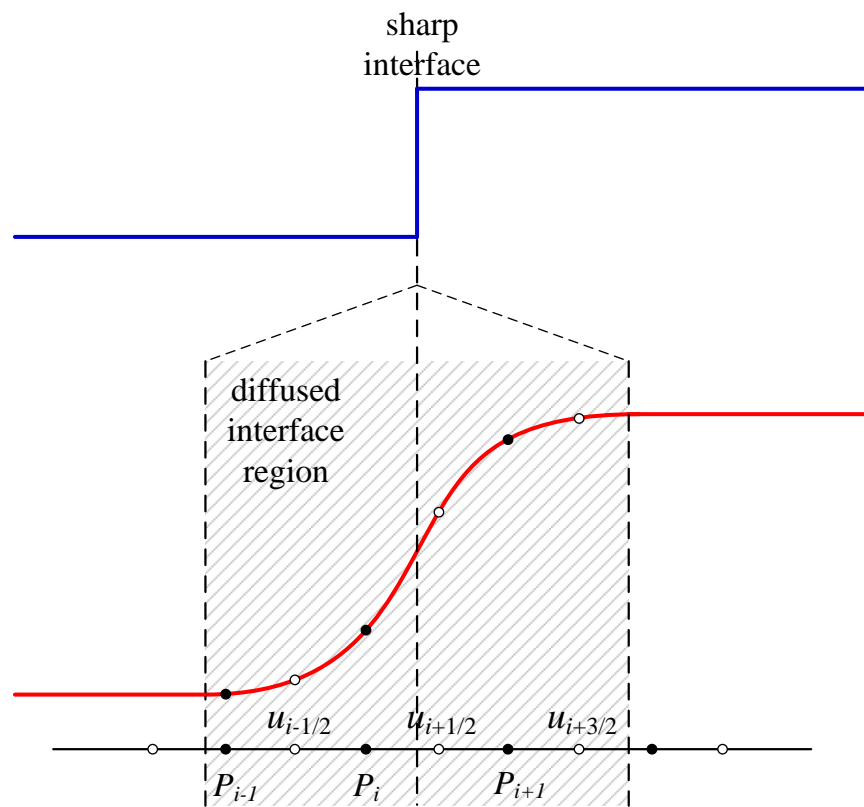


Figure 7: Illustration of 1-D diffused density profile within the diffused interface. The corresponding velocity jumps are calculated using the diffused densities in each cell.

3.1 Diffused Interface for Velocity Jump Condition

In order to create a robust implementation for the velocity jump condition, a diffused interface approach for velocity is used. A typical smoothed Heaviside function is used in this regard, which is defined as

$$H_\epsilon(\phi(\mathbf{x})) = \frac{1}{2} \left[1 + \text{erf}\left(\frac{\phi(\mathbf{x})}{\epsilon}\right) \right] , \quad (23)$$

where the thickness of the diffused region is controlled by the value ϵ . The thickness of the diffused zone remains constant over time as long as the signed distance function, ϕ , is reinitialized correctly near the interface region. A new approach of reinitialization, based on geometric projection of the interface, [54] has been shown to achieve second-order spatial accuracy for the construction of the signed distance function. An illustration of the diffused region associated with the sharp interface is provided in Fig. 7 where the blue and the red lines represent the sharp and the diffused density profiles, respectively. The cell centers are shown in black and the edges in white. The Heaviside function is evaluated at cell faces using arithmetic averaging of the signed distance function and is then used to calculate the smoothed inverse of the density profile, $\tilde{\beta}$ as

$$\tilde{\beta}(\mathbf{x}) = \frac{1}{\rho_g} H_\epsilon(\phi(\mathbf{x})) + \frac{1}{\rho_l} (1 - H_\epsilon(\phi(\mathbf{x}))) . \quad (24)$$

The smoothing of density defined in Eq. 24 complements the density related content of the jump conditions that are based on the inverse of local density values. I have found this approach to result in a symmetric distribution of the jump conditions about the interface. In Fig. 8, the distributions of the jump conditions across each cell, $\dot{m}(1/\rho_{i+1} - 1/\rho_i)$ within the diffused interface region are plotted for the inverse and the normal density smearing. Note that the smoothed density profile defined in Eq. 24 is used only for calculating the mass flux. The sharp density profile is used for all other purposes, as described further

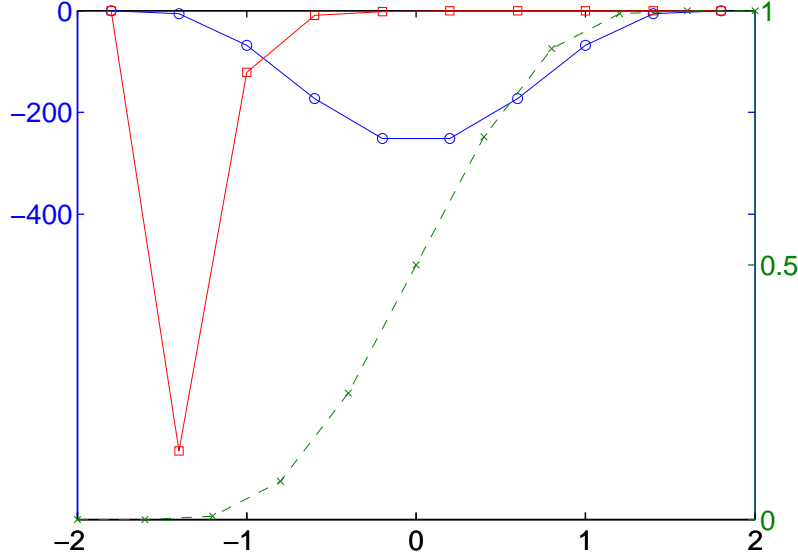


Figure 8: The distribution of jump condition using diffused densities: (red square) normal density diffusion, (blue circle) inverse density diffusion and (green dashed) the Heaviside function.

below. The purpose of using the special density profile in Eq. 24 is to smooth the velocity profile as described below. Consider, for example, a second-order central difference scheme for the momentum diffusion term about node $(i + 1/2)$. The required nodes, $(i - 1/2)$ and $(i + 3/2)$ are updated by ghost values if they are in a phase that is different than the one at $(i + 1/2)$. Assuming constant viscosity for illustration, the diffusion term can be written as

$$\frac{\partial}{\partial x} \left(\mu \frac{\partial u}{\partial x} \right) \Big|_{i+1/2} = \frac{\mu}{\Delta x^2} (u_{i+3/2}^G - (u_{i+1/2}^G)^2 + u_{i-1/2}^G) . \quad (25)$$

where superscript G refers to fictitious velocities that are defined as

$$\begin{aligned} u_{i+3/2}^G &= u_{i+3/2}, \\ u_{i-1/2}^G &= u_{i-1/2} - \dot{m}_{i-1/2} \left(\frac{1}{\rho_g} - \frac{1}{\rho_l} \right) n_{x,i-1/2} , \end{aligned} \quad (26)$$

where $n_x = 1$ for one-dimensional case and \dot{m} is evaluated by means of constant extrapolation from the interfacial node [59]. Thus each cell is provided with the correct phase velocity, depending on the phase of the node under consideration, which is essentially the ghost fluid

approach. The advantage of this approach is that, it allows a sharp implementation of physical jumps at the discrete level and preserves the symmetry of the Poisson coefficient matrix [42].

For the diffused interface approach, the ghost values take the following form.

$$\begin{aligned} u_{i-1/2}^G &= u_{i-1/2} + \dot{m}_i \left(\tilde{\beta}_{i-1/2} - \tilde{\beta}_{i+1/2} \right) n_{x,i} \\ u_{i+3/2}^G &= u_{i+3/2} + \dot{m}_{i+1} \left(\tilde{\beta}_{i+3/2} - \tilde{\beta}_{i+1/2} \right) n_{x,i+1} . \end{aligned} \quad (27)$$

The jump condition applied to each nodes is based on the difference in $\tilde{\beta}$ with respect to the node being solved for and the ghost values are in effect unchanged if there is no density difference. The implementation is rather simple since all nodes, including the primary node can be updated. \dot{m} and n_x approximated at the middle of the two density nodes ensure that a consistent jump condition is applied when solving for other nodes, e.g. $(i - 1/2)$. Ghost cells are used throughout the projection method, first in the calculation of the intermediate velocity u^* and then the divergence of the intermediate velocity, $\nabla \cdot u^*$, on the RHS of the pressure Poisson equation [10]. It is also used to obtain the correct phase velocity for the convective heat transfer in the energy equation. Similarly, for two-dimensional formulation, the ghost fluid velocities for $v_{i,j+1/2}$ are calculated as

$$\begin{aligned} v_{i,j-1/2}^G &= v_{i,j-1/2} + \dot{m}_{i,j} \left(\tilde{\beta}_{i,j-1/2} - \tilde{\beta}_{i,j+1/2} \right) n_{y,i,j} \\ v_{i,j+3/2}^G &= v_{i,j+3/2} + \dot{m}_{i,j+1} \left(\tilde{\beta}_{i,j+3/2} - \tilde{\beta}_{i,j+1/2} \right) n_{y,i,j+1} . \end{aligned} \quad (28)$$

Then the intermediate velocity field, \mathbf{u}^* of the projection method can be evaluated without the pressure term as

$$\mathbf{u}^* = \mathbf{u}^G + \Delta t \left(-\mathbf{u}^G \cdot \nabla \mathbf{u}^G + \frac{1}{\rho^n} \nabla \cdot [\mu (\nabla \mathbf{u}^G + (\nabla \mathbf{u}^G)^T)] + \mathbf{g} \right) , \quad (29)$$

using the ghost fluid values. The spatial discretization of Navier-Stokes equations is treated

by the second-order-accurate, central-difference scheme and the temporal discretization by a first-order explicit scheme.

The velocity field at the new time level, \mathbf{u}^{n+1} is related to \mathbf{u}^* and pressure by

$$\frac{\mathbf{u}^{n+1} - \mathbf{u}^*}{\Delta t} = -\frac{\nabla p^{n+1}}{\rho^{n+1}}, \quad (30)$$

and taking the divergence of this equation with the divergence free condition, $\nabla \cdot \mathbf{u}^{n+1} = 0$, gives the Poisson equation,

$$\nabla \cdot \left(\frac{\nabla p^{n+1}}{\rho^{n+1}} \right) = \frac{\nabla \cdot \mathbf{u}^*}{\Delta t} + w_p, \quad (31)$$

where w_p is a term that results from the sharp implementation of pressure jump in Eq. 12. The density ρ^n and ρ^{n+1} in Eq. 29-31 can be chosen independently (sharp or diffused) of the diffused density for mass flux, $\tilde{\beta}$. The divergence of intermediate velocity on the right hand side of Eq. 31 is obtained using the ghost fluid method. It is given by

$$\nabla \cdot \mathbf{u}^*|_{i,j} = \frac{1}{\Delta x} (u_{i+1/2,j}^{*G} - u_{i-1/2,j}^{*G}) + \frac{1}{\Delta y} (v_{i,j+1/2}^{*G} - v_{i,j-1/2}^{*G}), \quad (32)$$

where

$$\begin{aligned} u_{i-1/2,j}^{*G} &= u_{i-1/2,j}^* + \dot{m}_{i-1/4,j} (\tilde{\beta}_{i-1/2,j} - \tilde{\beta}_{i,j}) n_{x,i-1/4,j} \\ u_{i+1/2,j}^{*G} &= u_{i+1/2,j}^* + \dot{m}_{i+1/4,j} (\tilde{\beta}_{i+1/2,j} - \tilde{\beta}_{i,j}) n_{x,i+1/4,j} \\ v_{i,j-1/2}^{*G} &= v_{i,j-1/2}^* + \dot{m}_{i,j-1/4} (\tilde{\beta}_{i,j-1/2} - \tilde{\beta}_{i,i}) n_{y,i,j-1/4} \\ v_{i,j+1/2}^{*G} &= v_{i,j+1/2}^* + \dot{m}_{i,j+1/4} (\tilde{\beta}_{i,j+1/2} - \tilde{\beta}_{i,i}) n_{y,i,j+1/4}. \end{aligned} \quad (33)$$

If the approximation of the mass flux and the normal vector are simplified to the node (i, j) ,

Eq. 32 becomes

$$\nabla \cdot \mathbf{u}^*|_{i,j} = \frac{1}{\Delta x} (u_{i+1/2,j}^* - u_{i-1/2,j}^*) + \frac{1}{\Delta y} (v_{i,j+1/2}^* - v_{i,j-1/2}^*) - \dot{m}_{i,j} \nabla \tilde{\beta} \cdot \mathbf{n}_{i,j}, \quad (34)$$

where the last term can be considered as the source for the velocity divergence condition,

$$\nabla \cdot \mathbf{u}^{n+1} = \dot{m}_{i,j} \nabla \tilde{\beta} \cdot \mathbf{n}_{i,j}. \quad (35)$$

The specific form of the source term varies for different methods [8, 10, 14, 17] but essentially originates from the mass balance across the interface in Eq. 9. Diffused source terms similar to the one as in Eq. 35 have been implemented in [8, 45, 50] using Heaviside function. In [16], the mass source was distributed by solving the inhomogeneous Helmholtz equation for an additional scalar field. Diffused interface methods have been implemented to avoid the numerical difficulties arising from the sharp discontinuity across the interface. However, simple mass source diffusion results in a large error in the interface velocity (shown later in section 4.5) and the interface thickness is dependent on the density ratio. The new diffused interface approach using the ghost fluid technique and mass flux projection correction avoids such errors.

The pressure jump conditions in Eq. 12 is implemented using sharp ghost fluid method described in [42] and the Poisson equation is solved using a fast direct sparse matrix solver (PARDISO Solver [60]). The pressure solution from the Poisson equation is used to project the velocity at the next time step onto the divergence free field by

$$\mathbf{u}^{n+1} = \mathbf{u}^* - \Delta t \frac{\nabla P^{n+1}}{\rho^{n+1}}. \quad (36)$$

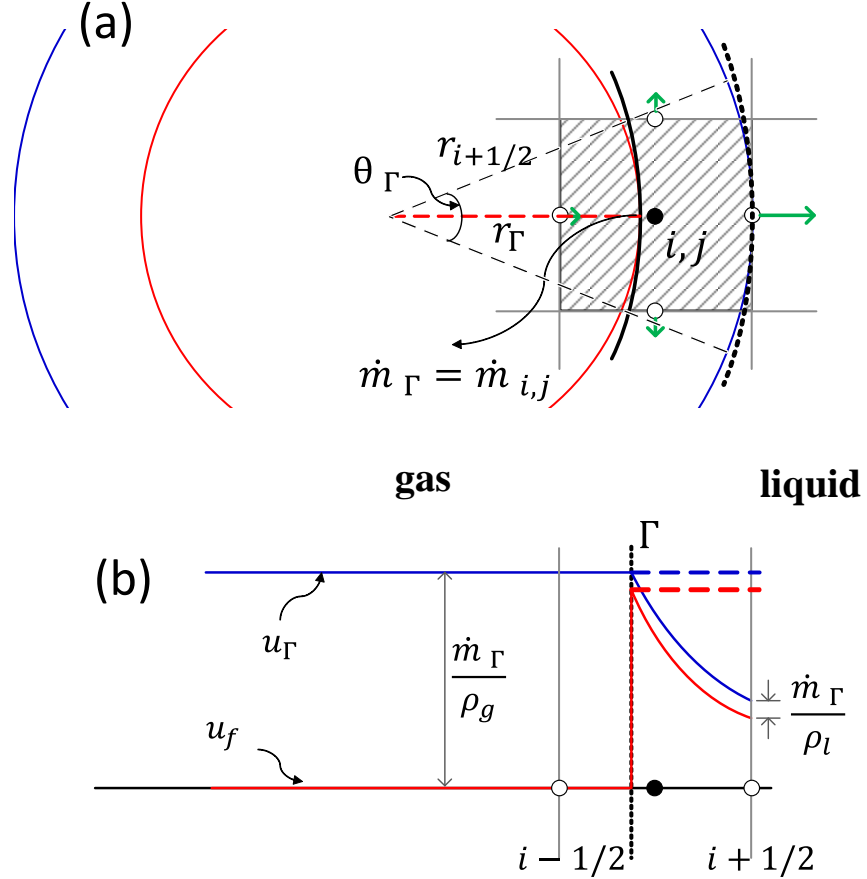


Figure 9: Sketch of mass flux projection error from interface to adjacent grid points.

Finally, using the relation shown in Eq. 13, the interface velocity is calculated as

$$\mathbf{u}_\Gamma(\mathbf{x}) = \dot{m}\mathbf{n}\tilde{\beta} + \mathbf{u}^{n+1}, \quad \mathbf{x} \in \Omega , \quad (37)$$

where Ω is the whole computational domain. According to the formulation, the diffused velocity and the velocity jump condition add up to a constant interface velocity around the interface region.

3.2 Mass Flux Projection Correction

The interface velocity given by Eq. 37 is constant for 1-D problems where the interface is flat but that is not the case when the interface is curved in 2-D space. The accuracy of mass flux implementation will be therefore evaluated for 2-D problems. The accuracy of interface velocity calculation in Eq. 37 depends on the distance from the interface. Consider the case of a bubble evaporation illustrated in Fig. 9. In plot (a), The red circle is the exact interface and the blue circle represents the interface projection to the velocity node at the cell face center. When the interface is curved, the total mass projected from the interface to the neighboring velocity node degrades due to the difference in the length of the two arc segments where the mass flux occurs. The total mass transfer at the interfacial arc (red) is matched with the total mass flux at the blue arc by

$$\theta_\Gamma r_\Gamma \dot{m}_\Gamma = \theta_{i+1/2} r_{i+1/2} \dot{m}_{i+1/2} . \quad (38)$$

where θ is the angle in radians by which the interface arc span at the center of the circle. Consequently, the jump in the velocity at $i + 1/2$ is less than the jump at interface Γ which results in an error in the interface velocity at $i + 1/2$ as shown in Fig. 9 (b). This is true for both the sharp and diffused interface approaches and becomes significant when either the curvature is large with respect to the grid resolution or the density difference is high. Attempts to workaround this issue have been shown in [44] and [14] using an extension of phases velocity field. However, that approach is not completely general and also requires an additional solution of the Poisson equation as described in [18].

Here, a more direct approach by deriving a correction term to compensate for the error in the mass flux projection is proposed. Since the local radius at a node can be approximated

as the inverse of curvature, it can be written as

$$\dot{m}_{i+1/2} = \frac{\kappa_{i+1/2}}{\kappa_\Gamma} \dot{m}_\Gamma , \quad (39)$$

where both \dot{m}_Γ and κ_Γ are interfacial values projected without any change in magnitude onto the grid nodes. The mass flux at the interface deteriorates on the order of $O(\Delta x)$ for two dimensional and $O(\Delta x^2)$ for three dimensional case as

$$\dot{m}_{i+1/2} = \frac{\kappa_{i+1/2}^2}{\kappa_\Gamma^2} \dot{m}_\Gamma . \quad (40)$$

With this correction, the ghost fluid velocity Eq. 33 in Eq. 32 is updated using Eq. 39 as,

$$\begin{aligned} u_{i-1/2,j}^{*G} &= u_{i-1/2,j}^* + \dot{m}_{i-1/4,j} \frac{\kappa_\Gamma}{\kappa_{i-1/2,j}} \left(\tilde{\beta}_{i-1/2,j} - \tilde{\beta}_{i,j} \right) n_{x,i-1/4,j} , \\ u_{i+1/2,j}^{*G} &= u_{i+1/2,j}^* + \dot{m}_{i+1/4,j} \frac{\kappa_\Gamma}{\kappa_{i+1/2,j}} \left(\tilde{\beta}_{i+1/2,j} - \tilde{\beta}_{i,j} \right) n_{x,i+1/4,j} , \\ v_{i,j-1/2}^{*G} &= v_{i,j-1/2}^* + \dot{m}_{i,j-1/4} \frac{\kappa_\Gamma}{\kappa_{i,j-1/2}} \left(\tilde{\beta}_{i,j-1/2} - \tilde{\beta}_{i,i} \right) n_{y,i,j-1/4} , \\ v_{i,j+1/2}^{*G} &= v_{i,j+1/2}^* + \dot{m}_{i,j+1/4} \frac{\kappa_\Gamma}{\kappa_{i,j+1/2}} \left(\tilde{\beta}_{i,j+1/2} - \tilde{\beta}_{i,i} \right) n_{y,i,j+1/4} . \end{aligned} \quad (41)$$

Note that the larger mass flux is applied towards the outer nodes to counteract the deteriorated velocity jump condition and vice versa for the inner nodes. The correction term does not affect the bulk phase where the density is constant. This type of correction leads to a larger jump at node $(i + 1/2)$ as depicted by the dotted red line in Fig. 9 (b). Alternatively, the correction term can be applied to Eq. 37 directly, but this can be more sensitive to the smoothness of curvature solution.

The accuracy and robustness of this approach essentially depends on the curvature calculation near the interface. The approach are tested in conjunction with the geometric projection scheme for reinitializing the level set [54]. Higher order schemes with smoother curvature approximations such as [61] can also be applied for further improvement.

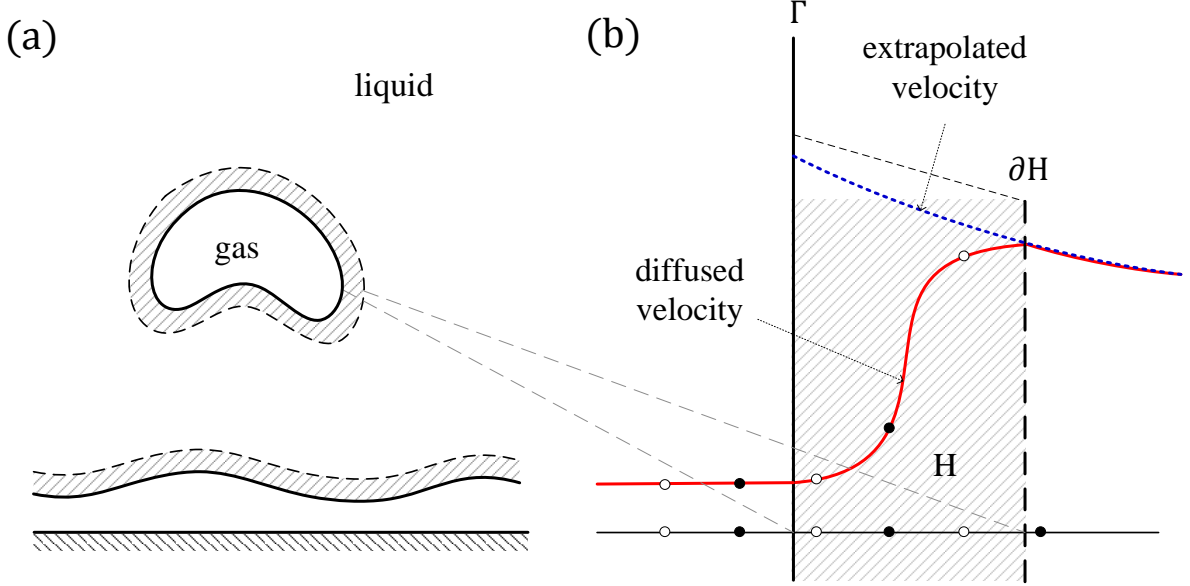


Figure 10: Illustration of (a) the asymmetric interface diffusion and (b) the extrapolation of velocity from diffused interface boundary ∂H to the interface Γ .

3.3 Asymmetric Interface Diffusion

Additional care is taken to bias the interface diffusion in the outer phase such as to avoid diffused regions in contact with a solid surface or with each other in a bubble. For example, in the film boiling problem, the diffusion is oriented towards the liquid phase as in Fig. 10 (a). The asymmetric interface diffusion also benefits the accuracy of interface velocity calculation in that the bulk phase velocity of the bubble is closest to the sharp interface profile. This also allows straight forward extrapolation of the outer phase velocity to the sharp interface location as shown in Fig. 10 (b). The extrapolation of the outer phase velocity was performed specifically to be used in the thermal energy equation because it can play a vital role in the determination of the heat flux on the outer phase.

3.4 Velocity Correction for Updated Density Field

The solution for fluid velocity, \mathbf{u} from Eq. 31 and Eq. 36 satisfies the zero divergence condition in each cell in terms of the ghost fluid velocities by

$$\begin{aligned} (\nabla \cdot \mathbf{u})_{i,j} &= 0 \\ &= \frac{1}{\Delta x} (u_{i-1/2,j}^G - u_{i+1/2,j}^G) + \frac{1}{\Delta y} (v_{i,j-1/2}^G - v_{i,j+1/2}^G) = 0 , \end{aligned} \quad (42)$$

where

$$\begin{aligned} u_{i-1/2,j}^G &= u_{i-1/2,j} + \dot{m}_{i-1/4,j} \left(\tilde{\beta}_{i-1/2,j} - \tilde{\beta}_{i,j} \right) n_{x,i-1/4,j} , \\ u_{i+1/2,j}^G &= u_{i+1/2,j} + \dot{m}_{i+1/4,j} \left(\tilde{\beta}_{i+1/2,j} - \tilde{\beta}_{i,j} \right) n_{x,i+1/4,j} , \\ v_{i,j-1/2}^G &= v_{i,j-1/2} + \dot{m}_{i,j-1/4} \left(\tilde{\beta}_{i,j-1/2} - \tilde{\beta}_{i,i} \right) n_{y,i,j-1/4} , \\ v_{i,j+1/2}^G &= v_{i,j+1/2} + \dot{m}_{i,j+1/4} \left(\tilde{\beta}_{i,j+1/2} - \tilde{\beta}_{i,i} \right) n_{y,i,j+1/4} . \end{aligned} \quad (43)$$

However, after the interface has advected to a new location over one time step, the jump in velocity condition is no longer with the updated velocity field. In other words, when the interface crosses a cell node, the velocity at that point does neither represents the actual phase velocity nor the jump condition associated with the pressure solution before advection. previous time step. Unlike flows without phase change, the right hand side in Eq. 42 includes the mass source term. The divergence structure in a cell, A , is shown in Fig. 11 where (a) is at time step n and (b) is after interface advection. The blue color indicates no phase change whereas red colored nodes indicate phase change over one time step. Velocity at the changed nodes need to be updated to represent the correct phase. In addition, it is clear that the previous divergence structure of cell A is no longer correct in Fig. 11 (b). The consequential problem arises when solving the pressure Poisson equation. The change in the velocity divergence creates an additional source that is neither due to the momentum transport nor the mass flux and creates spurious oscillation in the pressure field.

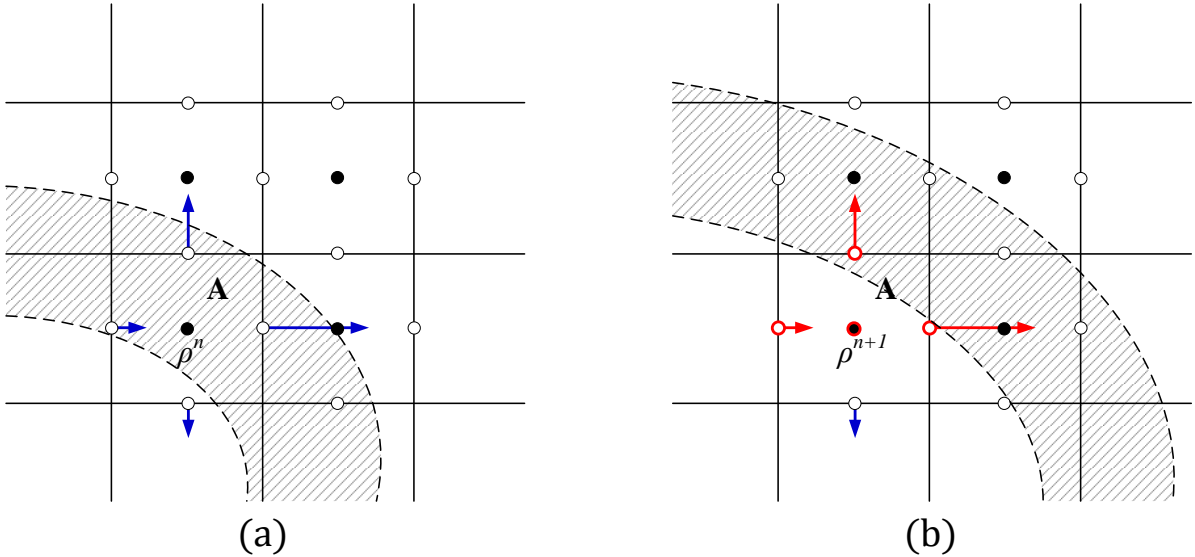


Figure 11: Illustration of divergence of fluid velocity in cell A at (a) n and (b) $n + 1$ time step. Divergence free condition met by blue vectors are no longer valid after the interface advection due to change in the jump conditions.

In order to eliminate such effect, the velocity field is updated in two steps prior to solving the Poisson equation. To facilitate the discussion, I start at time step, n , before the interface advection and take ' and " to be the intermediate time steps and $n + 1$ to be the next time level. First, the original velocity field are updated using the temporal difference in the density fields as,

$$\begin{aligned} u'_{i+1/2,j} &= u^n_{i+1/2,j} + \left(\tilde{\beta}_{i+1/2,j}^n - \tilde{\beta}_{i+1/2,j}^{n+1} \right) \dot{m}_{i+1/2,j} n_{x,i+1/2,j}, \\ v'_{i,j+1/2} &= v^n_{i,j+1/2} + \left(\tilde{\beta}_{i,j+1/2}^n - \tilde{\beta}_{i,j+1/2}^{n+1} \right) \dot{m}_{i,j+1/2} n_{y,i,j+1/2}, \end{aligned} \quad (44)$$

where the superscript ' denotes the first updated velocity field. This process updates the velocity into the correct phase based on the change of the density. In the second step, I compute an intermediate pressure velocity associated with the corrected velocity field u' and then find the divergence free velocity field, u'' , associated with the pressure P' and the

corrected velocity u' .

$$\begin{aligned}\nabla \cdot \mathbf{u}' &= \Delta t \nabla \cdot \left(\frac{\nabla P'}{\rho^{n+1}} \right) , \\ \mathbf{u}'' &= \mathbf{u}' + \Delta t \left(\frac{\nabla P'}{\rho^{n+1}} \right),\end{aligned}\tag{45}$$

The corrected velocity field, u'' , is used to calculate the intermediate velocity field of the standard Projection method as

$$\frac{\mathbf{u}^* - \mathbf{u}''}{\Delta t} = -\mathbf{u}'' \cdot \nabla \mathbf{u}'' + \nabla \cdot [\mu((\nabla \mathbf{u}'') + (\nabla \mathbf{u}'')^T)] + \mathbf{g},\tag{46}$$

followed by the pressure Poisson equation and the new velocity calculation as described in section 3.1.

With the velocity correction steps, the Poisson matrix are solved twice. However, the most time-consuming process of matrix factorization is required only once per each time step and the added computational expense is trivial.

3.5 Interface Advection and Reinitialization

Since the interface velocity field is not necessarily divergence free with phase change, the advection equation is given by

$$\frac{\partial \phi}{\partial t} + \nabla \cdot (\mathbf{u}_\Gamma \phi) - \phi(\nabla \cdot \mathbf{u}_\Gamma) = 0.\tag{47}$$

The discretization of convective terms in Eq. 47 is done using 5th order Hamilton Jacobian weighted essentially non-oscillatory (HJ-WENO) scheme [62]. The WENO scheme has been widely used for the level set methods as well as other convection dominant problems featuring high accuracy in smooth regions and essentially non-oscillatory solutions at discontinuity. It

has been shown to be very effective in minimizing the mass loss during the level set advection.

From the conservation law

$$\frac{\partial \phi}{\partial t} + f(u_\Gamma \phi)_x + g(v_\Gamma \phi)_y = \phi((u_\Gamma)_x + (v_\Gamma)_y) , \quad (48)$$

the derivative $f(u_\Gamma \phi)_x$ is approximated

$$f(u_\Gamma \phi)_x|_{x=x_i} = \frac{1}{\Delta x} \left(\hat{f}_{i+1/2} - \hat{f}_{i-1/2} \right) , \quad (49)$$

for the stencil $I_i = [x_{i+1/2}, x_{i-1/2}]$ and the numerical flux, $\hat{f}_{i+1/2}$ is calculated following upwind scheme

$$\hat{f}_{i+1/2} = \begin{cases} u_{\Gamma,i+1/2} \bar{\phi}_{i-1}^-, & \text{if } u_{\Gamma,i+1/2} > 0 \\ u_{\Gamma,i+1/2} \bar{\phi}_i^+, & \text{if } u_{\Gamma,i+1/2} < 0 \end{cases} \quad (50)$$

Only x-direction is explained since $g(\phi)_y$ is approximated in the same way. The fifth order finite difference WENO fluxes, $\hat{f}_{i\pm 1/2}$ is given by weighted derivatives calculated with three stencils around the cell center i .

$$\bar{\phi}_i^\pm = \omega_0^\pm p_i^{\pm 0} + \omega_1^\pm p_i^{\pm 1} + \omega_2^\pm p_i^{\pm 2} , \quad (51)$$

where p_i^r is the third order fluxes built on three sets of stencils as

$$\begin{cases} p_{i+1/2}^{\pm 0} = \frac{1}{3} f^\pm(\phi_{i-2}) - \frac{7}{6} f^\pm(\phi_{i-1}) + \frac{11}{6} f^\pm(\phi_i) \\ p_{i+1/2}^{\pm 1} = -\frac{1}{6} f^\pm(\phi_{i-1}) + \frac{5}{6} f^\pm(\phi_i) + \frac{1}{3} f^\pm(\phi_{i+1}) \\ p_{i+1/2}^{\pm 2} = \frac{1}{3} f^\pm(\phi_i) + \frac{5}{6} f^\pm(\phi_{i+1}) - \frac{1}{6} f^\pm(\phi_{i+2}) , \end{cases} \quad (52)$$

The weighting coefficients reflects the smoothness of f and are calculated by

$$\begin{cases} \omega_0^\pm = \frac{\alpha_0^\pm}{\sum_{l=0}^3 \alpha_l^\pm} \\ \omega_1^\pm = \frac{\alpha_1^\pm}{\sum_{l=0}^3 \alpha_l^\pm} \\ \omega_2^\pm = \frac{\alpha_2^\pm}{\sum_{l=0}^3 \alpha_l^\pm} , \end{cases} \quad (53)$$

where

$$\begin{cases} \alpha_0^\pm = \frac{C_0}{(\epsilon + IS_0^\pm)^2} \\ \alpha_1^\pm = \frac{C_1}{(\epsilon + IS_1^\pm)^2} \\ \alpha_2^\pm = \frac{C_2}{(\epsilon + IS_2^\pm)^2} , \end{cases} \quad (54)$$

with

$$C_0 = \frac{1}{10}, \quad C_1 = \frac{6}{10}, \quad C_2 = \frac{3}{10} , \quad (55)$$

are ideal weights. ϵ is to avoid zero denominator and is taken as 10^8 in current simulation.

Lastly, the IS is a measure of the smoothness given by

$$\begin{cases} IS_0^\pm = \frac{13}{12} (f^\pm(\phi_{i-2}) - 2f^\pm(\phi_{i-1}) + f^\pm(\phi_i))^2 + \frac{1}{4} (f^\pm(\phi_{i-2}) - 4f^\pm(\phi_{i-1}) + 3f^\pm(\phi_i))^2 \\ IS_1^\pm = \frac{13}{12} (f^\pm(\phi_{i-1}) - 2f^\pm(\phi_i) + f^\pm(\phi_{i+1}))^2 + \frac{1}{4} (f^\pm(\phi_{i-1}) - f^\pm(\phi_{i+1}))^2 \\ IS_2^\pm = \frac{13}{12} (f^\pm(\phi_i) - 2f^\pm(\phi_{i+1}) + f^\pm(\phi_{i+2}))^2 + \frac{1}{4} (3f^\pm(\phi_i) - 4f^\pm(\phi_{i+1}) + f^\pm(\phi_{i+2}))^2 . \end{cases} \quad (56)$$

The level set function needs to be reinitialized after each time steps in order to maintain the distance function $|\nabla\phi| = 1$. This is important throughout the simulation to maintain its smooth and well resolved geometrical properties and especially near the interface to obtain

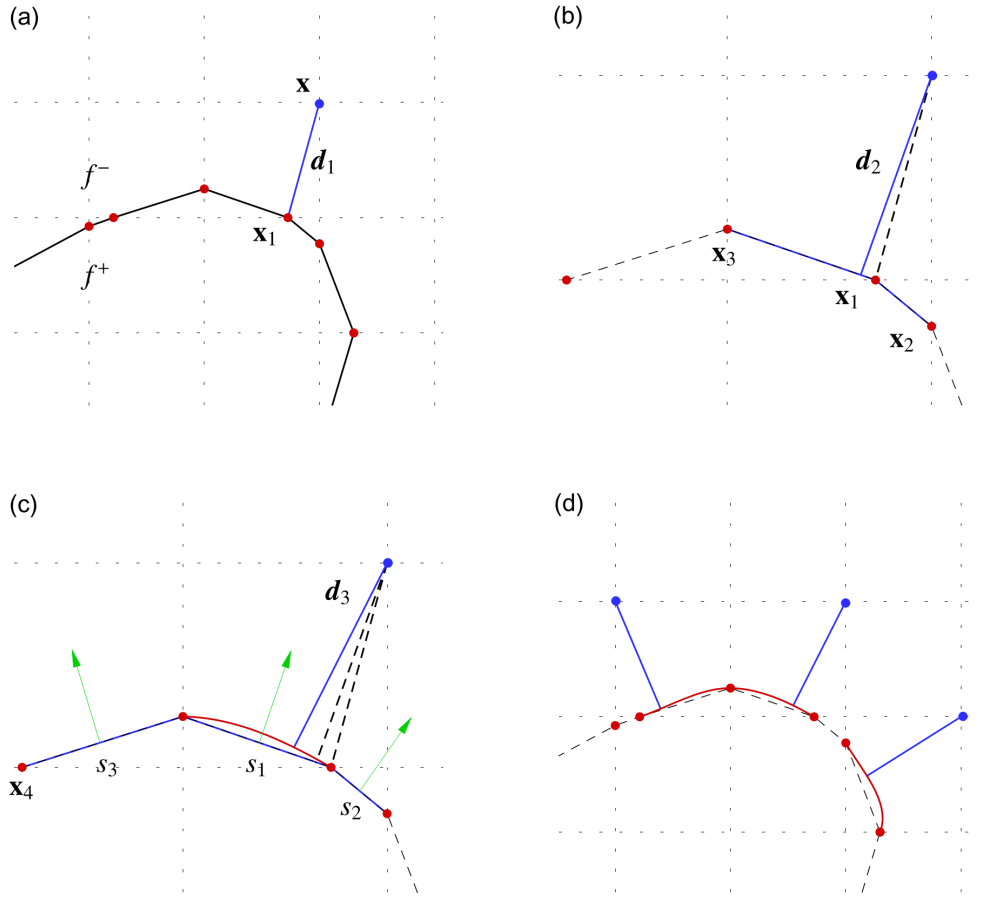


Figure 12: Illustration of stepwise refinement of geometric projection ([54], Fig. 3.): (a) level 1, (b) level 2, (c) level 3 (d) segments represented by smooth curves resulting from level 3 projection.

an accurate interface curvature and normal. The traditional reinitialization is given by

$$\frac{\partial \phi}{\partial \tau_r} + S(\phi_0)(|\nabla \phi| - 1) = 0 . \quad (57)$$

where τ_r is a fictitious time to be solved until steady state and the S_r is a sign function

$$S_r(\phi_0) = \frac{\phi_0}{|\phi_0| + \epsilon} . \quad (58)$$

with a small valued ϵ to avoid singularity.

However, standard methods of PDE based reinitialization has limited accuracy in the calculation of interface topology that lead to mass loss and unphysical interface distortion. To avoid such issue, the geometric projection method recently developed in [54] is incorporated. The method calculates three level of distances, \mathbf{d}_1 , \mathbf{d}_2 and \mathbf{d}_3 by directly projecting the distance from grid points \mathbf{x} onto a set of interpolated interface vectors, \mathbf{x}_p .

$$\begin{aligned} |\mathbf{d}_1(\mathbf{x})| &= \min_p (|\mathbf{x}_p - \mathbf{x}|) \\ \mathbf{d}_2(\mathbf{x}) \cdot \mathbf{t}_l &= 0 \\ \mathbf{d}_3(\mathbf{x}) \cdot \mathbf{t}_p &= 0 , \end{aligned} \tag{59}$$

where $\mathbf{t}_l n$ and $\mathbf{t}_p w$ are tangent vectors to piecewise linear and piecewise polynomial construction of the interface respectively. The final distance function is given by

$$d(\mathbf{x}) = \frac{\phi(\mathbf{x})}{|\phi(\mathbf{x})|} \min_i (|\mathbf{d}_i(\mathbf{x})|) \quad (i = 1, 2, 3) . \tag{60}$$

From this distance function, the interface normal vector is calculated by $\mathbf{n} = \nabla d(\mathbf{x}) / |\nabla d(\mathbf{x})|$ and the interface curvature by $\kappa = -\nabla \cdot \mathbf{n}$ using the standard central differencing scheme. The resulting distance function is shown to have 2nd order accuracy in interface normal and 1st order for the curvature.

The geometric projection reinitialization step is not entirely free of zero level set moving. Thus the selective redistancing technique is applied when updating the original level set function ϕ with the distance function in order to minimize mass error during reinitialization.

$$\phi(\mathbf{x}) = S_h(\phi)d(\mathbf{x}), \tag{61}$$

where

$$S_h(\phi) = \begin{cases} 0, & |\phi| < \epsilon_s \\ 1, & \text{otherwise ,} \end{cases} \quad (62)$$

and ϵ_s is typically chosen to be equal to the grid size.

3.6 Discretization of the Energy Equation and the Temperature Gradient Jump Condition

Second order scheme is used for the spacial discretization of the temperature equation, Eq. 2: 2nd order ENO scheme for the convective term and the 2nd order central difference scheme for the diffusive term. To alleviate the time step limitation of the diffusion term, a semi-implicit Crank-Nicolson scheme is used which yields 2nd order accuracy in time as well. The discretized energy equation is then given by

$$\frac{T^{n+1} - T^n}{\Delta t} = -\mathbf{u} \cdot \nabla T^n + \frac{1}{2} \nabla \cdot (\alpha \nabla T^{n+1}) + \frac{1}{2} \nabla \cdot (\alpha \nabla T^n) , \quad (63)$$

Reorganizing to

$$2T^{n+1} - \nabla \cdot (C \nabla T^{n+1}) = 2T^n - 2\Delta t(\mathbf{u} \cdot \nabla T^n) + \nabla \cdot (C \nabla T^n) , \quad (64)$$

where $C = \Delta t / \alpha$ and the left hand side forms the linear system of equation which is solved using the PARDISO solver.

The discretization at the interface follows the Dirichlet boundary condition method with subcell resolution technique described in [10, 41]. The ghost fluid value of the temperature across the interface is calculated by linear extrapolation with the distance function to obtain second order accurate solution [41]. For example, consider the node i, j where the interface

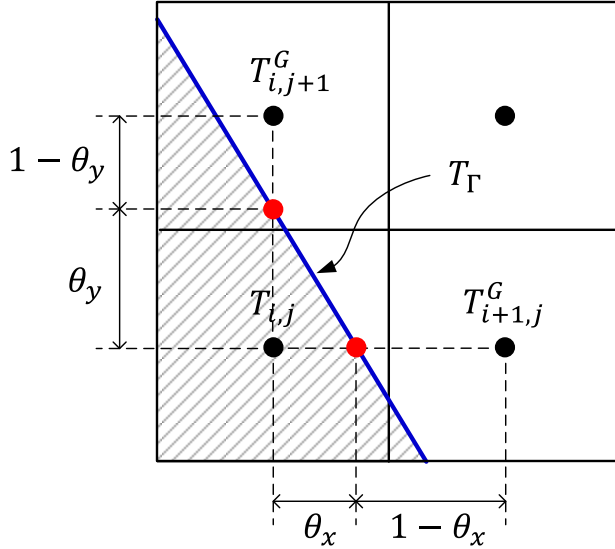


Figure 13: Dirichlet temperature boundary condition at the interface in subcell resolution.

is located as shown in Fig. 13. The ghost fluid values for the temperature at $i + 1, j$ and $i, j + 1$ are equal to

$$T_{i+1,j}^G = T_{i,j} + (T_\Gamma - T_{i,j}) \left(\frac{\Delta x}{\theta_x} \right) ,$$

$$T_{i,j+1}^G = T_{i,j} + (T_\Gamma - T_{i,j}) \left(\frac{\Delta y}{\theta_y} \right) ,$$

where $\theta_x = |\phi_{i,j}| \setminus (|\phi_{i,j}| + |\phi_{i+1,j}|)$ and $\theta_y = |\phi_{i,j}| \setminus (|\phi_{i,j}| + |\phi_{i,j+1}|)$. Since each cell is calculated as a single phase fluid using the sharp interface approach, the thermal diffusivity for each fluid is available on both sides of the interface. The cell center fluid velocity is averaged using the ghost fluid values on the cell edges. Due to the diffused nature of the new velocity jump condition, however, the velocity near the interface can lead to incorrect thermal convection. Such problems are avoided by simply extrapolating the velocity value from the outer most edge of the diffused region towards the interface $\phi = 0$.

The resulting solution of the temperature equation is used to obtain the temperature gradients and the mass flux in Eq. 5 at the interface following the same ghost fluid methodology. The mass flux is required near the interface on both phases to apply the velocity jump con-

dition thus the temperature field is extrapolated normal to the interface. Also similar to the velocity field, the temperature may not represent the correct phase once the interface is updated to a new location and needs to be updated to the correct phase by means as described in [10].

3.7 Discretization of the Momentum Equation

The discretization of the convective term in Eq. 46 is done using the second order ENO scheme[63] while the discretization of the diffusion term is done by the second order central difference. For $u_{i+1/2,j}^*$ and in same fashion for $v_{i,j+1/2}^*$,

$$\begin{aligned} & (uu)_x + (vu)_x \\ &= u_{i+1/2,j}^n (u_{i+1/2,j}^n - u_{i-1/2,j}^n) / dx \\ &+ (v_{i,j+1/2}^n + v_{i,j-1/2}^n + v_{i+1,j+1/2}^n + v_{i+1,j-1/2}^n) (u_{i+1/2,j}^n - u_{i-1/2,j}^n) / 4dy . \end{aligned} \quad (65)$$

Let

$$m(a, b) = \begin{cases} a, & \text{if } |a| \geq |b| \\ b, & \text{otherwise ,} \end{cases} \quad (66)$$

and

$$\begin{aligned} u_L &\equiv u_i - 1/2 + 0.5m(u_i + 1/2 - u_i + 1/2, u_i + 1/2 - u_i + 1/2) \\ u_R &\equiv u_i + 1/2 + 0.5m(u_i + 1/2 - u_i + 1/2, u_i + 1/2 - u_i + 1/2) \\ u_M &\equiv 0.5m(u_L + u_R) , \end{aligned} \quad (67)$$

where

$$m(a, b) \equiv \begin{cases} u_M, & \text{if } u_L \leq 0 \text{ and } u_R \geq 0 \\ u_L, & \text{if } u_M \geq 0 \text{ and } u_L \geq 0 \\ u_R, & \text{if } u_M \leq 0 \text{ and } u_R \leq 0 . \end{cases} \quad (68)$$

3.8 Viscous Term

The viscosity is treated smoothly which greatly simplifies the implementation and is defined using the Heaviside function in Eq. 23

$$\mu(H_\epsilon) = \mu_g H_\epsilon + \mu_l(1 - H_\epsilon) , \quad (69)$$

and is implemented in the diffusion term by harmonic averaging of the coefficients. A formula for sharp treatment of the viscosity has been proposed in [43] for incompressible flow but the method is very complicated and also inapplicable to the phase change case. Therefore the implementation of viscosity with phase change condition has been restricted to a smooth approach in almost all literature so far. In addition, Gibou noted in [10] that the implicit treatment of the viscous term is not as clear with the velocity jump condition and the ghost fluid method. Thus the explicit scheme is used.

3.9 Time Step Size Restrictions

Time step limits are given for explicit formulation of the projection method and the temperature equation. Adaptive time stepping is performed by calculating the *CFL* conditions at each time step. Stability analysis on the convection-diffusion equations with forward in time and central in space gives two time step criteria, convection dominant and diffusion

dominant.

$$\Delta t \frac{(u_{max} + v_{max})^2}{4\alpha} \leq 1, \quad (70)$$

$$\Delta t \frac{2\alpha}{\left(\frac{1}{\Delta x^2} + \frac{1}{\Delta y^2}\right)} \leq 1. \quad (71)$$

where α is the diffusive coefficient for the Navier-Stokes equation and the temperature equation. Not required but sufficiently necessary condition is the grid Peclet number which gives restriction in the grid size as

$$\frac{(U_{max} + V_{max})^2}{\alpha \left(\frac{1}{\Delta x^2} + \frac{1}{\Delta y^2}\right)} \leq 8. \quad (72)$$

The capillary time step constraint is also considered and is given by

$$\Delta t \sqrt{\frac{\sigma\pi}{\rho_l + \rho_g}} \frac{2}{\Delta x^{3/2}} \leq 1. \quad (73)$$

The time limitation can be quite stringent for small mesh sizes which can be improved with implicit formulation of the diffusive terms.

The minimum time step restriction from the Navier-Stokes and energy equation is chosen after each time step for the next time iteration with a *CFL* number of 0.5 to ensure stability of the solution.

$$\Delta t^{n+1} = \frac{1}{2} \min(\Delta t_{CFL}). \quad (74)$$

3.10 Solution Algorithm

The numerical calculation procedure is summarized by the flow chart in Fig. 14.

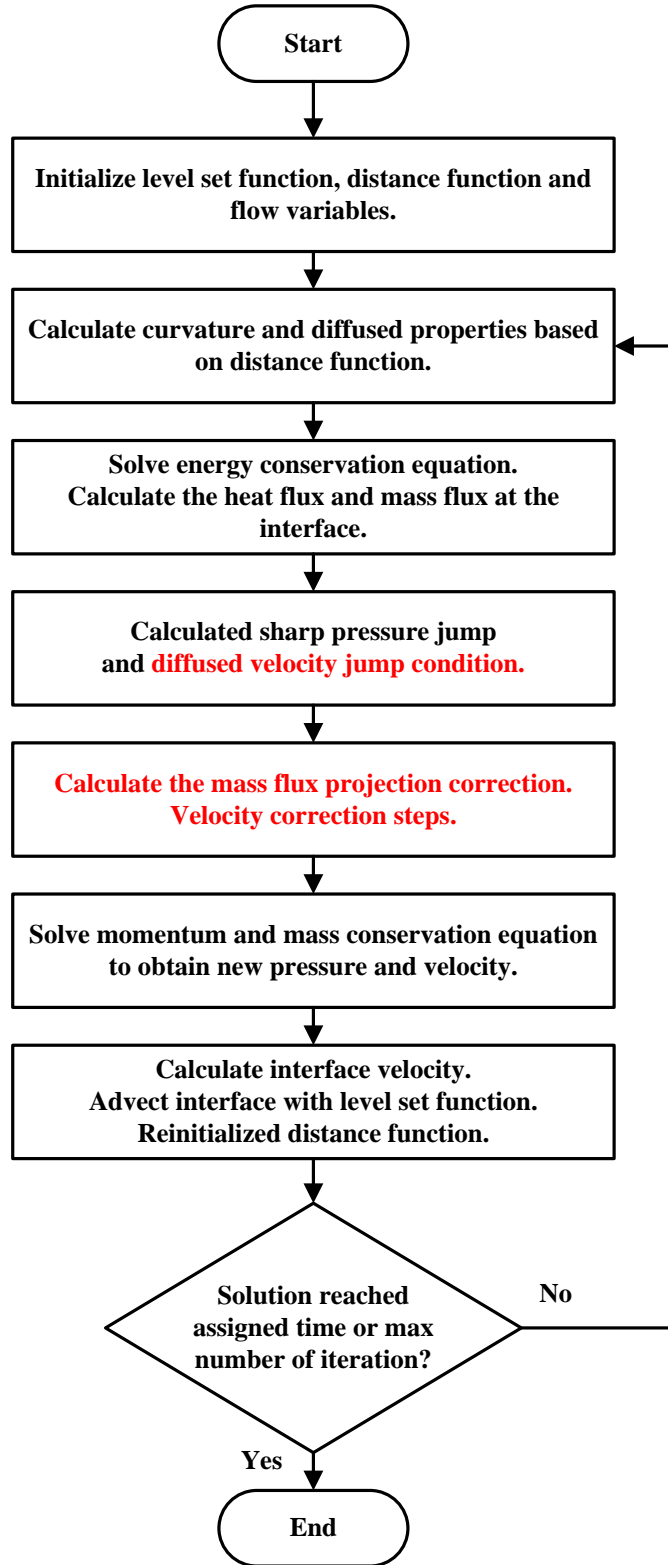


Figure 14: Flow chart of the solution algorithm. The new methods are highlighted in red.

4 Verification Cases: One-dimensional Interface and Two-dimensional Bubble

In order to determine the validity of the new numerical method, a series of one-dimensional and two-dimensional problems are solved. For each of dimension, I start with constant mass flux cases to isolate the effect of the velocity jump condition from the temperature solution and the mass flux calculation. For these cases, the solutions from the new method are compared with those of the sharp ghost fluid method and standard diffused mass flux distribution.

Then well-known verification problems, such as one-dimensional Stefan problem, one-dimensional sucking interface problem and two-dimensional bubble evaporation in superheated liquid problem, are considered. Complete governing equations that were considered in the numerical formulation for the phase change formulation are solved with physical parameters of water as the working fluids. The conditions for the verification cases are summarized in Table. 1.

Table 1: *Conditions for verification cases.*

	System	Working fluid	Phase change	Mass flux	ΔT or \dot{m}
Case 1.	1-D	dimensionless	evap.	const.	1
Case 2.	1-D	saturated water ($p = 101.3\text{kPa}$)	evap.	heated wall	25K
Case 3.	1-D	saturated water ($p = 101.3\text{kPa}$)	evap.	superheated liq.	25K
Cases 4.1-4.2.	2-D bubbles	saturated water ($P_r = 0.99$)	evap./cond.	constant	± 0.01
Cases 4.3-4.4.	2-D bubbles	saturated water ($p = 101.3\text{kPa}$)	evap./cond.	constant	± 0.001
Case 4.5.	2-D bubbles ($\sigma = 0$)	saturated water ($p = 101.3\text{kPa}$)	cond.	constant	-0.001
Case 5.	2-D bubble	saturated water ($p = 101.3\text{kPa}$)	evap.	superheated liq.	2K

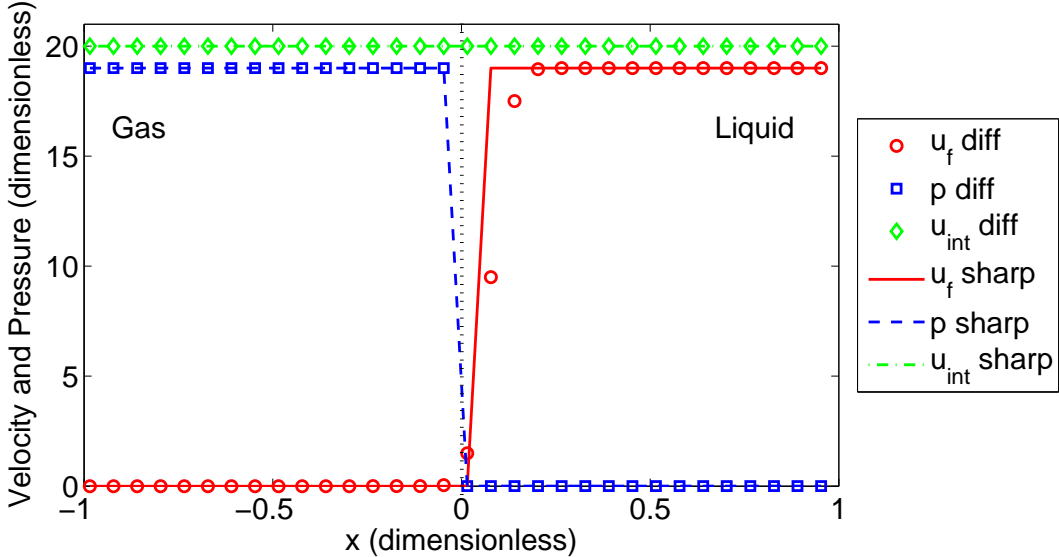


Figure 15: Case 1. Comparison of velocity jump, pressure jump and interface velocity for 1-D constant mass flux evaporation case between sharp and new diffused interface method. The interface is asymmetrically diffused towards the liquid phase.

4.1 Case 1. One-dimensional Phase Change with Constant Mass Flux

A one-dimensional phase change problem with a constant mass flux is considered first to verify the result of the diffused velocity jump distribution. The level set function is defined as $\phi(x) = x - 1$ within a domain $[-1, 1]$ so that the gas phase is on the left-hand side, the liquid phase on the right-hand side and the interface is located at $x = 0$. The $x = -1$ boundary is treated as a wall whereas the $x = 1$ boundary is kept open for the fluid to exit freely with Dirichlet pressure boundary condition of $P = 0$. The densities are taken as $\rho_g = 1$, $\rho_l = 20$ and the $\dot{m} = 1$. Since the gas phase is bounded, the diffused interface is biased toward the liquid phase and the thickness of the diffused region is chosen to be about six times the grid size just for the current case. A mesh size of 64 is used. The gas phase is at rest while the liquid phase experiences a jump in velocity. The pressure jump condition includes only the mass flux term. The exact solution for the pressure jump, the velocity jump and the interface velocity are -19, 19 and 20, respectively. Fig. 15 compares the result

for the sharp ghost fluid method and the new diffused interface method. It shows that the velocity jump is smoothly and symmetrically distributed about the center of asymmetrically diffused interface region and the pressure jump due to mass flux is sharp. The interface velocity is constant throughout the domain. For this 1-D case, both methods are able to calculate the precise amount of jump for all variables.

4.2 Case 2. One-dimensional Stefan Problem

Consider the 1-D Stefan problem illustrated in Fig. 16. In this case, the gas-liquid interface is initially at rest near the left end of the computational domain $x = 0$ where the wall temperature is set constant at T_{wall} and the interface temperature is at T_{sat} . The liquid phase is at a constant temperature of T_{sat} . The gas phase temperature gradient at the interface is thus responsible for the mass flux. The interface is pushed away from the wall due to evaporation. Assuming that the gas phase temperature is fully developed (linear) and the liquid phase temperature is at a constant saturation temperature, the exact solution for the interface position and the temperature profile is given by [64],

$$d_\Gamma(t) = 2\lambda\sqrt{\alpha_g t} \quad (75)$$

$$T(x, t) = T_{wall} + \left(\frac{T_{sat} - T_{wall}}{\text{erf}(\lambda)} \right) \text{erf} \left(\frac{x}{2\sqrt{\alpha_g t}} \right) \quad (76)$$

$$\lambda \exp(\lambda^2) \text{erf}(\lambda) = C_{p,g} \frac{(T_{wall} - T_{sat})}{h_{lg} \sqrt{\pi}}. \quad (77)$$

where $d_\Gamma(t)$ is the interface location, λ the growth constant, α_g the gas thermal diffusivity, $C_{p,g}$ the gas heat capacity and $\text{erf}(x)$ the error function. For current case, the fluid properties are taken as the saturated water at the pressure of 101.3kPa, given in Table 2 and $\Delta T = T_{wall} - T_{sat} = 25K$.

Fig. 18 shows the temperature profile at $t = 0.2s$ calculated for three difference grid res-

Table 2: Saturated water properties at $p = 101.3kPa$

Phase	ρ [kg/m ³]	μ [μ Pa· s]	C_p [J/kgK]	k [W/mK]	h_{lg} [kJ/kg]	σ [N/m]	T_{sat} [K]
Vapor	0.597	12.6	2030	0.025	2260	0.059	373.15
Liquid	958.4	280	4216	0.679			

solutions (32, 64, 128) and compared with the analytical solution. In Fig. 17, the interface location is plotted versus time for the three grid resolutions and the analytical solution. It can be seen that the numerical solutions agree well with the analytical solution and the overall numerical scheme shows approximately second order accuracy in space as shown in Fig. 19.

4.3 Case 3. One-dimensional Sucking-interface Problem

Another important validation case in 1-D is the problem of evaporation driven by the liquid superheat. In this problem, the heat source for evaporation comes from the superheated liquid. Other conditions are the same as for the previous problem in section 4.2. The gas phase is on the left-hand side bounded by the wall and the liquid phase on the right-hand side can exit freely. The interface is initially located close to the left end $x = 0$. The liquid phase is initially superheated homogeneously by $\Delta T = T_\infty - T_{sat} = 25K$ and the gas phase and the wall temperature are kept constant at the saturation temperature $T = T_{sat}$. As the bubble evaporates, a thermal boundary layer develops in the liquid phase and the interface expands to the right. The schematic of the problem is shown in Fig. 20. An analytical solution, similarity has is provided in [7].

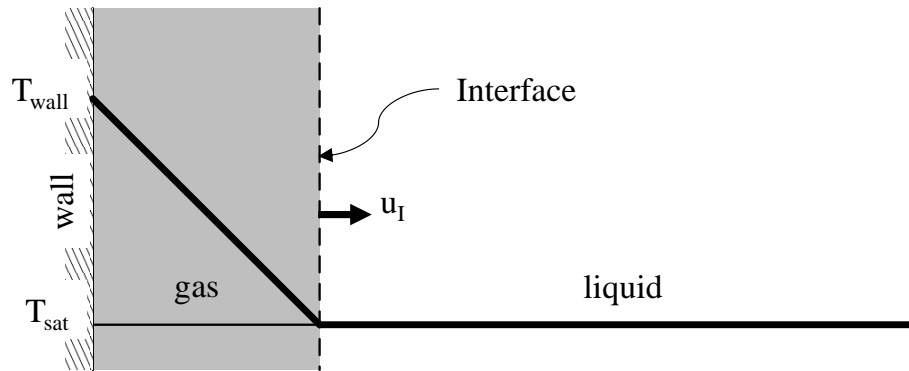


Figure 16: *Case 2.* Schematic of 1-D Stefan problem.

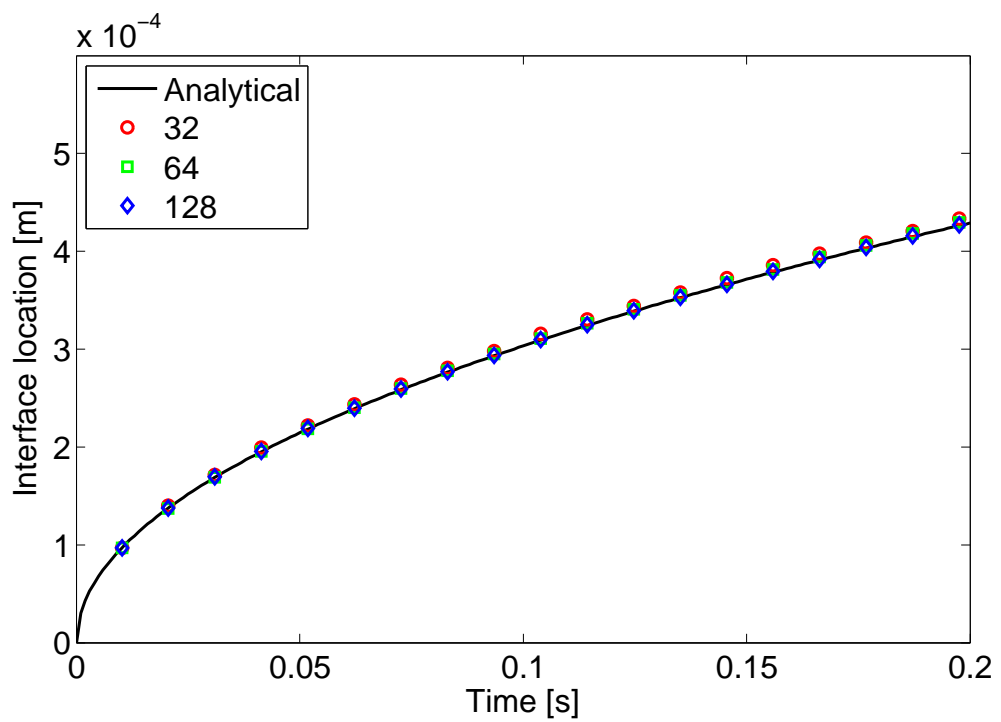


Figure 17: *Case 2.* Time evolution of interface location for 1-D Stefan problem with saturated water at $p = 101.3 \text{ kPa}$ and $\Delta T = 25 \text{ K}$. Three grid resolutions (32, 64, 128) are plotted on top of the analytical solution (solid line).

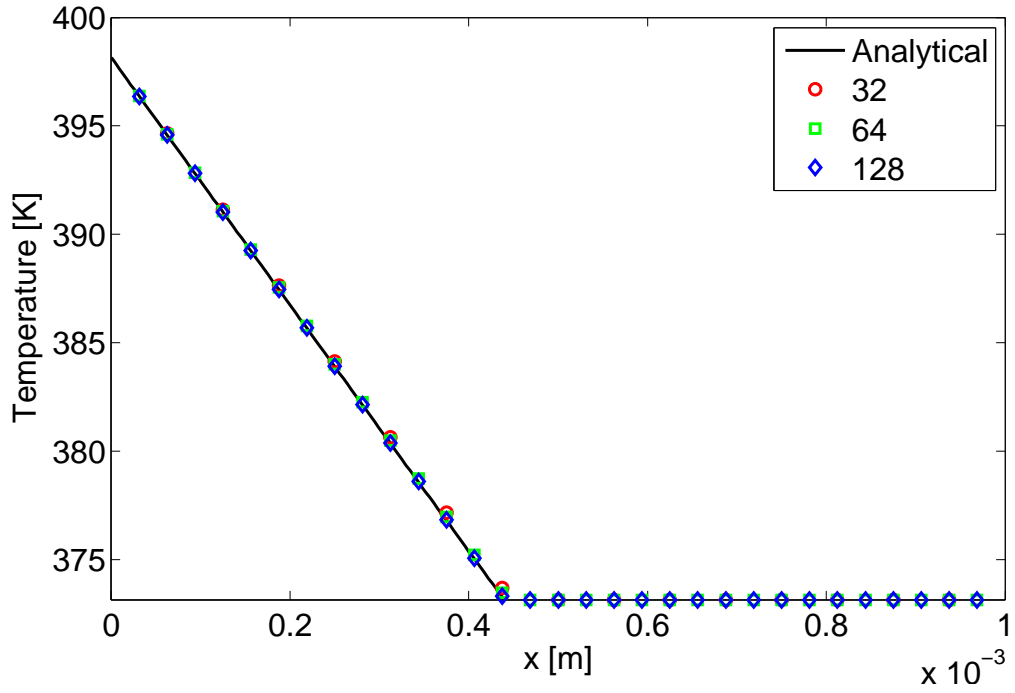


Figure 18: *Case 2.* Temperature profile for 1-D Stefan problem with saturated water at $p = 101.3\text{kPa}$ and $\Delta T = 25\text{K}$. The time is at $t = 0.2\text{s}$. Three grid resolutions(32, 64, 128) are plotted on top of analytical solution(solid line).

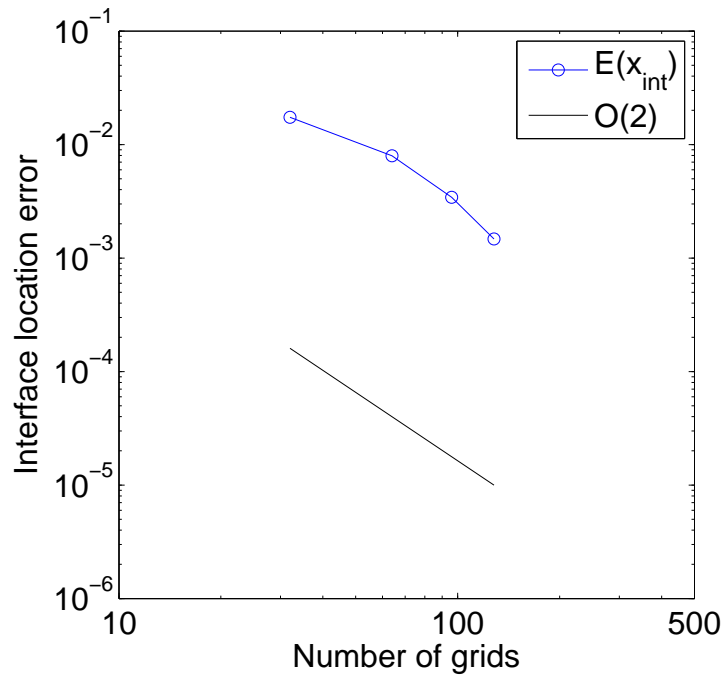


Figure 19: *Case 2.* Order of convergence for 1-D Stefan problem with respect to interface location at $t = 0.2\text{s}$. The errors are computed for four grid resolutions (32, 64, 96, 128).

$$\begin{aligned}
\frac{\partial T}{\partial t} + (u_l - u_\Gamma) \frac{\partial T}{\partial \xi} &= \frac{1}{\text{Pe}} \frac{\partial^2 T}{\partial \xi^2} \\
T(\xi = 0, t) &= T_{sat} \\
T(\xi \rightarrow \infty, t) &= T_\infty \\
T(\xi \rightarrow \infty, t = 0) &= T_\infty ,
\end{aligned} \tag{78}$$

where u_l is the liquid velocity, u_Γ the interface velocity, Pe the Peclet number and ξ is a moving coordinate such that $\xi = 0$ at the interface. Using similarity variable $\eta = \sqrt{1/2\alpha_l t}\xi$, the equation is transformed to a non-linear ODE which must be solved numerically with sufficient resolution to ensure its convergence. The exact interface location is calculated as

$$\xi = x + \int_0^t u_\Gamma(t) dt . \tag{79}$$

The interface velocity is defined as

$$u_\Gamma = \left. \frac{k_l}{\rho_g h_{lg}} \frac{\partial T}{\partial \xi} \right|_{\xi=0} , \tag{80}$$

where k_l is the liquid thermal conductivity, ρ_g the gas density and h_{lg} the latent heat of evaporation. The problem of evaporation driven by liquid superheat is considerably more challenging than the Stefan problem because of the presence of a thermal boundary layer on the liquid side where diffusion competes with interface expansion.

Calculation of the temperature gradient at the interface requires subcell resolution, which depends on the accuracy of the distance function $d(\mathbf{x})$ as well as the temperature values adjacent to the interface. The accuracy of the liquid velocities near the interface is also crucial for the accurate calculation of heat convection and the subsequent calculation of the mass flux. For this reason, the bulk liquid velocity at the boundary of the diffused interface

is taken and extrapolated towards the interface using the method described in section 3.6. The thermal boundary layer at $t_0 = 0.1\text{s}$ (start of this simulation) is $\delta_{th} = 0.476\text{mm}$ which needs to be resolved sufficiently. Three grid sizes (64, 128, 256) are used to check grid convergence, which corresponds approximately to 3, 6 and 12 grid points inside the initial thermal boundary layer. Water properties in Table 2 is used again as the working fluid.

In Fig. 21, the time evolution of the interface is plotted. It shows that the numerical solution converges to the exact solution and is very accurate for the high grid resolution case. The temperature profile at $t = 0.9\text{s}$ for numerical solutions with three grid sizes are compared with the exact solution in Fig. 22. In Fig. 23, the error in the interface location shows about second order of accuracy in with respect to space. I found that for this example, the numerical error accumulates quickly and can show poor results when the solution is under-resolved or when a diffusive scheme such as the first order upwind scheme is used for the temperature equation. Thus the extrapolation of liquid velocity within the diffused region is vital for obtaining an accurate solution.

4.4 Cases 4.1-4.5. Two-dimensional Bubble Phase Change with Constant Mass Flux

I now move on to two-dimensional cases and first consider the constant mass flux evaporation and condensation of a bubble depicted in Fig. 24. Within a scaled computational domain $[0.5, -0.5] \times [0.5, -0.5]$, the initial interface is defined by $\phi(x, y) = r_0 - \sqrt{(x - x_0)^2 + (y - y_0)^2}$ where $r_0 = 0.25$ for a shrinking bubble, $r_0 = 0.1$ for expanding bubble and the center is located at $x_0 = y_0 = 0$. The length scale is taken as $L = \sqrt{\sigma/(g|\rho_g - \rho_l|)}$. Here, the properties of the fluids are taken at the saturated condition for water at near critical pressure (Table 3) and 1atm (Table 2). Clearly, the latter condition is more complicated due to the large density difference and the high surface tension. Both conditions are tested here to

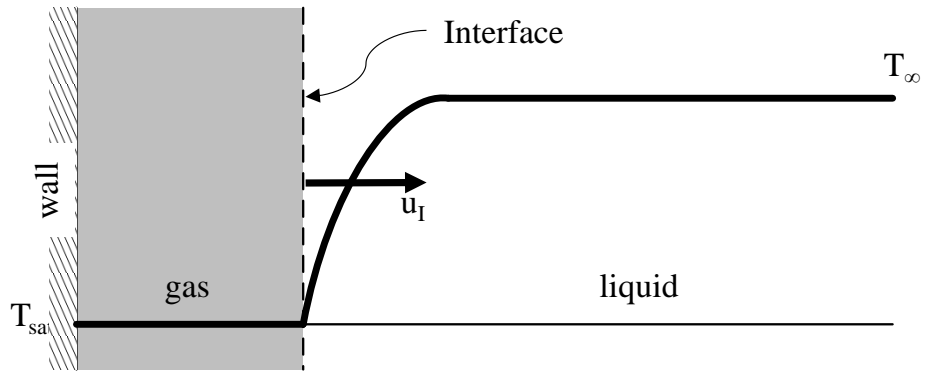


Figure 20: *Case 3.* Schematic of 1-D sucking interface problem.

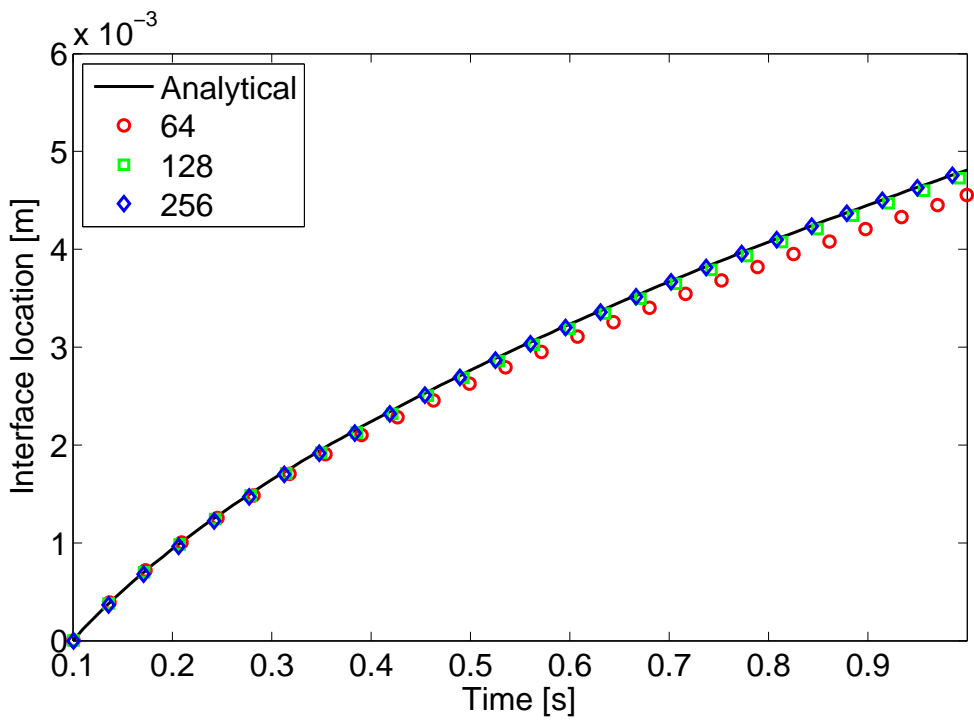


Figure 21: *Case 3.* Time evolution of interface location for 1-D sucking interface problem with saturated water at $p = 101.3\text{kPa}$ and $\Delta T = 25\text{K}$. Three grid resolutions (64, 128, 256) are plotted on top of analytical solution(solid line)

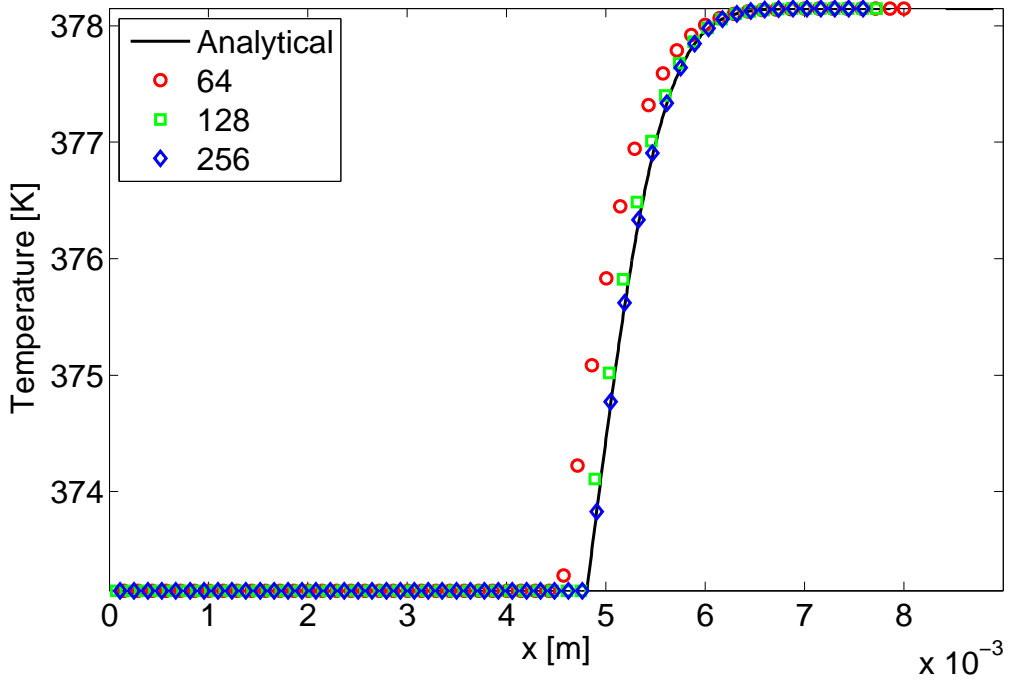


Figure 22: *Case 3.* Temperature profile for 1-D sucking-interface problem with saturated water at $p = 101.3\text{kPa}$ and $\Delta T = 25\text{K}$. The time is at $t = 0.9\text{s}$. Three grid resolutions (64, 128, 256) are plotted on top of analytical solution (solid line).

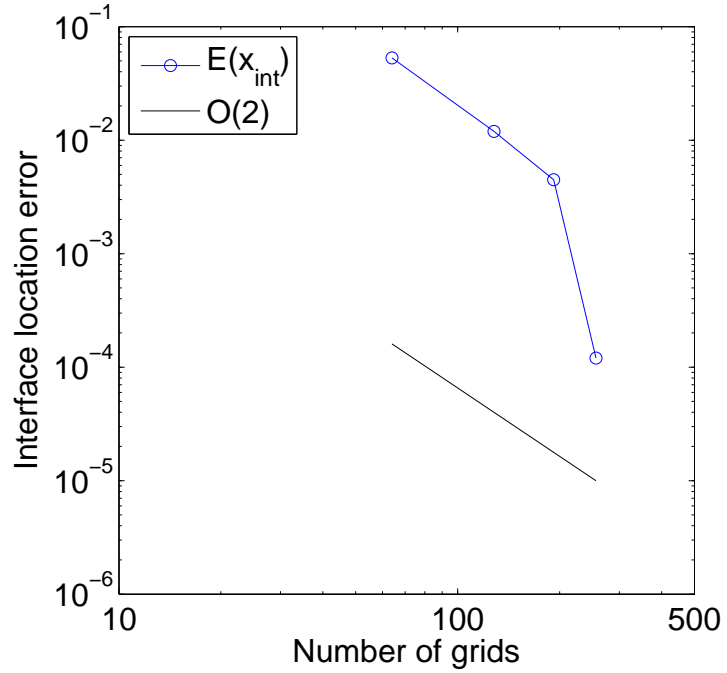


Figure 23: *Case 3.* Order of convergence for 1-D sucking-interface problem with respect to interface location at $t = 0.9\text{s}$. The errors are computed for four grid resolutions (64, 128, 192, 256).

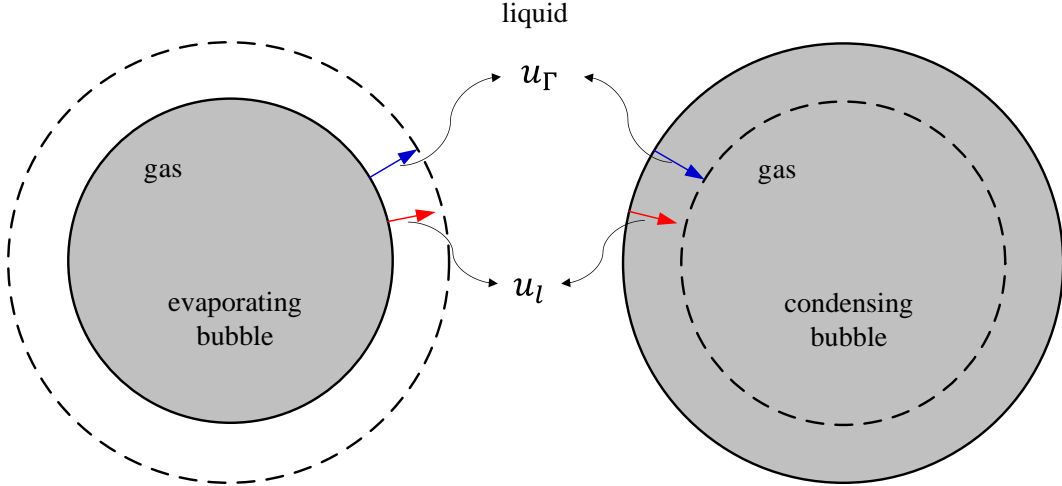


Figure 24: *Case 4.* Schematics of two-dimensional bubble condensation and evaporation problems.

Table 3: Saturated water properties at near critical pressure, $P_r = 0.99$.

Phase	ρ [kg/m ³]	μ [μ Pa· s]	C_p [J/kgK]	k [W/mK]	h_{lg} [kJ/kg]	σ [N/m]	T_{sat} [K]
Vapor	242.7	32.38	3520	0.538			
Liquid	402.4	46.7	2180	0.545	276.4	0.00007	646

validate for both bubble evaporation and condensation. Note that droplet cases can present with even more stringent and time consuming conditions due to the large gas phase velocity compared to the interface velocity (three orders of magnitude larger for properties in Table 2) and will not be considered. The constant mass fluxes for condensation and evaporation are $\dot{m} = -0.01$ and 0.01 for near critical pressure condition and $\dot{m} = -0.001$ and 0.001 for pressure at 1atm. Since gas phase is stationary, the exact solutions for the interface velocity are given by

$$\mathbf{u}_\Gamma = \frac{\dot{m}}{\rho_g} \mathbf{n} . \quad (81)$$

The results for three numerical schemes are presented in comparison, the new diffused interface, ghost fluid method with mass flux projection correction, the sharp interface ghost fluid method and the conventional diffused mass source approach. They will be referred to as DGFM/MPCC, SGFM and SDI. As described in chapter 3, the diffused region is assigned

to be less than two cells thick in the outer liquid phase. Three grid sizes are used, 32×32 , 64×64 , 128×128 , and all plots other than grid convergence plots are based on the medium resolution runs.

The temporal evolution of the averaged bubble radius is plotted in Fig. 25 and Fig. 26. The numerical bubble radius is evaluated as the average of the distances from the bubble center, \mathbf{x}_0 to the interfacial points, $\mathbf{x}_{p,n}$ computed as

$$R_{av} = \frac{1}{N} \sum_{n=1}^N |\mathbf{x}_{p,n} - \mathbf{x}_0| , \quad (82)$$

where N is the total number of interface points. It is quite clear that the performance of different schemes depends strongly on fluid properties, specifically the density difference. For water at 1 atm, a simple diffused mass flux distribution cannot obtain the correct rate of phase change. The new diffused interface method on the other hand shows higher accuracy than the sharp interface method. Also Fig. 27 shows that the bubble shape is more smooth and symmetrical compared to the sharp interface method.

The comparison between sharp and diffused methods with regards to the temporal evolution of the maximum pressure difference for the vapor bubble at 1 atm saturated pressure is plotted in Fig. 28. The sharp method experiences large oscillations whereas my diffused approach shows a smoother pressure profile throughout the simulation.

The rate of grid convergence is plotted in Fig. 29. It can be seen that while all methods are approximately first order accurate, the absolute error is smaller for the new approach. Because curvature calculation is generally not smooth when based on the classical reinitialization, a more accurate schemes that produces smoother curvature solutions are essential for the mass flux projection correction to be effective, such as the geometric projection method [54].

In order to further investigate the effect of sharp and diffused velocity conditions, additional

tests without the surface tension term have been performed using saturated water at $P = 101.3\text{kPa}$ condition. In Fig. 30, the gas phase velocity fields are compared after just one time step and the interface has not moved from the perfectly circular initial shape. Similar to the surface tension force, the velocity jump condition also exhibits parasitic current near the interface. The overall magnitude is similar for both methods but it can be seen that the sharp interface jump creates large peaks of spurious velocity adjacent to the interface whereas the new diffused method shows smoother currents. The resulting interface velocity field is shown in Fig. 31 and as expected, interface velocity is smoother for current method. Fig. 32 shows the shape evolution of the condensing bubble of water with sharp velocity jump and diffused velocity jump. It can be seen that the diffused velocity jump creates more smooth and symmetric deformations.

4.5 Case 5. Two-dimensional Bubble Evaporation in Superheated Liquid

Two-dimensional evaporating bubble case is analogous to the 1-D problem of evaporation due to liquid superheat described in section 4.3. Initially at $t = 0$, an infinitesimally small gas phase bubble is placed within the superheated liquid and the temperature inside the gas phase is assumed to be constant at T_{sat} and the liquid is superheated at $T_\infty = T_{sat} + \Delta T$. The gas phase spontaneously begins to evaporate and thermal boundary is formed on the liquid side near the interface. Thus the bubble expands in the amount determined by the heat flux from the liquid. Following the procedure described in [65], we derived an exact, similarity solution for the cylindrical, axisymmetric problem, in the following form

$$R = 2\beta\sqrt{\frac{1}{Pe}t}, \quad (83)$$

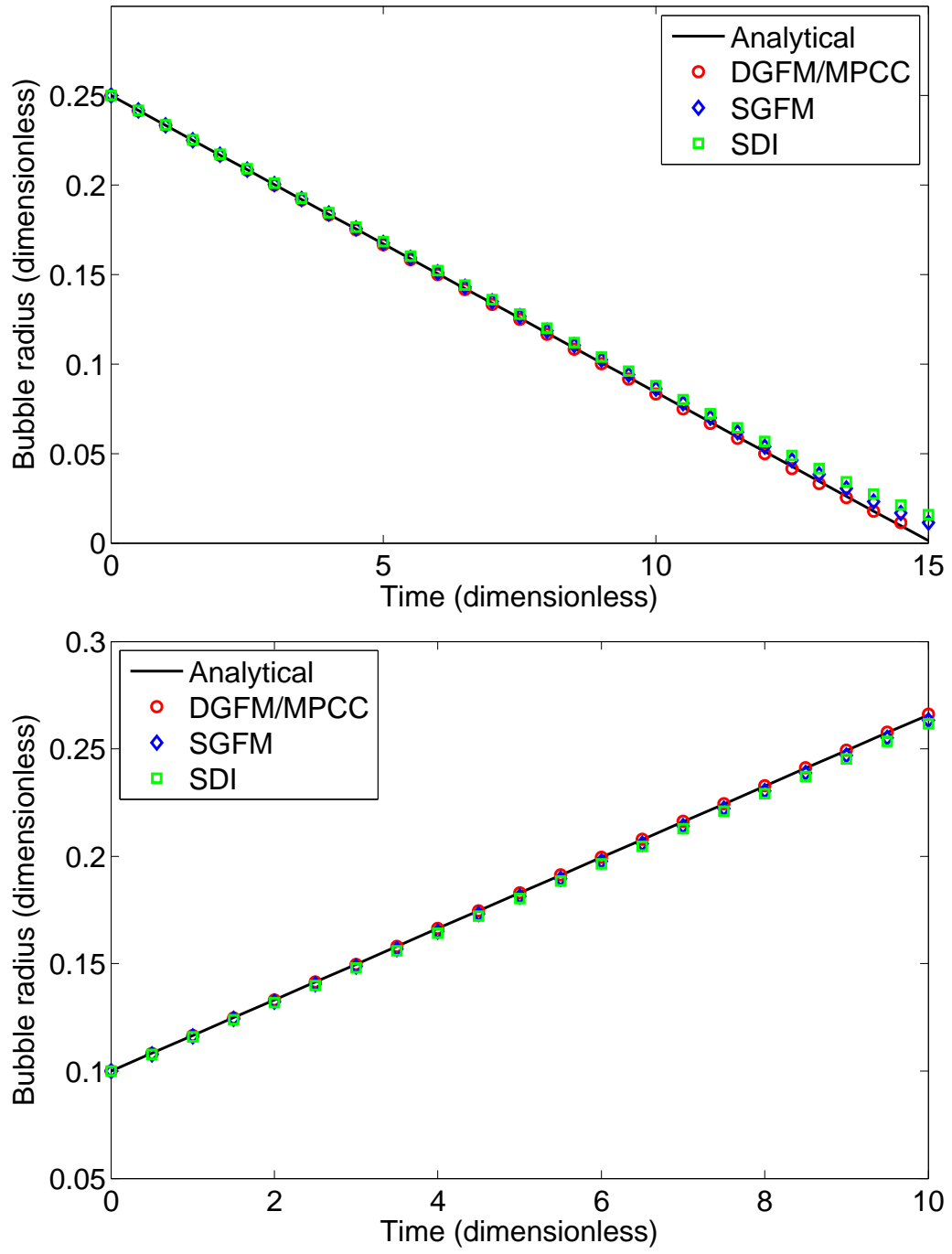


Figure 25: Cases 4.1-4.2. Time evolution of averaged bubble radius for condensation (top) and evaporation (bottom) of saturated water at $P_r = 0.99$ with constant $\dot{m} = -0.01$ and $\dot{m} = 0.01$, respectively. Results are for 64×64 grid resolution.

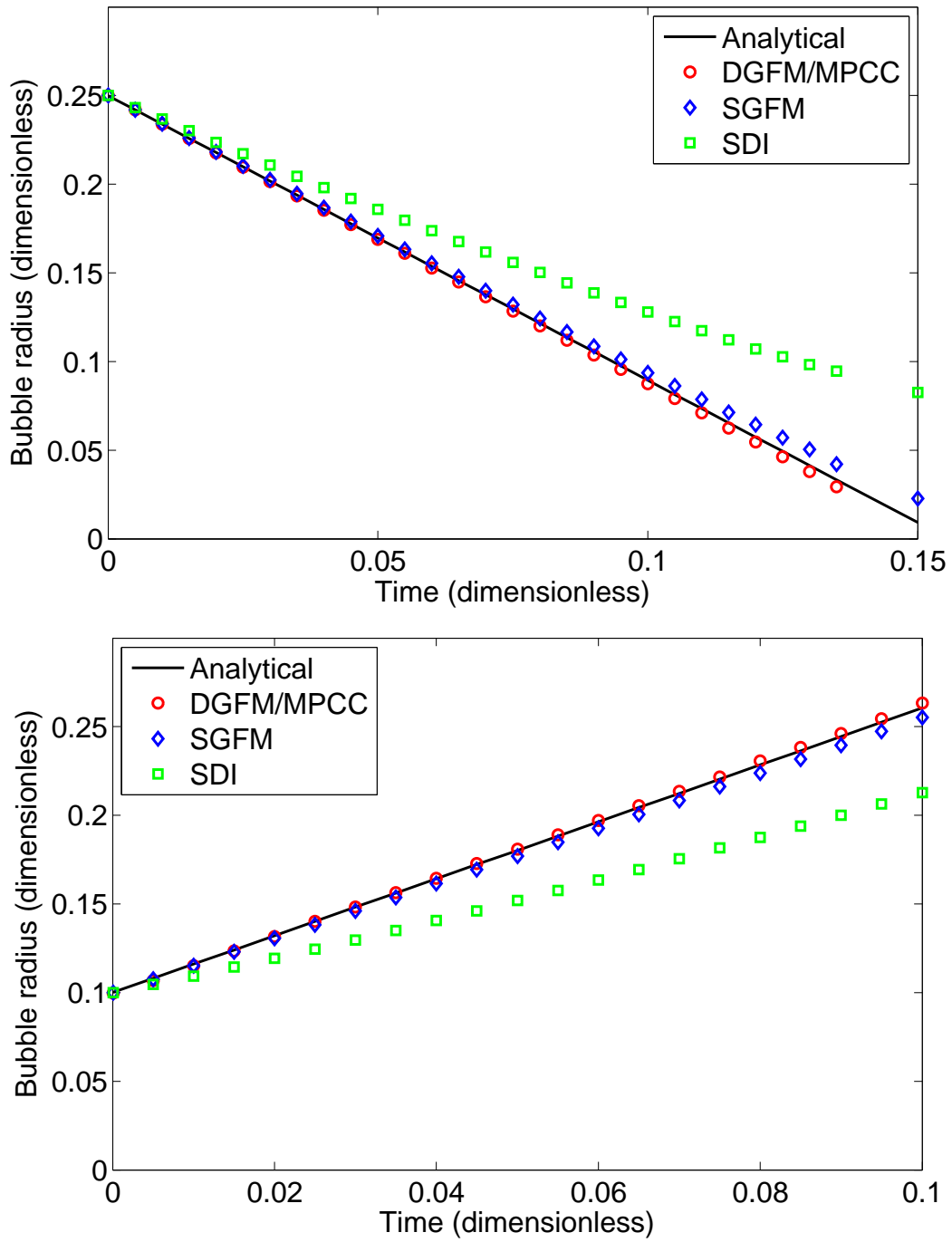


Figure 26: Cases 4.3-4.4. Time evolution of averaged bubble radius for condensation (top) and evaporation (bottom) of saturated water at $P = 101.3\text{kPa}$ with constant $\dot{m} = -0.001$ and $\dot{m} = 0.001$, respectively. Results are for 64×64 grid resolution.

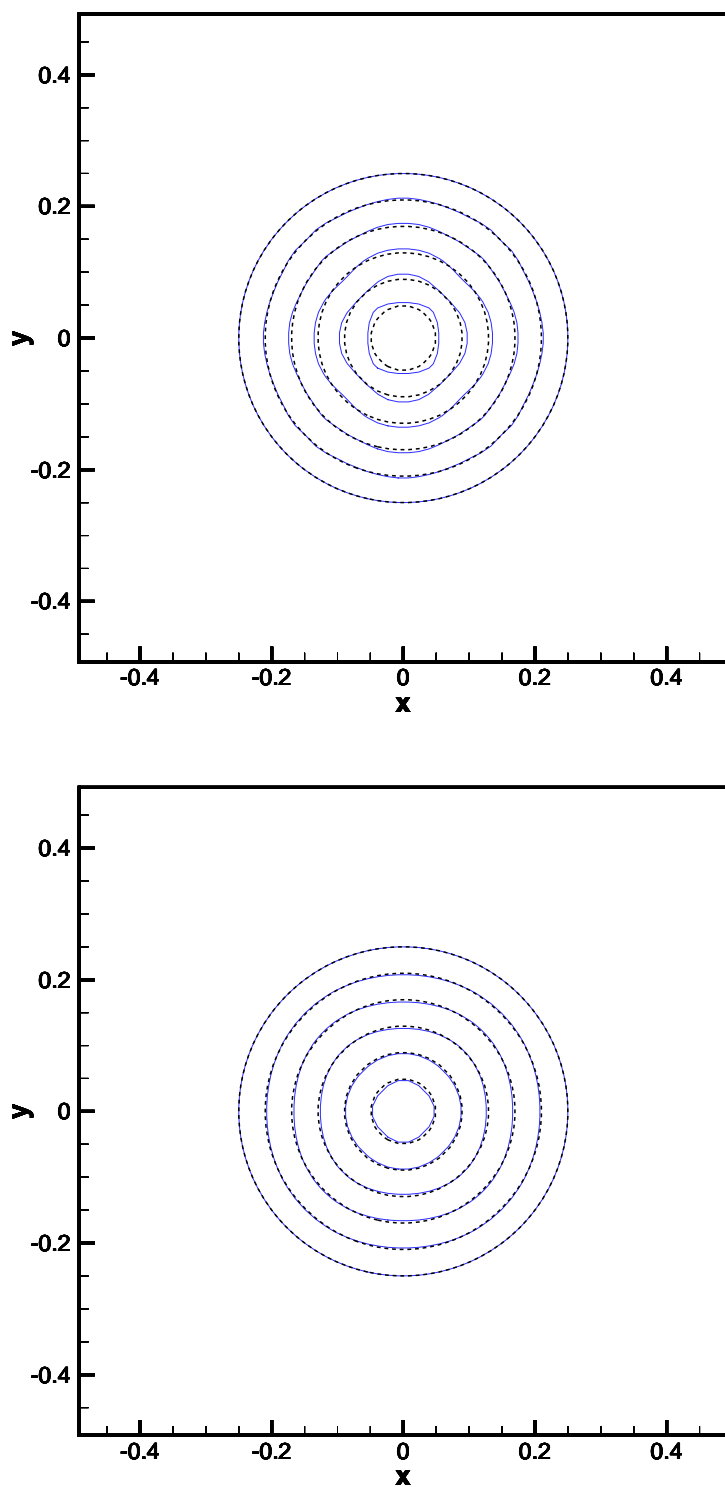


Figure 27: *Case 4.3.* Shape of condensing bubble with DGFM/MPCC (top) and SGFM (bottom). Working fluid is saturated water at $P = 101.3\text{kPa}$ and constant $\dot{m} = -0.001$.

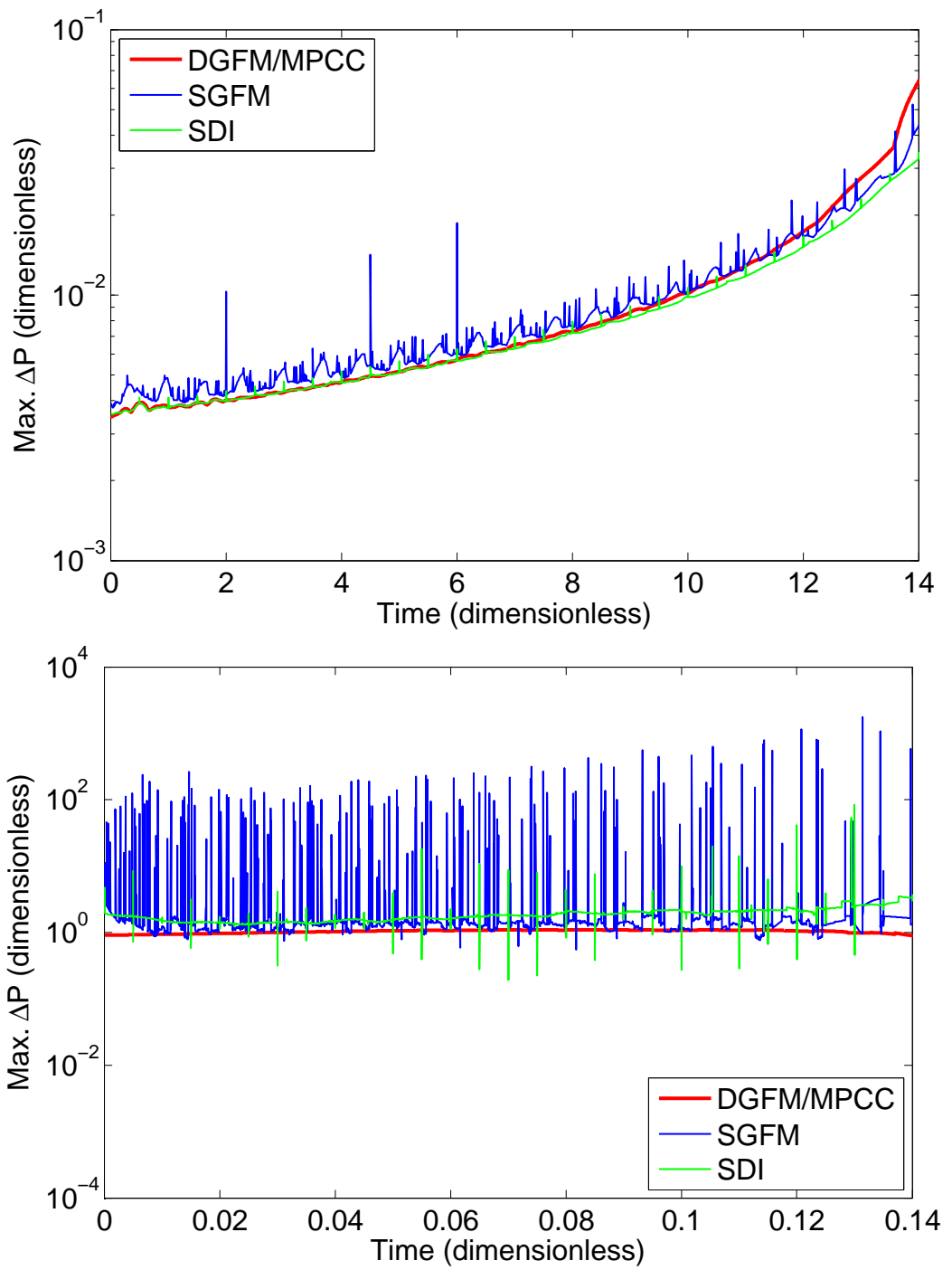


Figure 28: Cases 4.1, 4.3. Time evolution of maximum pressure difference for condensing bubble with saturated water at $P_r = 0.99$ (top) and saturated water at $P = 101.3\text{kPa}$ (bottom).

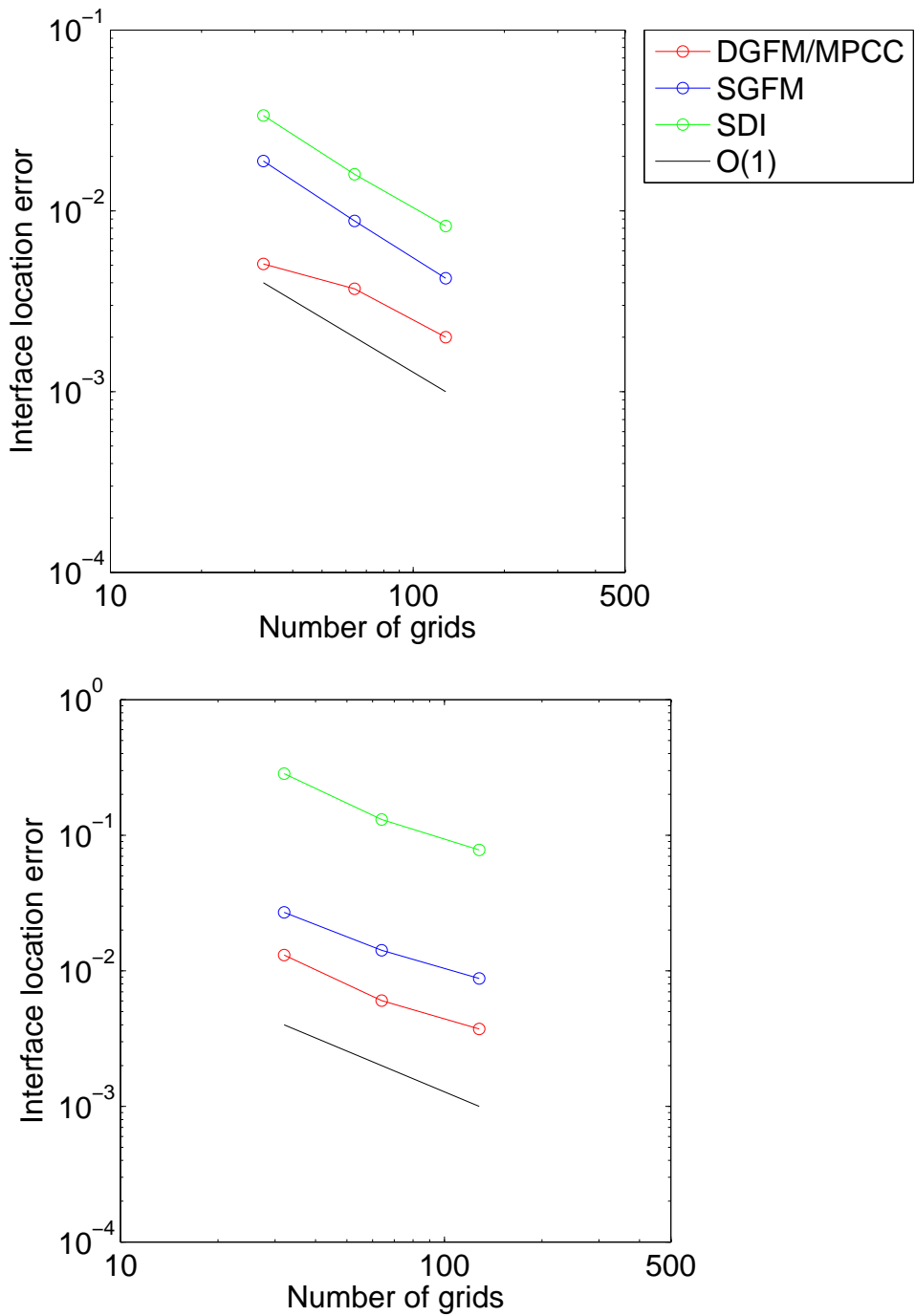


Figure 29: *Cases 4.1, 4.3. Order of convergence for condensation of 2-D water bubble saturated at $P_r = 0.99$ (top) and at $P = 101.3 \text{ kPa}$ (bottom). Errors are calculated with respect to interface location at $t = (\text{final computational time})/2$ computed on three grid resolutions (32, 64, 128).*

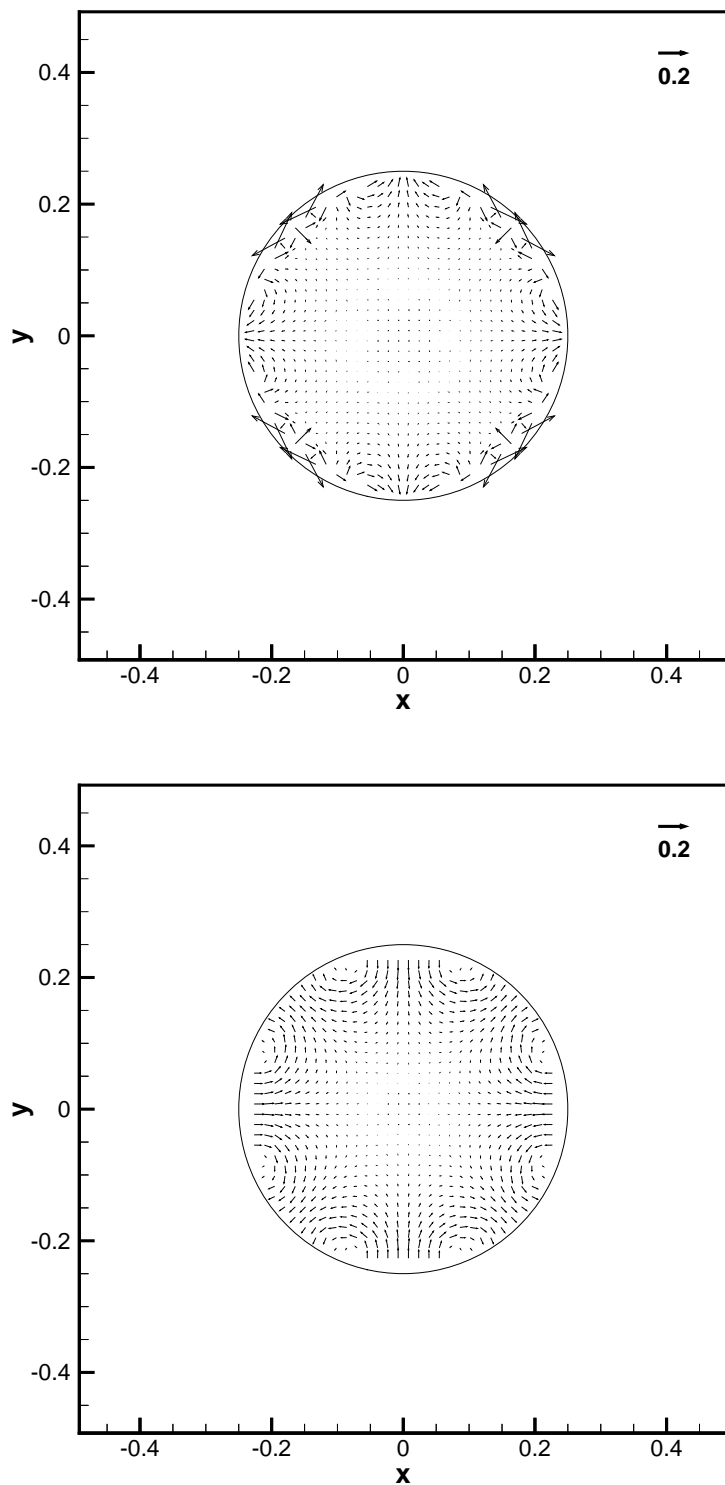


Figure 30: Cases 4.5. Parasitic currents in condensing bubble with no surface tension using sharp velocity jump (top) and diffused velocity jump (bottom) conditions. The working fluid is saturated water at $P = 101.3\text{kPa}$ and constant $\dot{m} = -0.001$.

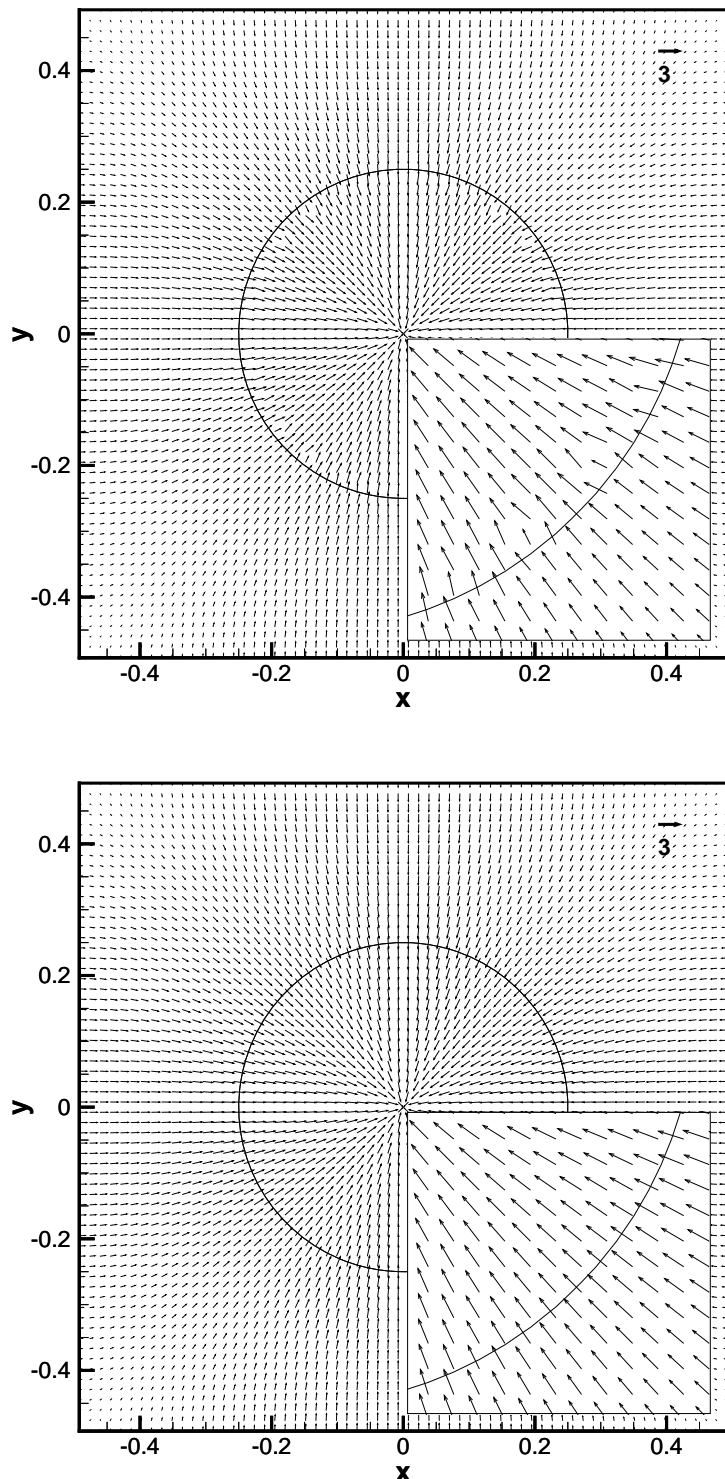


Figure 31: Cases 4.5. Interface velocities for condensing bubble with no surface tension using sharp velocity jump (top) and diffused velocity jump (bottom) conditions. The working fluid is saturated water at $P = 101.3\text{kPa}$ and constant $\dot{m} = -0.001$.

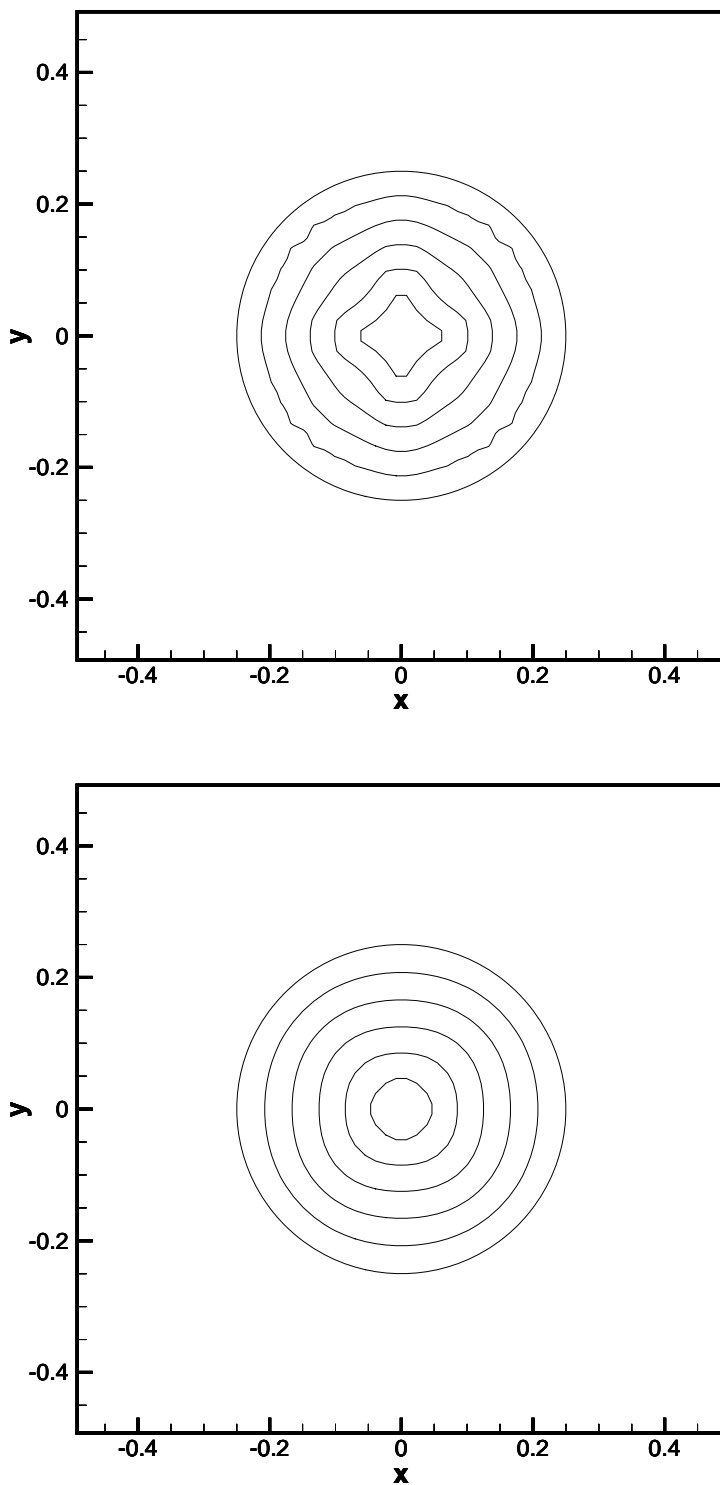


Figure 32: Cases 4.5. Shape of condensing bubble with no surface tension using sharp velocity jump (top) and diffused velocity jump (bottom) condition. The working fluid is saturated water at $P = 101.3\text{kPa}$ and constant $\dot{m} = -0.001$.

$$T_l(s) = 1 - 2\beta^2 \rho' \left(\frac{1}{St} + \epsilon \right) \exp(\beta^2) \int_{1-\frac{\beta}{s}}^1 (1-\xi)^{1-2\chi\beta^2} \exp\left(\frac{-\beta^2}{(1-\xi)^2}\right) \frac{1}{(1-\xi)^2} d\xi , \quad (84)$$

$$1 - 2\beta^2 \rho' \left(\frac{1}{St} + \epsilon \right) \exp(\beta^2) \int_0^1 (1-\xi)^{1-2\chi\beta^2} \exp\left(\frac{-\beta^2}{(1-\xi)^2}\right) \frac{1}{(1-\xi)^2} d\xi = 0 . \quad (85)$$

where R is the radius of the bubble, T_l is the temperature field for liquid phase, $\epsilon = 1 - C'_p$ and $\chi = 1 - \rho'$. β is the growth constant which is evaluated through Eq. 85. Simulation has been performed for the water properties given in Table 2 and the temperature difference, $\Delta T = 2\text{K}$. The initial bubble radius and temperature field are taken slightly after the start of the bubble evaporation to avoid singularity in mass flux, in this case, at $t = 23.51 \mu\text{s}$ where the analytical solution for initial radius is $R = 20 \mu\text{m}$. Like the sucking interface problem, the thickness of the thermal boundary layer need to be evaluated in order to determine appropriate grid size. The thermal boundary layer at the interface is defined as,

$$\delta_{th}(t) = R_{th}(t) - R(t) , \quad (86)$$

where R_{th} is the radial distance at which the temperature is equal to $T_l/T_\infty = 0.99$. In the current case, the thermal boundary layer given by the initial temperature profile is $\delta_{th} = 5.2206 \mu\text{m}$. Approximately 2, 4, 8 grid points within the thermal boundary layer have been used and the corresponding mesh sizes are 64×64 , 128×128 , 256×256 . The size of the computation domain is taken as $128 \mu\text{m} \times 128 \mu\text{m}$ and the simulation is run until $R = 40 \mu\text{m}$. Fig. 33 (a) shows the comparison of the evolution of bubble radius between the numerical solution in three grid sizes and the analytical solution. The figure implies good match with the analytical solution and good grid convergence. The interface contour at $t = 53.83 \mu\text{s}$ is plotted in Fig. 33 (b) and shows symmetric bubble deformation. Fig 34 show the convergence with grid refinement and overall it shows around second order accuracy spatially. Fig. 35 (a) and Fig. 35 (b) shows the fluid velocity field and the interface velocity

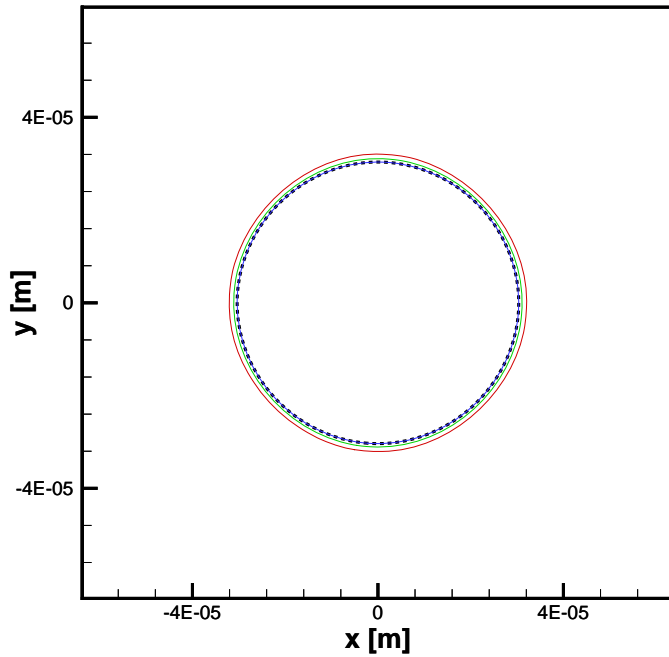
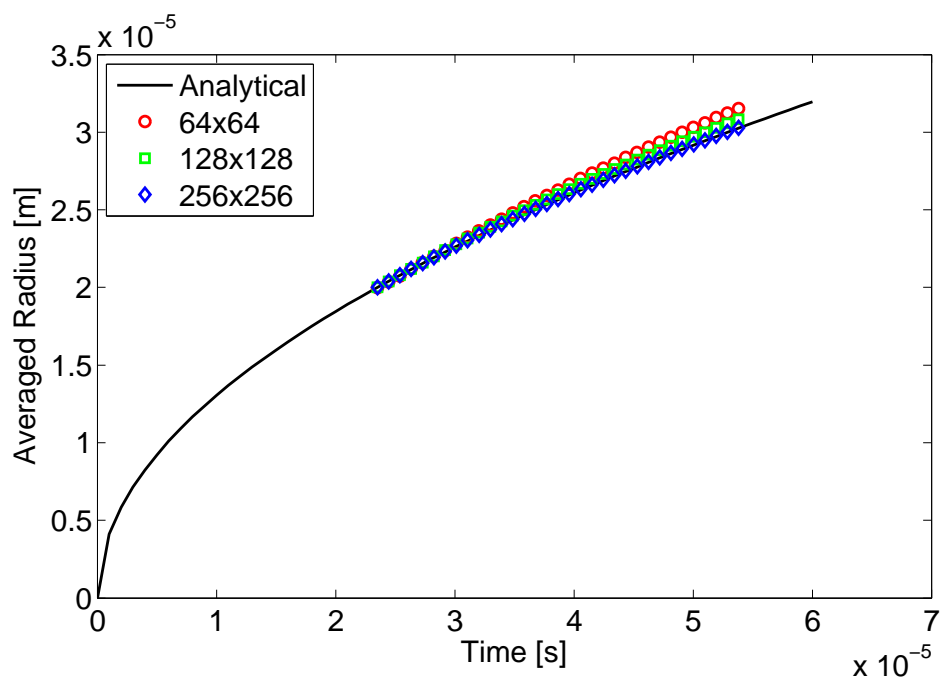


Figure 33: *Case 5.* (Top) Time evolution of bubble radius and (Bottom) profile of bubble interface at $t = 53.83\mu\text{s}$ for evaporating 2-D bubble in superheated liquid ($\Delta T = 2\text{K}$). The working fluid is saturated water at $P = 101.3\text{kPa}$. Three grid resolutions (64, 128, 256) are plotted on top of analytical solution (solid line).

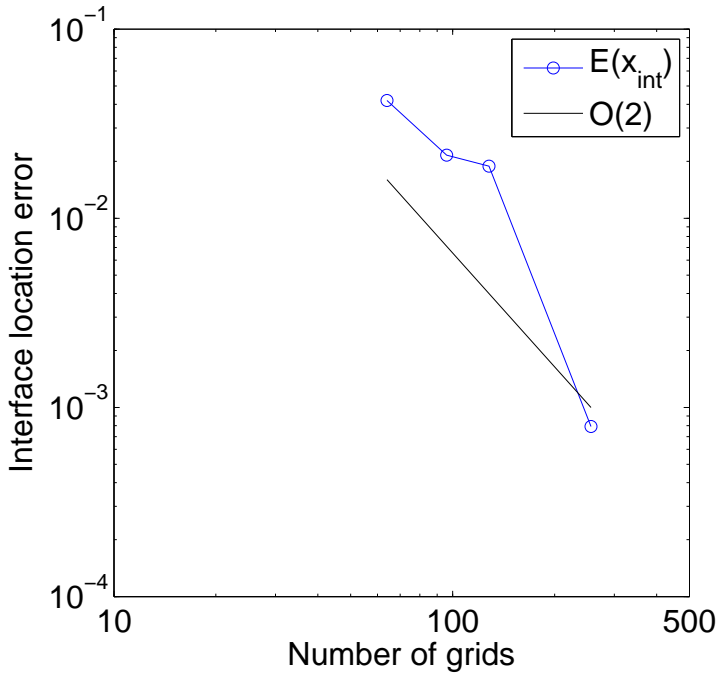


Figure 34: *Case 5.* Order of convergence with respect to interface location for evaporating 2-D bubble in superheated liquid ($\Delta T = 2K$). The working fluid is saturated water at $P = 101.3kPa$. Errors are computed for three grid resolutions (64, 128, 256).

field. Owing to the asymmetric diffusion of the interface, the jump occurs in the unconfined phase (liquid) and the fluid velocity expanded continuously over the thin diffused interface region. The interface velocity is smoothly distributed near the diffused interface region.

Fig. 36 (a) and Fig. 36 (b) show the temperature and pressure contours for the medium grid size at $t = 53.83\mu s$ respectively. Again it can be found that the pressure jump is resolved sharp without oscillatory behavior at the interface.

4.6 Conclusion

Numerical method for multiphase, phase change simulations has been developed to improves on issues such as the numerical oscillation of pressure and the spurious interface velocity field by incorporating suitable features of the sharp interface method and the diffused interface. The new method features, (i) continuous velocity and density fields within a thin interfacial

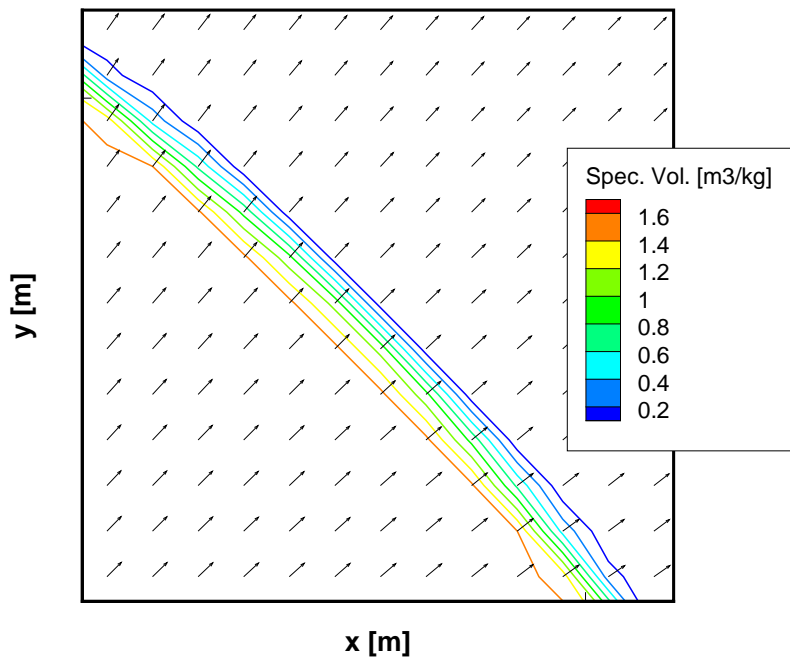
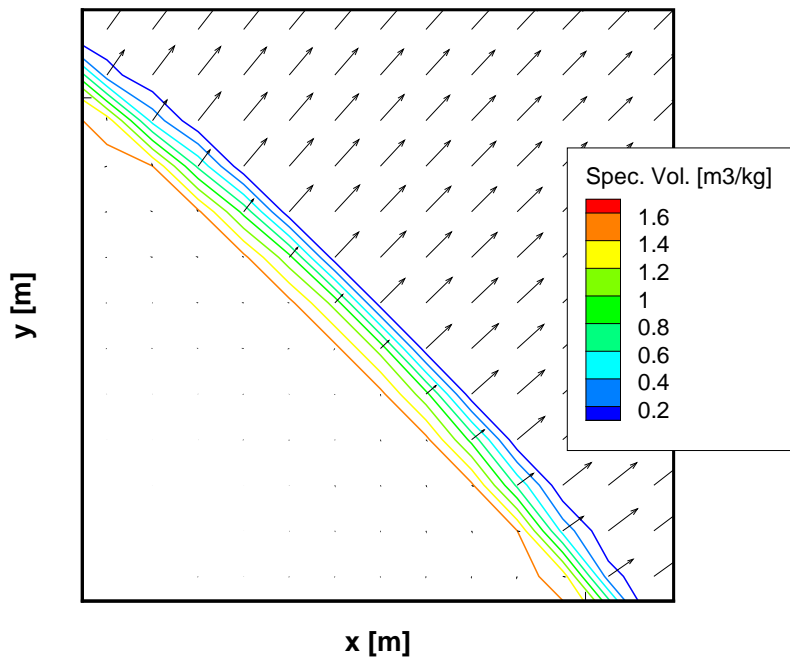


Figure 35: Case 5. (Top) Fluid velocity and (Bottom) interface velocity field around the diffused interface at $t = 53.83\mu\text{s}$ for grid resolution 256×256 .

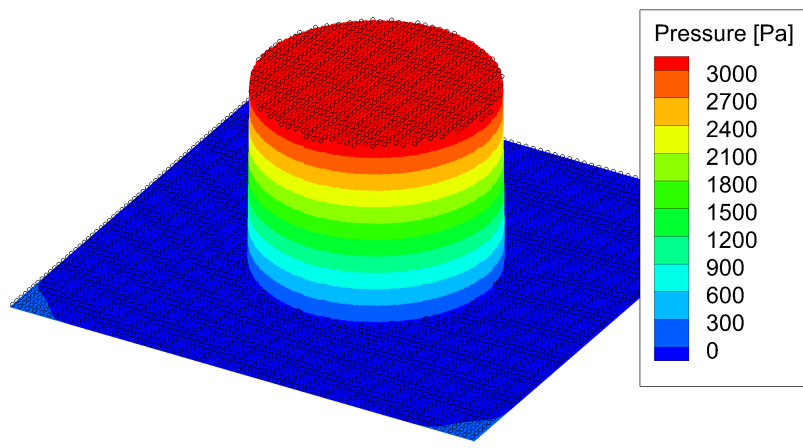
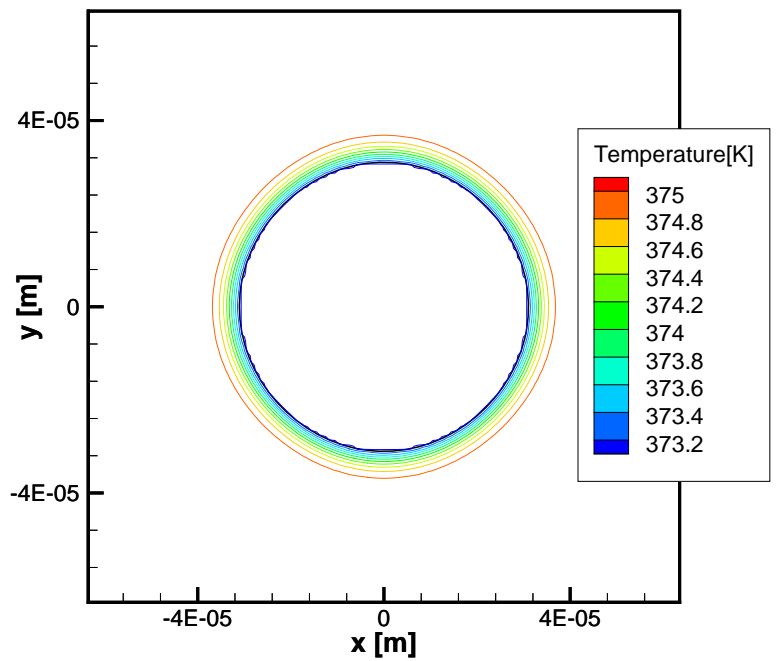


Figure 36: *Case 5.* (Top) Temperature and (Bottom) pressure fields at $t = 53.83\mu s$ for grid resolution 256×256 .

region, (ii) temporal velocity correction steps to ensure robust pressure solution and (iii) mass flux projection correction for improved mass flux conservation. Simulations of one-dimensional and two-dimensional test cases have been carried out to show that the new method can promote robust solutions in the pressure field and the interface velocity field which ensures physical accuracy in the advection of the interface due to phase change. The new method has shown enhanced results compared to the sharp ghost fluid method as well as previous diffused interface method. Also the method works well in combination with the sharp pressure jump conditions. Numerical results show very good agreement with analytical solution with overall 2nd order convergence in space.

5 Validation Cases: Film Boiling

The film boiling regime is ideal for validation cases because its analysis are less complex and the predictive correlations are reliable compared to the nucleate boiling regime due to the heated surface condition being less influential on the heat transfer mechanism. Thus, the in-house code is validated with a series of 2-D and axisymmetric film boiling cases using water and R134a as working fluids. The results are compared qualitatively with the numerical and experimental observation from literature in term of the bubble shape and release mechanism as well as quantitatively with the Nusselt number correlations. The conditions for film boiling cases are summarized in Table. 4.

Table 4: *Conditions for film boiling cases.*

	System	Working fluid	ΔT
Case 6.1.	2-D	saturated water ($P_r = 0.99$)	5K
Case 6.2.	2-D	saturated water ($P_r = 0.99$)	5K
Case 6.3.	2-D	saturated water ($p = 101.3\text{kPa}$)	300K
Case 7.1.	axisymmetric	saturated R134a ($P_r = 0.92$)	30K
Case 7.2.	axisymmetric	saturated R134a ($P_r = 0.92$)	30K
Case 7.3.	axisymmetric	saturated PF-5060 ($p = 101.3\text{kPa}$)	$\Delta T_{sup} = 100\text{K}$, $\Delta T_{sub} = 10\text{K}$

5.1 Cases 6.1-6.3. Two-Dimensional Cases

The film boiling problem illustrated in Fig. 37 is@articleID, author = author, title = title, journaltitle = journaltitle, date = date, OPTtranslator = translator, OPTannotator = annotator, OPTcommentator = commentator, OPTsubtitle = subtitle, OPTtitleaddon = titleaddon, OPTeditor = editor, OPTeditora = editora, OPTeditorb = editorb, OPTeditorc = editorc, OPTjournalsubtitle = journalsubtitle, OPTissuetitle = issuetitle, OPTissuesubti-

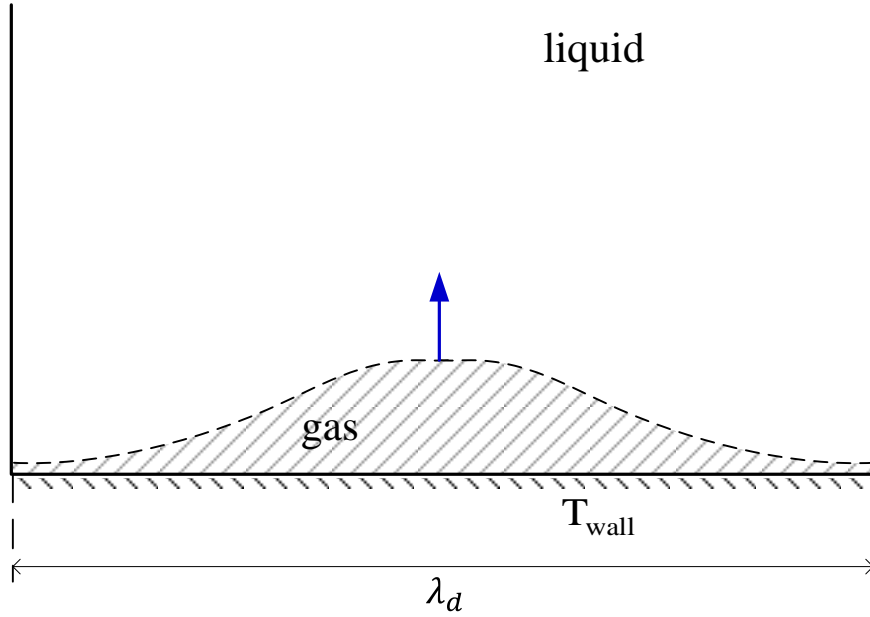


Figure 37: Illustration of 2-D film boiling problem.

tle = issuesubtitle, OPTlanguage = language, OPToriglanguage = origlanguage, OPTseries = series, OPTvolume = volume, OPTnumber = number, OPTeid = eid, OPTissue = issue, OPTmonth = month, OPTpages = pages, OPTversion = version, OPTnote = note, OPTissn = issn, OPTaddendum = addendum, OPTpubstate = pubstate, OPTdoi = doi, OPTeprint = eprint, OPTeprintclass = eprintclass, OPTeprinttype = eprinttype, OPTurl = url, OPTurldate = urldate, setup with a thin layer of gas phase below the liquid and above a heated solid surface. The gas film is initially defined by a function of half cosine wave

$$\phi(x, y) = y - (4 + \cos(2\pi x/\lambda_d)) \lambda_d/128 , \quad (87)$$

where λ_d is the most unstable Taylor wavelength

$$\lambda_d = 2\pi\sqrt{3\sigma/g(\rho_l - \rho_g)} , \quad (88)$$

Table 5: R134a properties at Near critical pressure $p_r = 0.92$

Phase	ρ [kg/m ³]	μ [μ Pa· s]	C_p [J/kgK]	k [W/mK]	h_{lg} [kJ/kg]	σ [N/m]	T_{sat} [K]
Vapor	301.9	21.71	4445	0.0415			
Liquid	730.8	56.72	5128	0.052	54.6	0.000182	370.46

or in dimensionless parameters

$$\lambda'_d = \frac{\lambda}{L} = 2\pi \sqrt{\frac{3Fr^2}{We(1 - \rho')}} , \quad (89)$$

and λ is the reference length scale defined as

$$\lambda = \sqrt{\sigma g(\rho_l - \rho_g)} . \quad (90)$$

The initial profile promotes the onset of Rayleigh-Taylor instability during film growth and bubble formation at the crest of the wavy interface. The thin gas film is maintained by the balance between the periodically detaching bubbles and the gas formation due to phase change. To validate current method, two systems that have been studied previously [8, 9, 55, 56] are used; water at near critical pressure (Table 3) and R134a at near critical pressure (Table 5). The computational domain is taken as $\lambda_d \times \lambda_d$ for grid independence study and Nusselt number validation cases while $\lambda_d \times 2\lambda_d$ is used for the investigation of bubble formation and release mechanisms as well as temperature, pressure and velocity fields. At the bottom wall, a constant temperature is defined as

$$T_{wall} = T_{sat} + \Delta T , \quad (91)$$

where $\Delta T = 5\text{K}$ for water and $\Delta T = 30\text{K}$ for R134a. The liquid is assumed to be at the saturation temperature while the interface temperature depends on the curvature and the

pressure by

$$T_\Gamma = T_{sat} + \frac{T_{sat}(P_\Gamma - P_\infty)}{h_{gl}} \left(\frac{1}{\rho_g} - \frac{1}{\rho_l} \right) - \frac{\sigma T_{sat} \kappa}{2h_{gl}} \left(\frac{1}{\rho_g} + \frac{1}{\rho_l} \right), \quad (92)$$

The lateral boundaries are symmetric and an outflow boundary condition is used at the top. A buffer layer has also been defined at the top boundary. Moreover, to avoid numerical issues at the outlet for two-phase flow, the bubble is removed before it contacts the outflow boundary by adding a source term in the level set advection Eq. 16 as

$$\frac{\partial \phi}{\partial t} + \mathbf{u}_\Gamma \cdot \nabla \phi = S_b. \quad (93)$$

The source, S_b is given by

$$S_b|_{i,j} = C_b(j - (N_y - N_b))/N_b, \quad (N_y - N_b \leq j \leq nx) \quad (94)$$

where N_y is the mesh size in y -direction, N_b is the number of cells in the buffer layer in y -direction and C_b is the rates of removal defined proportional to the domain length.

The grid independence study results are shown in Fig. 38 for the water case with three mesh sizes, 64×64 , 128×128 and 256×256 . The figure shows the interface profile before the bubble breaks off at $t = 0.093$ s. It is found that the two higher resolution cases match closely. In case of the coarse grid, the interface fail to sustain the thin layer at the bottom and crosses the bottom surface. This happens due to insufficient grid resolution near the thin gas layer and does not occur for the higher resolution cases. In this case, a limitation is enforced for the level set function to prevent it from collapsing and ensure interface existence because, in the scope of the level set method, the liquid-gas interface must be present in a cell in order for the phase transition to begin. The limit for the level set function at bottom

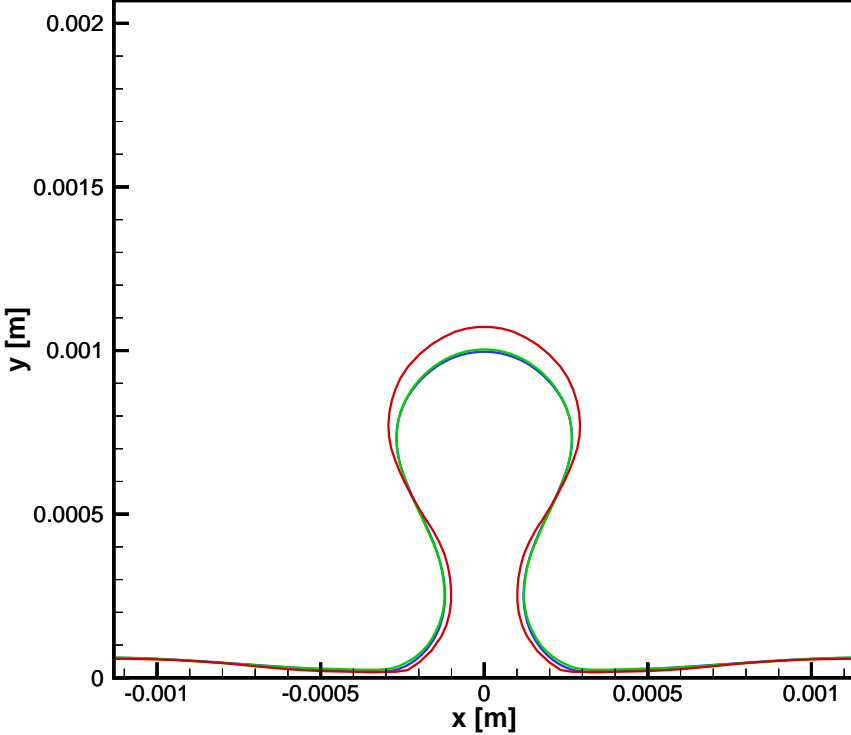


Figure 38: Case 6.1. Grid independence study for 2-D film boiling of water at $P_r = 0.99$ with $\Delta T = 5K$. Interface locations for three grid resolutions, 64×64 (red), 128×128 (green) and 256×256 (blue), are shown at $t = 0.322s$.

cell is to be always smaller than zero (for gas phase);

$$\phi(i, 1) = \min(-0.01\Delta x, \phi(i, 1)) . \quad (95)$$

While, this is a rather explicit implementation and can lead to small increase in the bubble size formation as shown in Fig. 38, the converged solutions do not reflect this error and dry out can be avoided at all times. The medium grid resolution is used for hereupon results.

In Fig. 39 and 40, the temperature contour, the pressure contour and the velocity field are plotted along with the interface profile at $t = 0.338$ for water and $t = 0.15$ for R134a, just before the first pinch-off of a bubble. The temperature is scaled as $T' = (T - T_{sat})/(T_{wall} - T_{sat})$ and the pressure is the gauge pressure with respect to the saturation pressure. The pressure jump due to the surface tension effect is sharp at the interface without oscillatory

behavior. In Fig. 41, the maximum pressure over the computational time is plotted. As it has been shown in the verification cases, the overall time evolution of pressure is free of sharp peaks and oscillations. The small peaks that are found at $t = 0.34$ and $t = 0.354$ correspond to the pressure at the pinch-off and the collapse of the gas film close to the wall. Figs. 42 and 43 show the bubble formation and pinch-off process of a bubble for the water and R134a cases. After the pinch-off at the center node, the retractive motion of the film stem due to capillary force is transferred laterally and the film rises at the symmetric boundary (antinode). The pinch off point subsequently reverts back to the center node.

In addition to the near critical pressure conditions, the performance of the new method with a large density difference is also demonstrated with the saturated water properties at atmospheric pressure given in Table 2 and $\Delta T = 300\text{K}$ in two-dimensional coordinate domain of $\lambda_d \times \lambda_d$. Due to the large surface tension, fine meshes are required at the bottom and the grid resolution taken to be 100×400 . Fig. 44 shows the temperature contour, pressure contour and velocity field. In Fig. 45 the time evolution of the film boiling is shown. Like in the previous cases, smooth solutions of the interface advection and the transport variables as well as the sharp pressure jump without oscillatory behavior can be found.

5.2 Cases 7.1-7.3. Axisymmetric Cases

Although two-dimensional domains have been commonly used for studying film boiling, it is clear that a 2-D depiction cannot provide a realistic picture of actual bubble formation for such problems. In addition to the fact that the two-dimensional bubble is not spherical, the bubble pinch-off in 2-D case cannot account for effect of radial curvature and can create grid dependent, elongated gas stems, making it difficult to obtain converged solutions. To further validate bubble shape, a cylindrical coordinates is implemented and modified to the two-cylinder computational domain introduced in [2] and illustrated in Fig. 46. Here, the

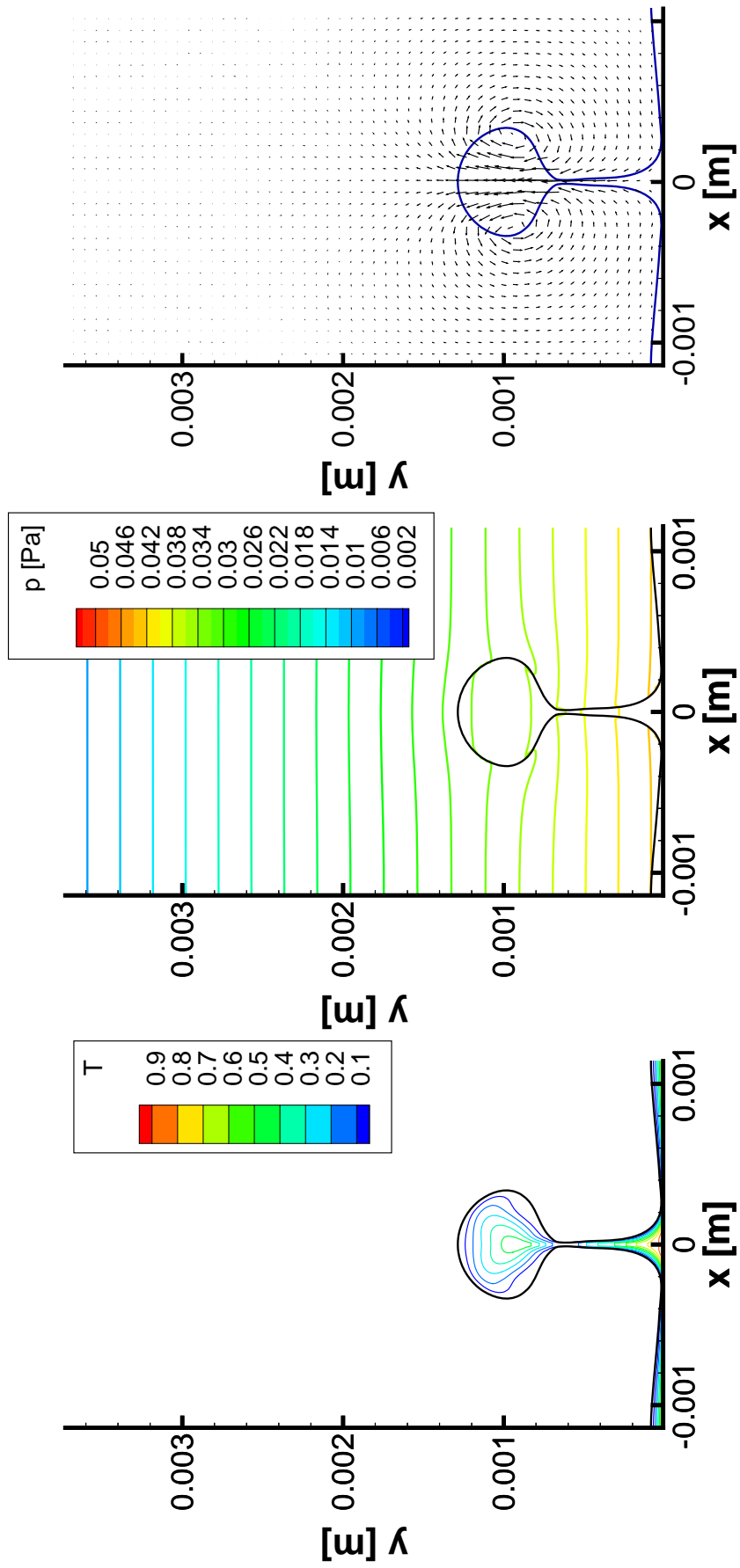


Figure 39: Case 6.1. 2-D film boiling of saturated water at $P_r = 0.99$ with $\Delta T = 5K$. Plots are temperature contour (left), pressure contour (center) and velocity field (right) at instance $t = 0.338s$. Results are shown for 128×256 grid resolution.

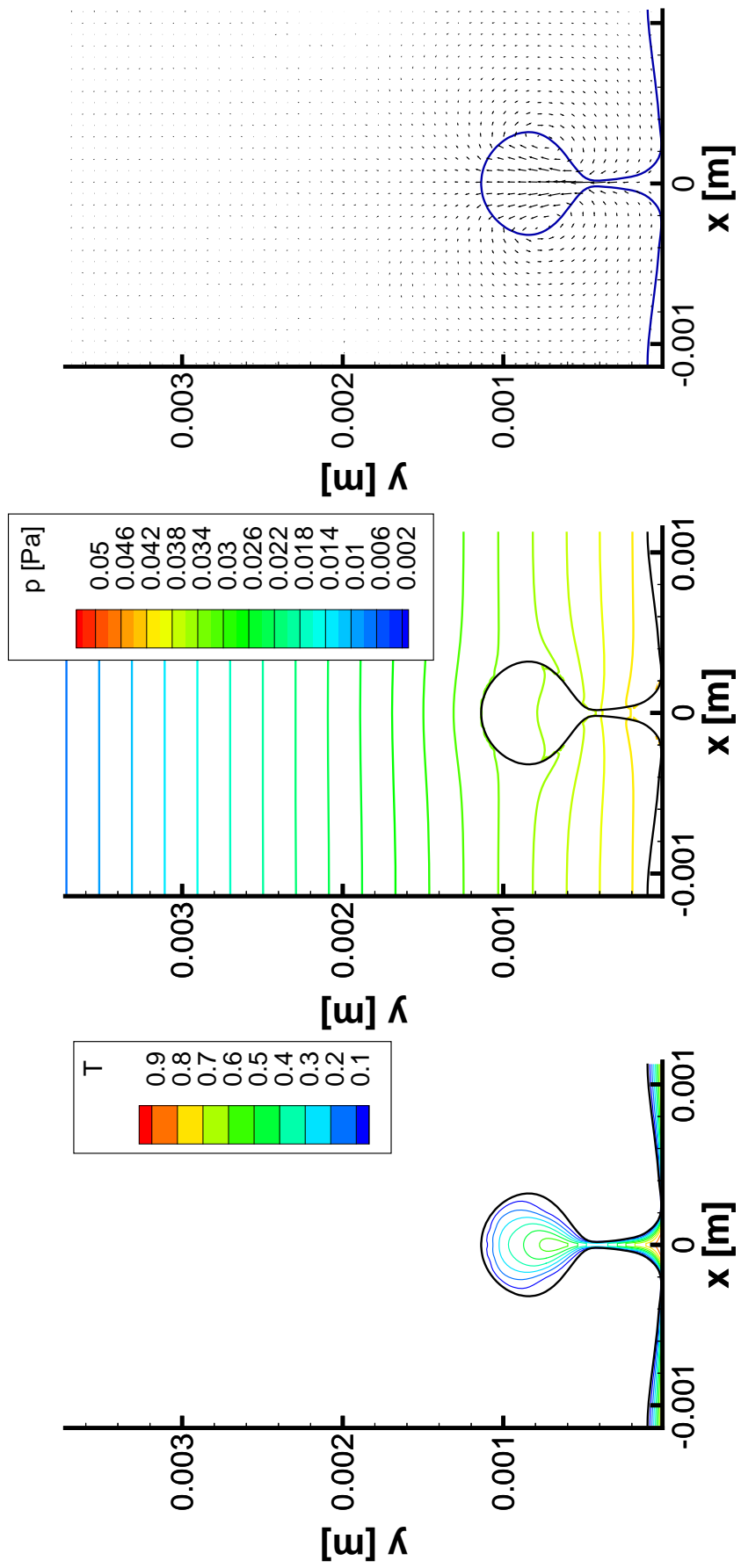


Figure 40: **Case 6.2.** 2-D film boiling of saturated R134a at $P_r = 0.92$ with $\Delta T = 30K$. Plots are temperature contour (left), pressure contour (center) and velocity field (right) at instance $t = 0.15s$. Results are shown for 128×256 grid resolution.

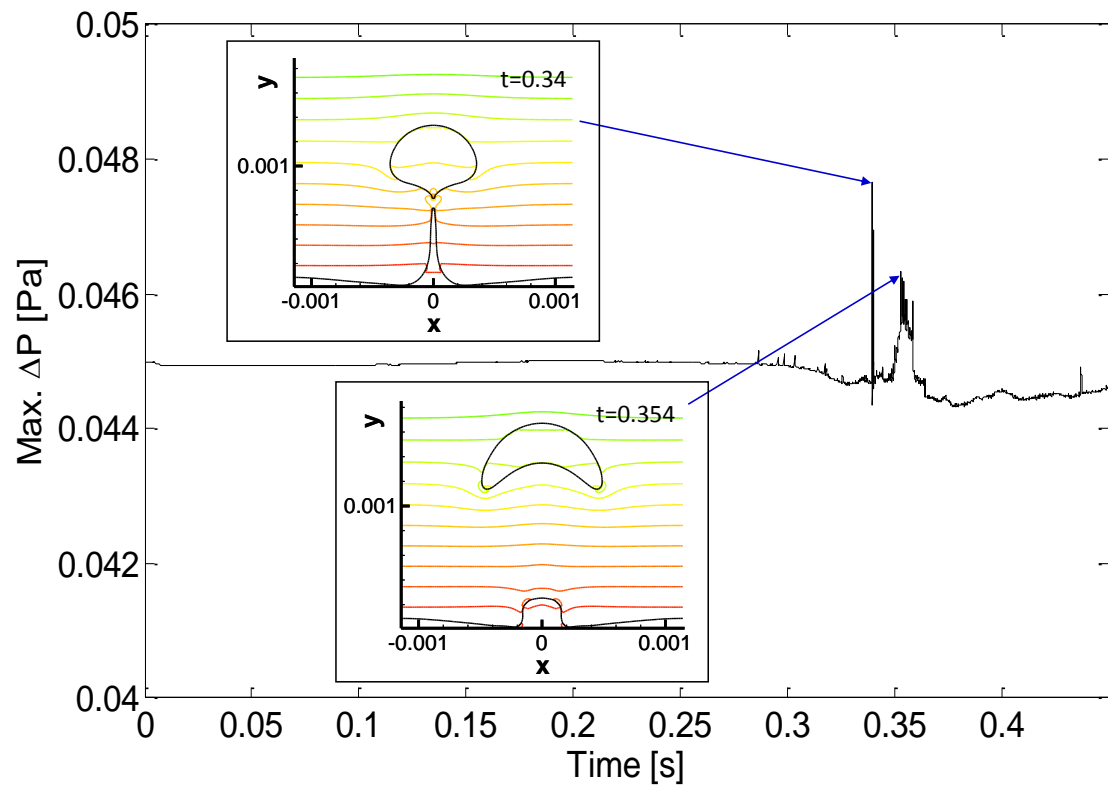


Figure 41: Case 6.1. Maximum pressure difference during computational time for 2-D film boiling of saturated water at $P_r = 0.99$.

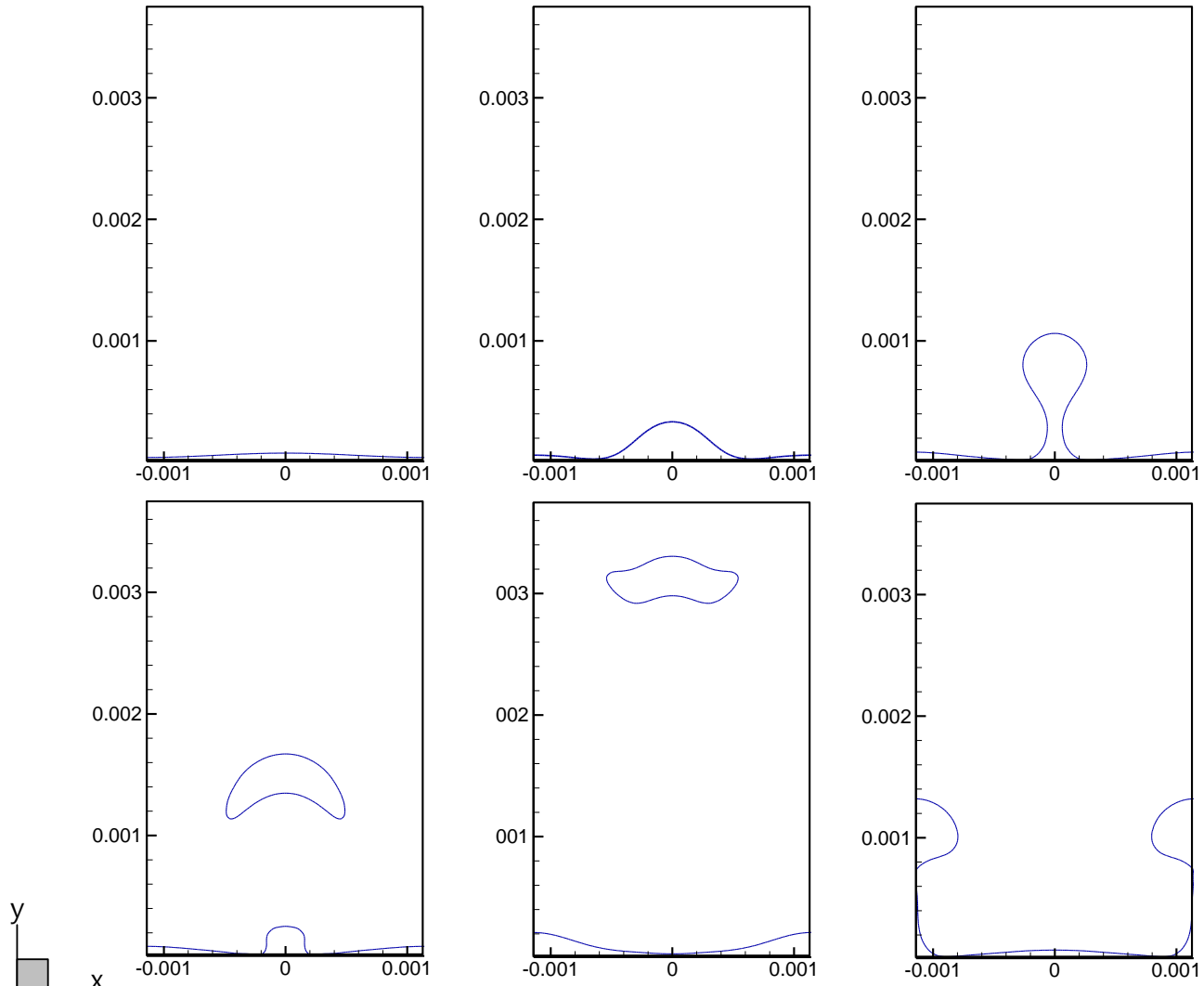


Figure 42: *Case 6.1. Bubble formation and pinch-off mechanism for 2-D film boiling of saturated water at $P_r = 0.99$ with $\Delta T = 5K$. Results are shown for 128×256 grid resolution.*

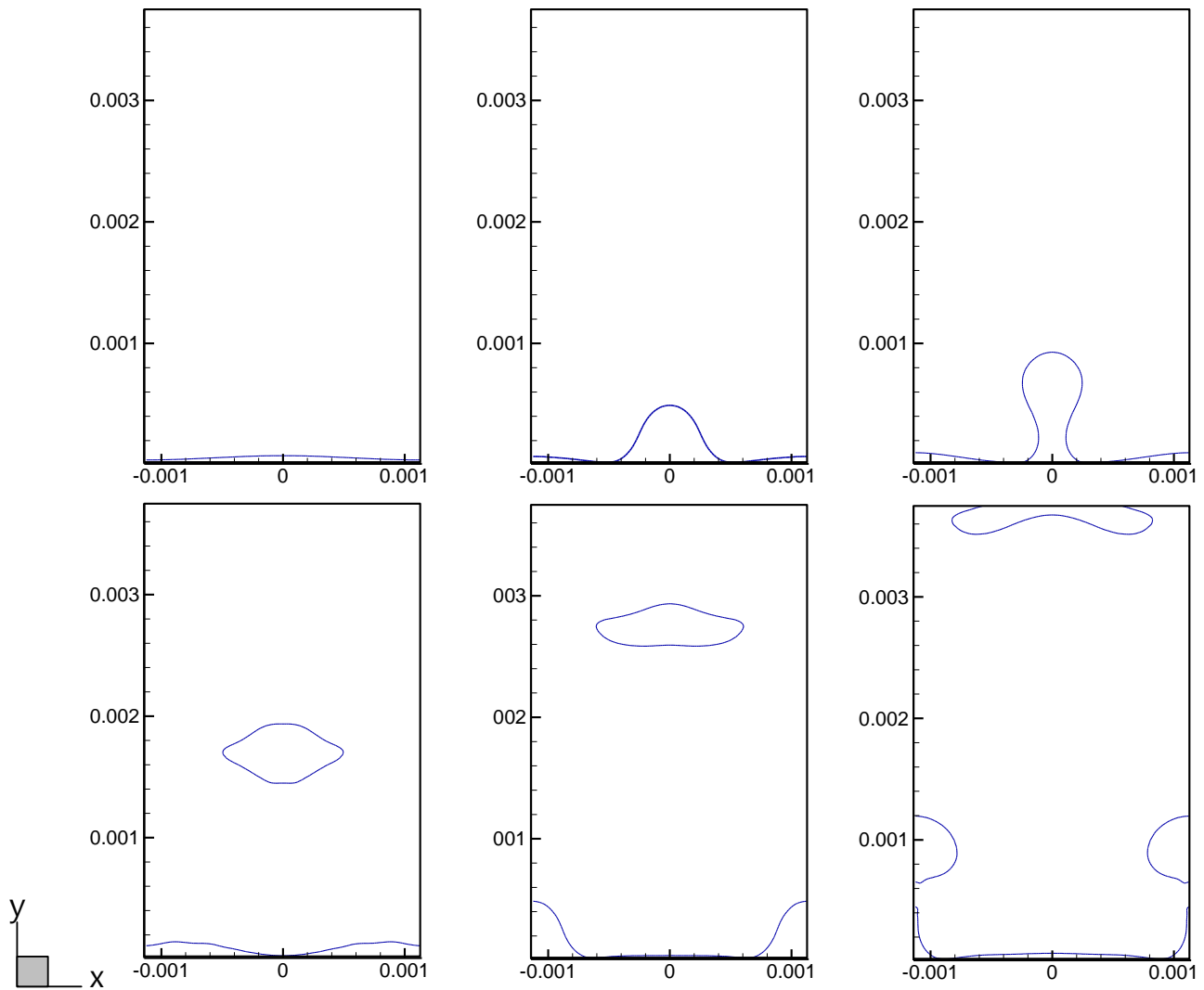


Figure 43: Case 6.2. Bubble formation and pinch-off mechanism for 2-D film boiling of saturated R134a at $P_r = 0.92$ with $\Delta T = 30K$. Results are shown for 128×256 grid resolution.

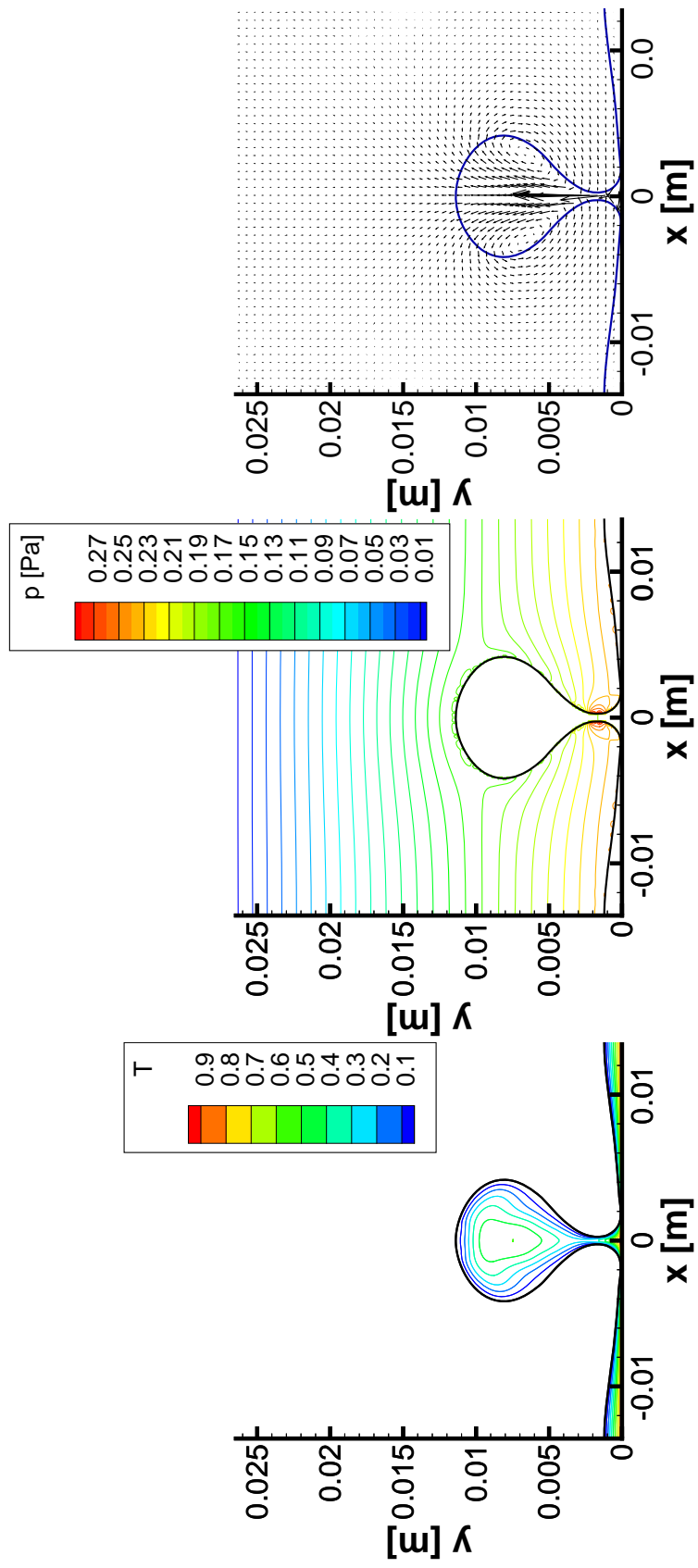


Figure 44: Case 6.3. 2-D film boiling of saturated water at atmospheric pressure condition with $\Delta T = 300K$. Plots are temperature contour (left), pressure contour (center) and velocity field (right) at instance $t = 0.15s$. Results are shown for 100×400 grid resolution.

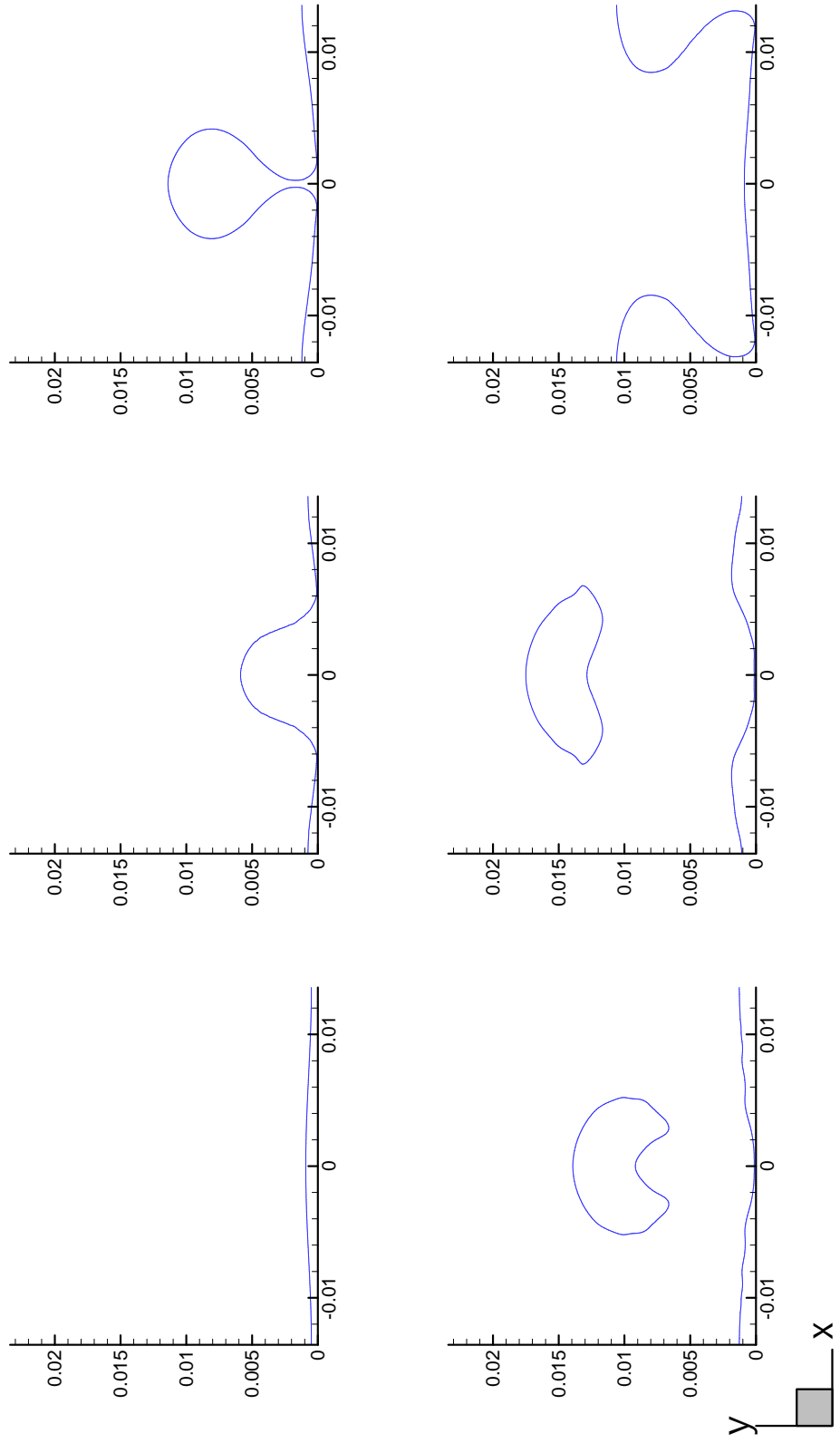


Figure 45: Case 6.3. Bubble formation and pinch-off mechanism for 2-D film boiling of saturated water at atmospheric pressure condition with $\Delta T = 300K$. Results are shown for 100×400 grid resolution.

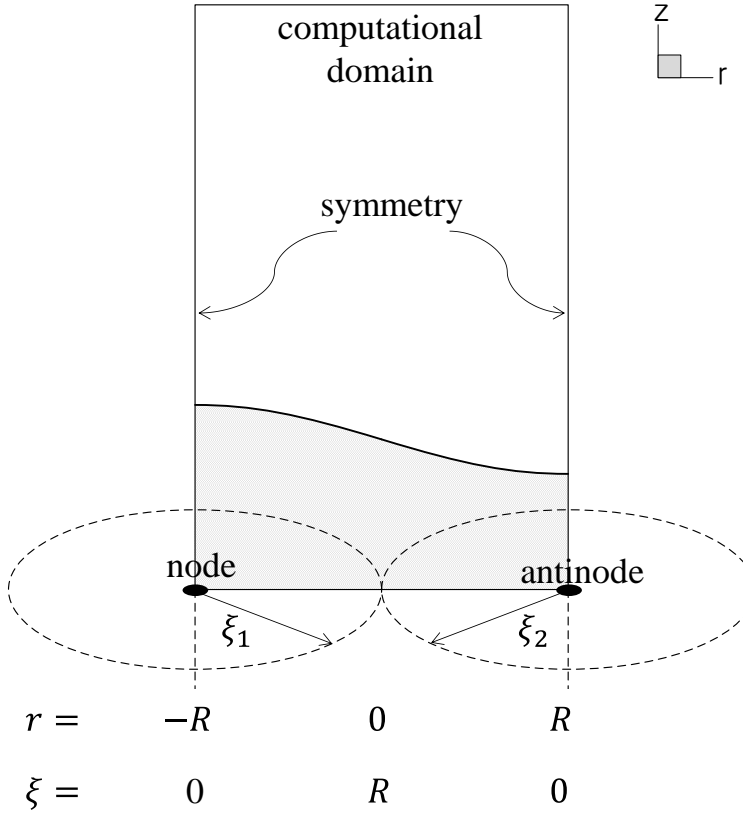


Figure 46: Illustration of the two-cylinder computational domain for axisymmetric film boiling cases.

domain width is $2R$ where R is defined

$$R = \lambda_d / \sqrt{2\pi} , \quad (96)$$

such that the boiling area is equivalent to that of a 3-D domain, λ_d^2 . The original axisymmetrical axis of the cylindrical coordinate (r, z) is replaced with (ξ, z) by $\xi = R - |r|$. The axisymmetric coordinate provides much closer approximation to 3-D results with the radial effects and spherical bubble and the two-cylindrical domain enables us to observe the node and antinode boiling phenomena. Water and R134a properties same as for 2-D cases are used. The dimension of the computational domain is $2R \times 4R$. Grid convergence is tested using three mesh sizes with a two times finer grid in the y -direction, 32×128 , 64×256 and

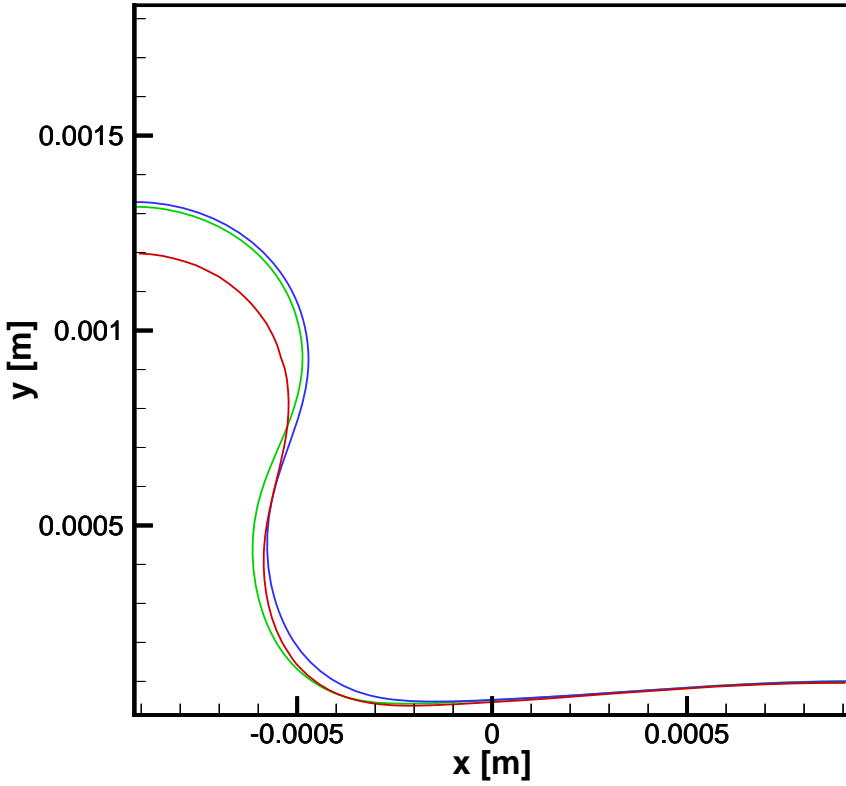


Figure 47: Case 7.1. Grid independence study for axisymmetric film boiling of saturated water at $P_r = 0.99$ with $\Delta T = 5K$. Interface locations for three grid resolutions, 64×64 (red), 128×128 (green) and 256×256 (blue), are shown at $t = 0.172s$.

128×512 , to resolve the thin film more efficiently. Fig. 48 shows the results and the two higher resolution profiles match each other closely. The following results are shown for the medium grid size.

The time evolution of the interface for the water and R134a conditions in the axisymmetric coordinates are shown in Fig. 48 and Fig. 49, respectively. The results show a clear difference in that the cylindrical coordinate produces a thicker and longer stem and higher bubble release points compared to the 2-D case. The observed interface formation for water case is found to be similar to the numerical result by Son et al. [8]. The contours for temperature and pressure and the velocity profiles are plotted in Fig. 50 at $t = 0.216s$ and in Fig. 51 at

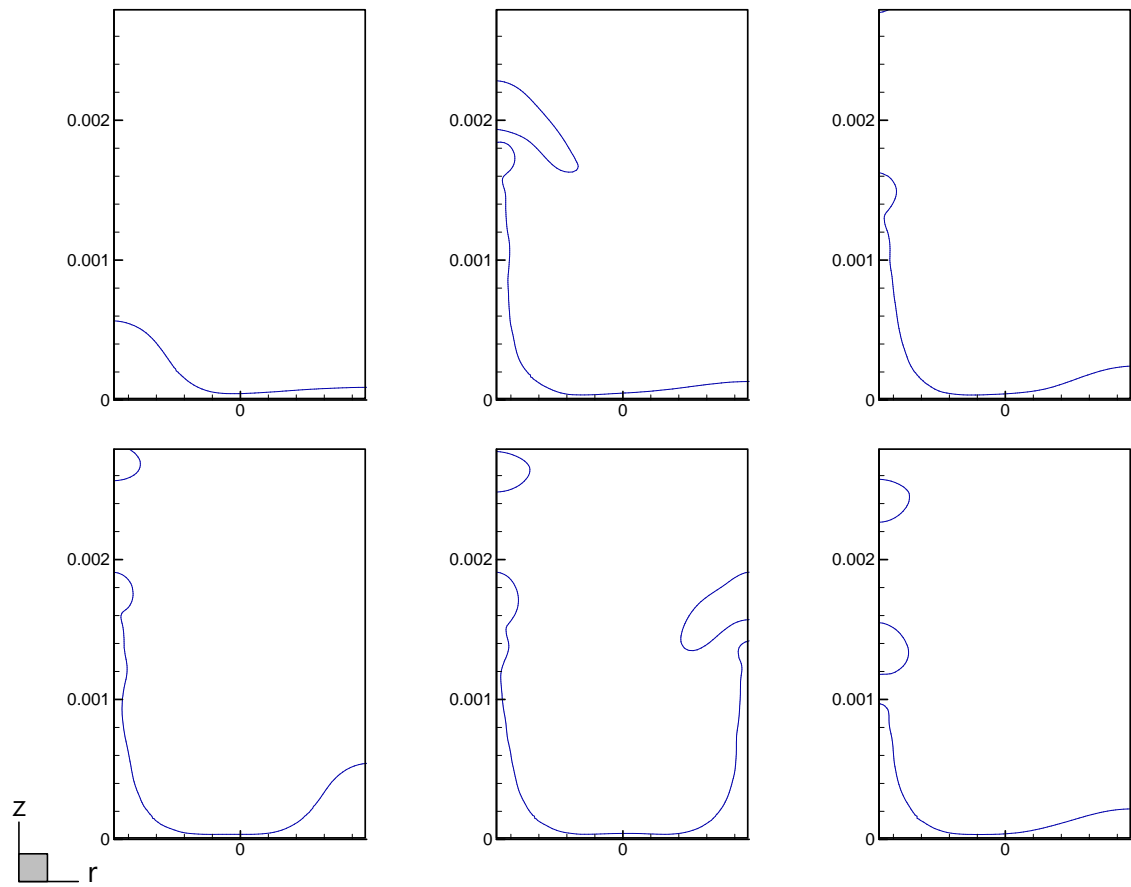


Figure 48: Case 7.1. Bubble formation and pinch-off mechanism for axisymmetric film boiling of saturated water at $P_r = 0.99$ with $\Delta T = 5K$. Results are shown for 128×256 grid resolution.

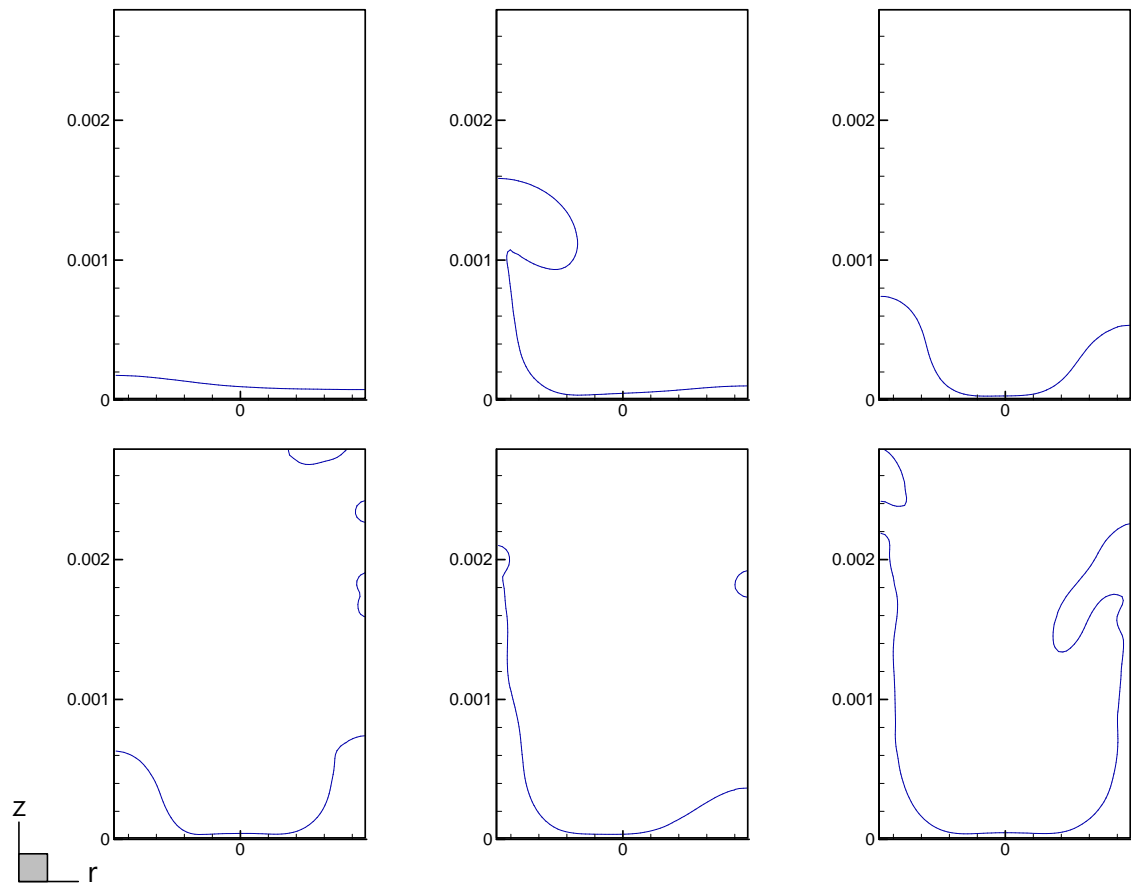


Figure 49: *Case 7.2. Bubble formation and pinch-off mechanism for axisymmetric film boiling of saturated R134a at $P_r = 0.92$ with $\Delta T = 30K$. Results are shown for 128×256 grid resolution.*

$t = 0.116\text{s}$ as with the 2-D cases. The thick gas phase stem is formed primarily due to radial fluid flow toward a center node but also is supported by the temperature profile inside the stem. Fig. 52 plots the mass flux due to phase change along the interface and it shows that a significant amount of phase change occurs at the gas stem. Higher wall temperatures lead to the vapor jet that increases the heat transfer coefficient. This is not accounted for in most mechanistic based correlations.

Numerical results for the Nusselt number at the bottom wall is compared with the existing correlations. The spaced averaged Nusselt number is calculated as a non-dimensional heat flux at the solid-gas interface according to

$$\overline{\text{Nu}} = \frac{1}{\lambda_d} \int_{-\lambda_d/2}^{\lambda_d/2} \frac{\lambda}{(T_{wall} - T_{sat})} \left. \frac{\partial T}{\partial y} \right|_{y=0} dx , \quad (97)$$

and for the axisymmetric coordinate as

$$\overline{\text{Nu}} = \frac{2}{R^2} \int_0^R \frac{\lambda}{(T_{wall} - T_{sat})} \left. \frac{\partial T}{\partial z} \right|_{z=0} r dr . \quad (98)$$

Correlations for plane film boiling are based on the bubble release rate as a function of buoyancy and film thickness. Here, the solutions are compared with two commonly used correlations developed by Berenson [66] and Klimenko [67] which are given by

$$\text{Nu}_B = 0.425 \left(\frac{\text{GrPr}}{\beta} \right)^{1/4} . \quad (99)$$

and

$$\text{Nu}_K = \begin{cases} 0.19 \times \text{Gr}^{1/3} \text{Pr}^{1/3} f_1 & \text{Gr} < 4.03 \times 10^5 \\ 0.216 \times \text{Gr}^{1/2} \text{Pr}^{1/3} f_2 & \text{Gr} > 4.03 \times 10^5 \end{cases} \quad (100)$$

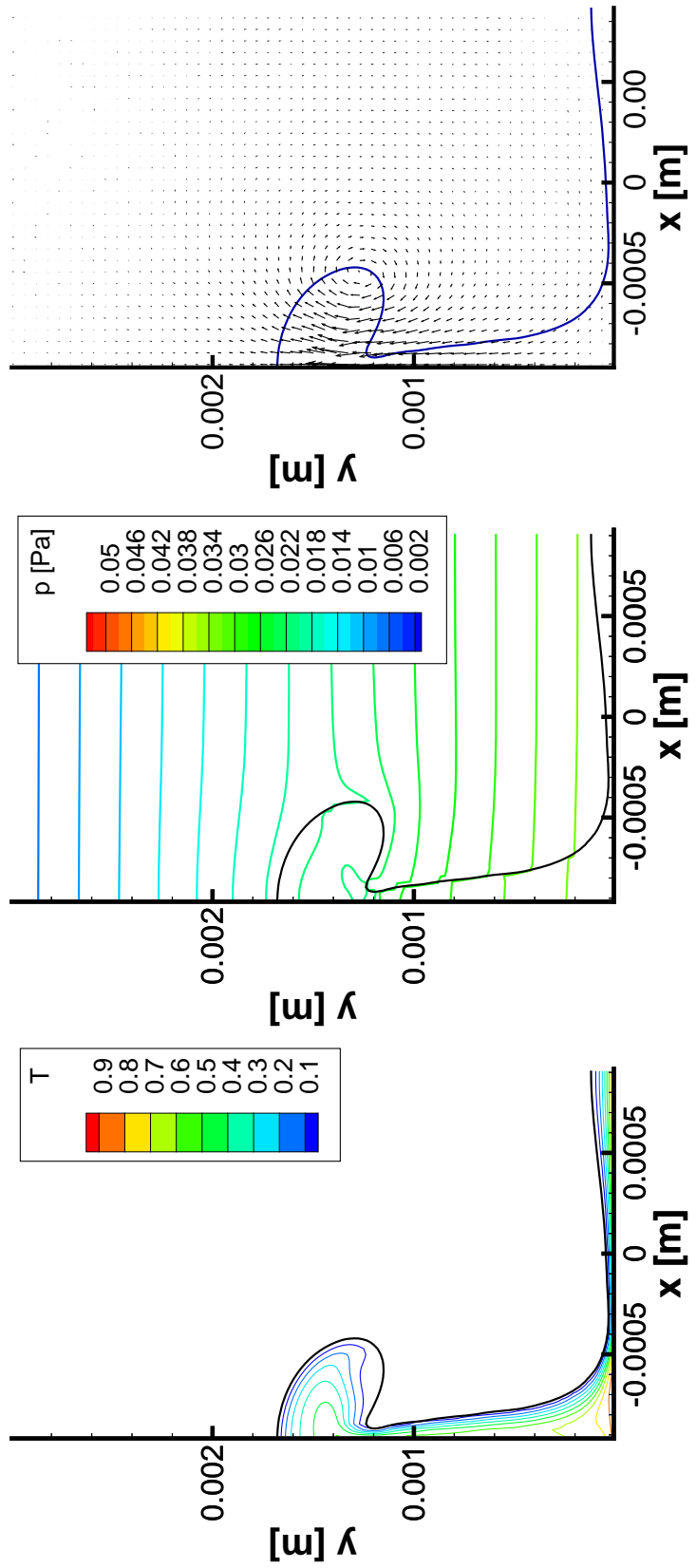


Figure 50: Case 7.1. Axisymmetric film boiling of saturated water at $P_r = 0.99$ with $\Delta T = 5K$. Plots are temperature contour (left), pressure contour (center) and velocity field (right) at instance $t = 0.216s$. Results are shown for 128×256 grid resolution.

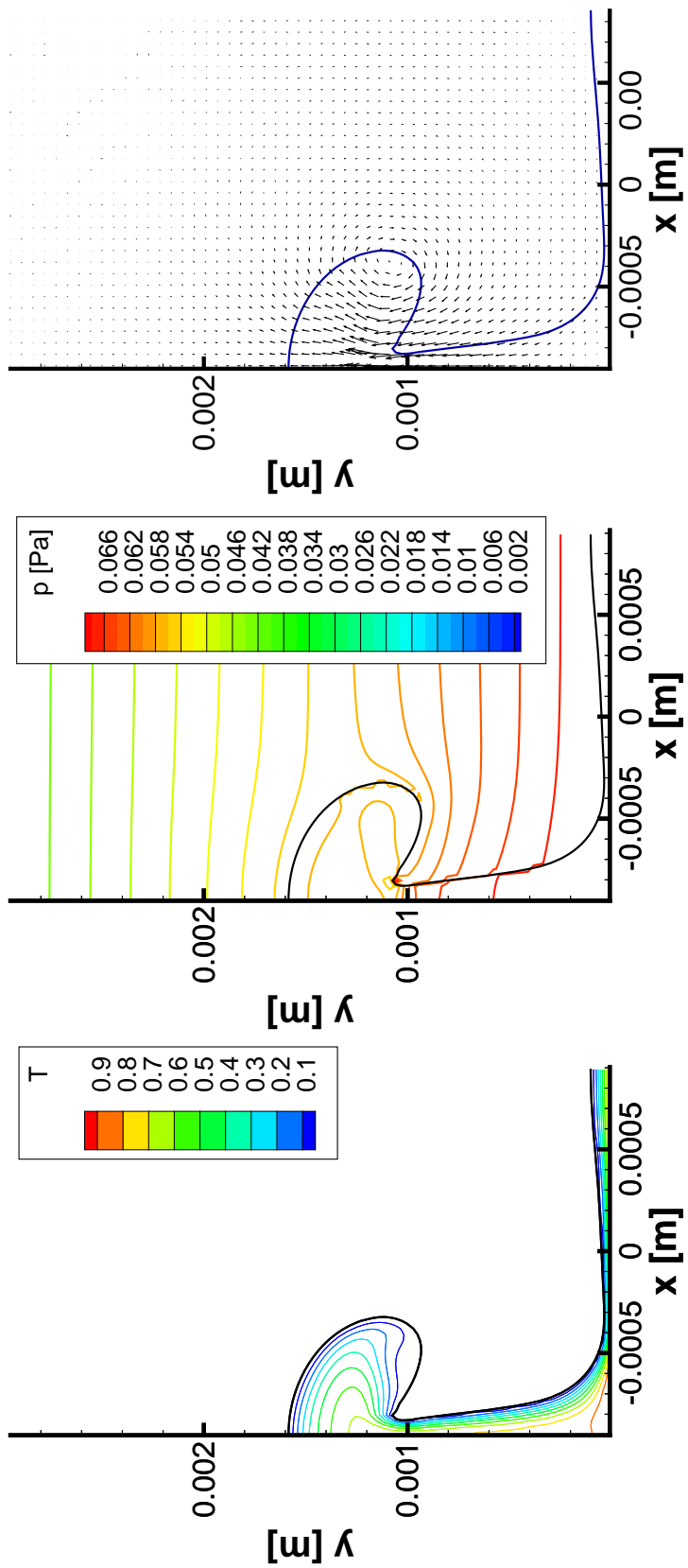


Figure 51: Case 7.2. Axisymmetric film boiling of saturated R134a at $P_r = 0.92$ with $\Delta T = 30K$. Plots are temperature contour (left), pressure contour (center) and velocity field (right) at instance $t = 0.116s$. Results are shown for 128×256 grid resolution.

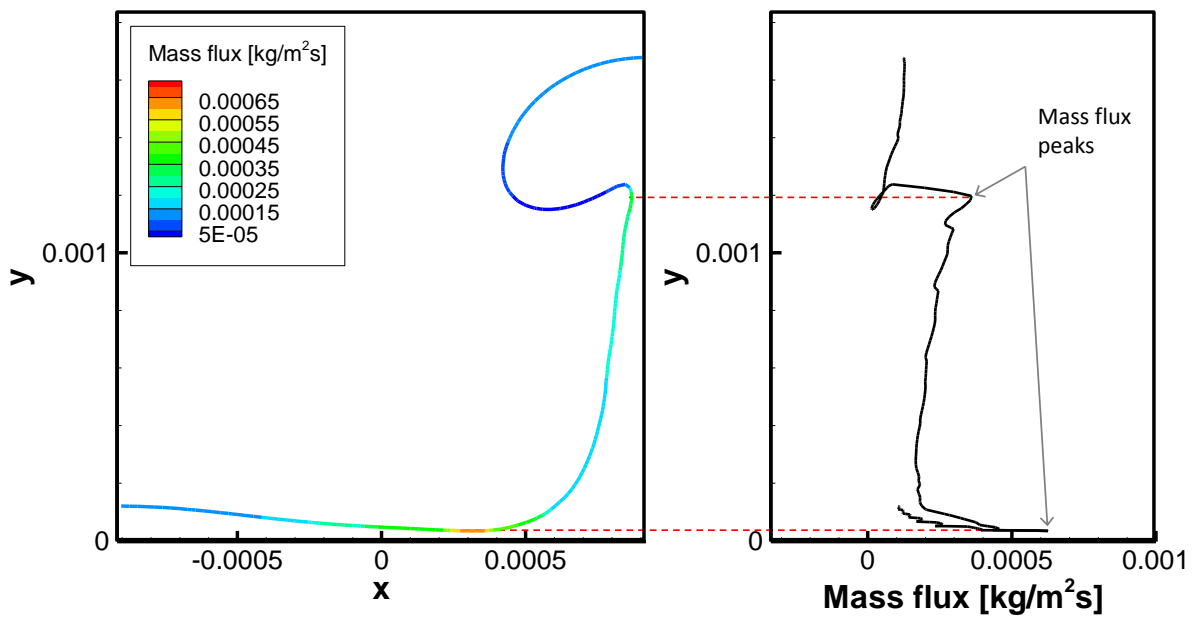


Figure 52: Case 7.1. Mass flux distribution along the interface profile for axisymmetric film boiling of saturated water at $P_r = 0.99$. Peaks are shown at the thinnest film region at the wall and the bubble pinch off point.

where B and K refer to Berenson and Klimenko respectively, and

$$f_1 = \begin{cases} 1 & \text{for } \beta > 0.71 \\ 0.89\beta^{-1/3} & \text{for } \beta < 0.71 \end{cases} \quad (101)$$

$$f_2 = \begin{cases} 1 & \text{for } \beta > 0.71 \\ 0.71\beta^{-1/3} & \text{for } \beta < 0.71 \end{cases} \quad (102)$$

where the dimensionless parameters are defined as

$$\begin{aligned} \text{Gr} &= \frac{\rho_g(\rho_l - \rho_g)g\lambda^3}{\mu_g^2} \\ \text{Pr} &= \frac{C_{p,g}\mu_g}{k_g} \\ \beta &= \frac{C_{p,g}(T_{wall} - T_{sat})}{h_{lg}} \\ f &= 1, \end{aligned} \quad (103)$$

respectively. The corresponding Nusselt numbers for current the cases are calculated as $\text{Nu}_B = 5.03$ and $\text{Nu}_K = 4.56$. The conditions used in the correlations are taken from the superheated gas properties at the averaged temperature $T_{ave} = T_{sat} + T_{wall}$.

Our results for the Nusselt number are shown for water in Fig. 53 and Fig. 54 and for R134a in Fig. 55 and Fig. 56 for both two-dimensional and axisymmetric cases. They show the periodicity of the Nusselt number variation over a few releases cycles. At the initial stages, the bubble sizes are mostly larger due to the initial setup of the interface and the release takes longer owing to the time required for the gas film to build up but soon it forms a quasi-steady periodic pattern. It can be seen that the Nusselt number fluctuates more for the two-dimensional case than the axisymmetrical case. Looking at the interface evolution, the thicker and higher crest of film is maintained at a certain height whereas the two-dimensional crest collapses further down after the bubble pinch-off, causing the larger fluctuation. Also

the time and space averaged Nusselt number are slightly larger in the axisymmetrical cases. This too appears to be a result of the concentration of the gas phase in the stem area creating a larger thin film region. However the two-dimensional and the two-circle axisymmetric case show little difference in terms of the time and space averaged Nusselt number. The Nusselt numbers for water cases are predicted slightly higher than the correlations while for R134a, it is lower. The reason for under or over prediction can be due to other wavelengths present in experiments which can leads to difference in the thin gas film area. Note that at the near critical pressure condition, the thermodynamic properties can vary by orders of magnitude over a small temperature difference. For the water case, the Nusselt numbers calculated based on the saturation temperature are $Nu_B = 4.39$ and $Nu_K = 7.92$. It can be found that our results fall between these values. It can also be anticipated that variable fluid properties can lead to a closer agreement with the correlations. Agarwal et al. [56] compared the influence of variable and constant thermal properties to find a closer match with the variable properties. Overall, comparing with the correlations, the numerical results are well in good agreement range with the both Klimenko and Berenson correlations.

The effect of mesh size on the Nusselt number is plotted for the two-cylinder axisymmetric film boiling case of water at a near critical pressure. In this case, the lower resolutions result in a slower rate of bubble growth and bubble release and an overestimation of the Nusselt number. This can explained by the under resolved temperature gradient at the interface which leads to a decrease in the evaporation rate.

Lastly, the experimental figures shown in [68, 69] are considered, to which they have compared their boundary fitted grid numerical solution, in order to validate the bubble shape of my simulation. The working fluid is PF-5060 at 101.325kPa and in this case, the liquid is subcooled by 10K and the wall superheat is 100K. To the best of the author's knowledge, the viscosity and the thermal conductivity of the gas phase are unavailable or has not been specified. Thus, I took the liberty of using the value for vapor at atmospheric pressure. The

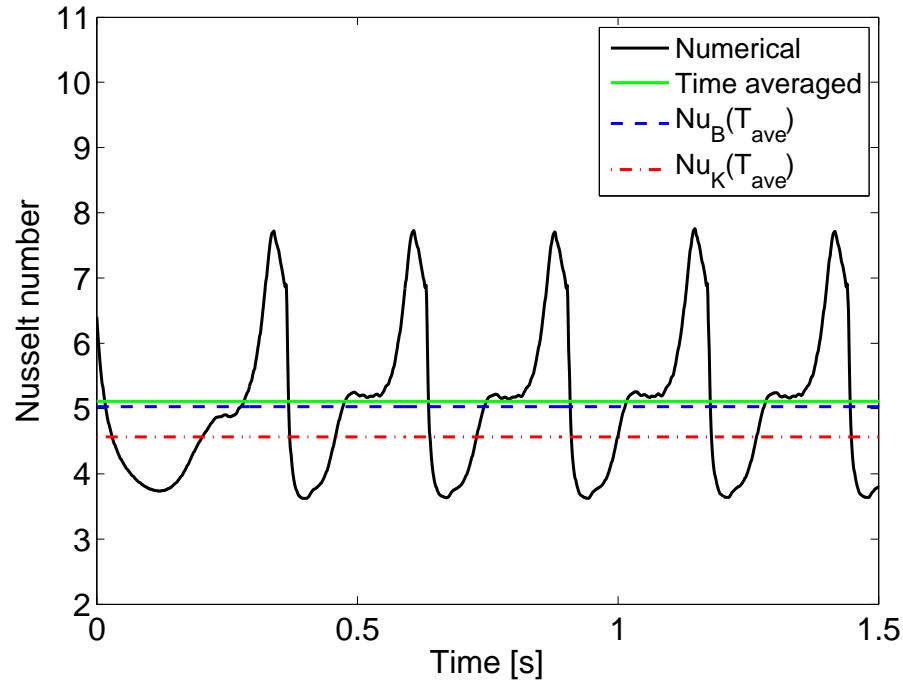


Figure 53: *Case 7.1.* Space averaged Nusselt number for 2-D saturated water film boiling at $P_r = 0.99$ with $\Delta T = 5K$. Numerical results and the correlations compared.

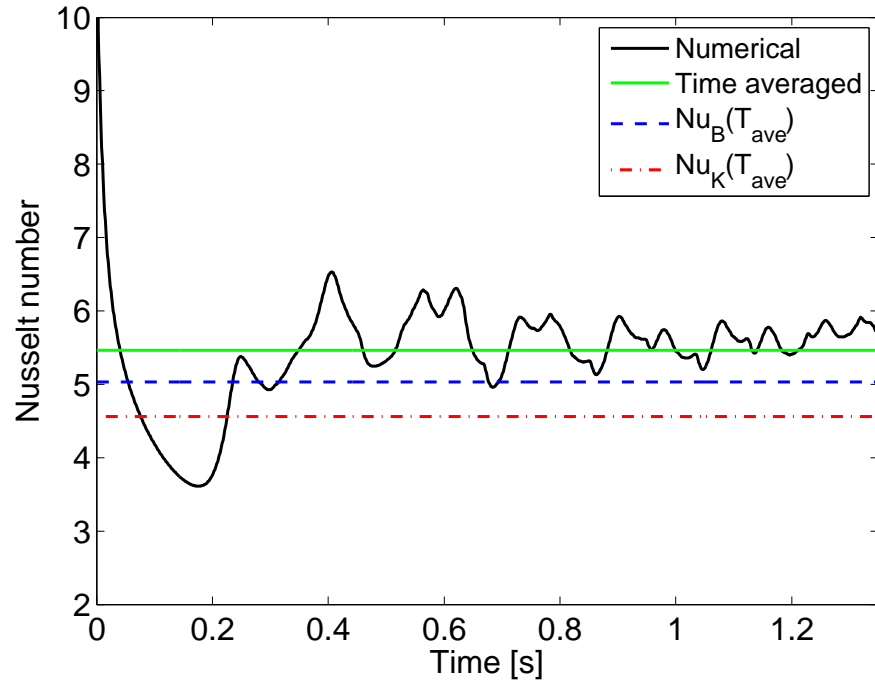


Figure 54: *Case 7.3.* Space averaged Nusselt number for axisymmetric saturated water film boiling at $P_r = 0.99$ with $\Delta T = 5K$. Numerical results and the correlations compared.

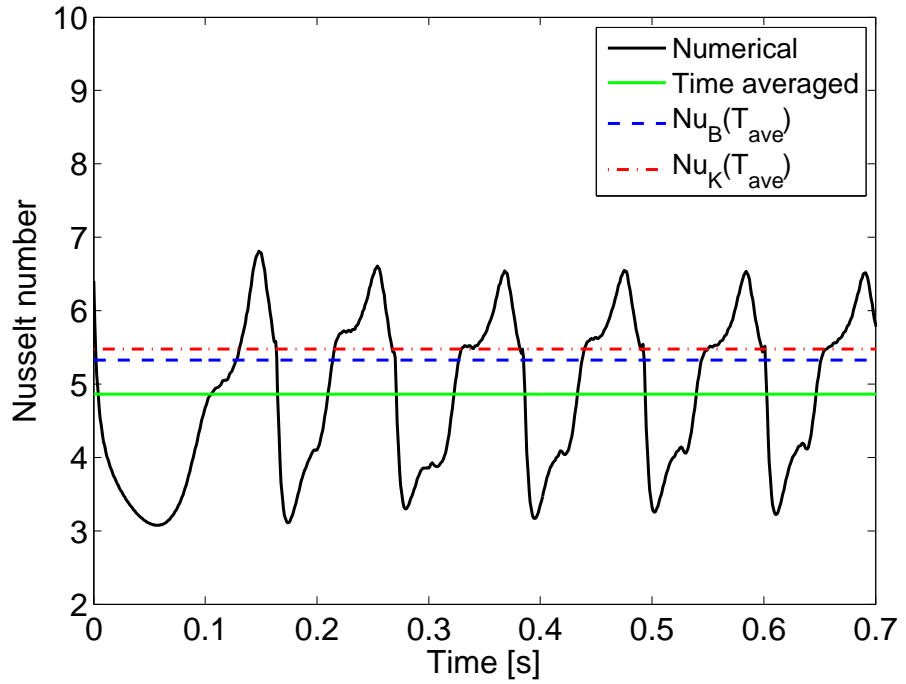


Figure 55: *Case 7.2.* Space averaged Nusselt number for 2-D R134a film boiling at $P_r = 0.92$ with $\Delta T = 30K$. Numerical results and the correlations compared.

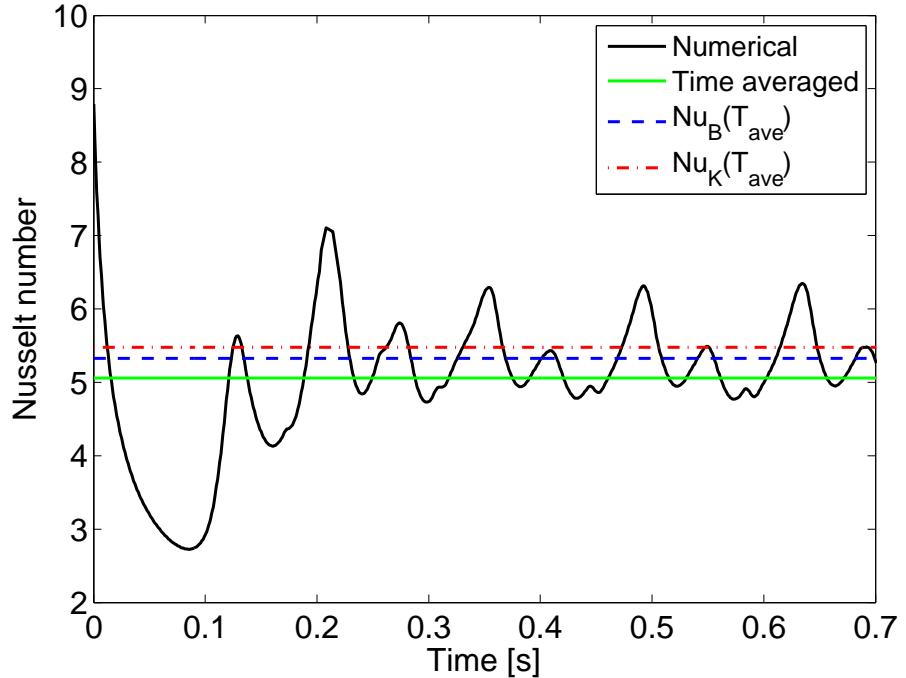


Figure 56: *Case 7.4.* Space averaged Nusselt number for axisymmetric R134a film boiling at $P_r = 0.92$ with $\Delta T = 30K$. Numerical results and the correlations compared.

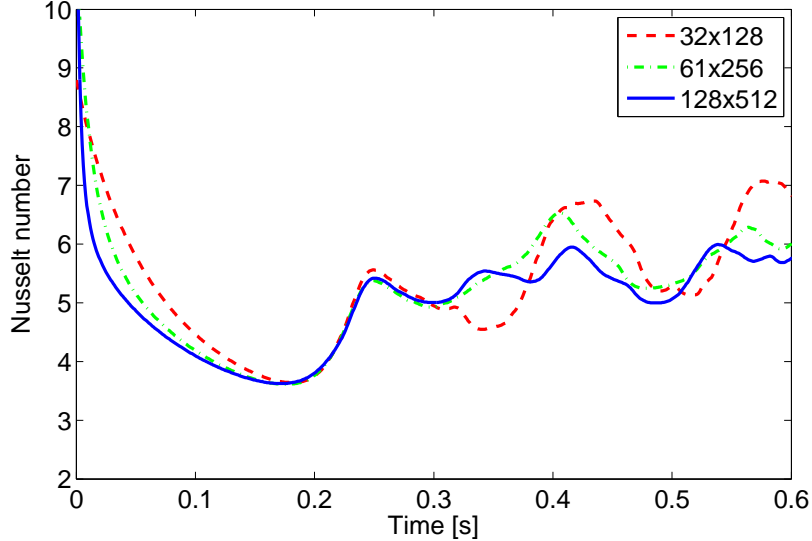


Figure 57: *Case 7.3.* Space averaged Nusselt number calculated with three grid resolutions for axisymmetric film boiling of saturated water at $P_r = 0.99$ with $\Delta T = 5\text{K}$.

Table 6: Saturated PF-5060 properties at $p = 101.3\text{kPa}$

Phase	ρ [kg/m ³]	μ [μ Pa· s]	C_p [J/kgK]	k [W/mK]	h_{lg} [kJ/kg]	σ [N/m]	T_{sat} [K]
Vapor	13.01	12.6	868	0.025			
Liquid	1620.94	447	1096	0.0538	88000	0.0106	329.15

properties used in the current simulations are shown in Table. 6 and a mesh size of 128×128 has been used over a $\lambda_d \times \lambda_d$ domain.

Our solutions are shown in Fig. 58 and good qualitative agreement can be observed of the bubble shape deformation.

5.3 Conclusions

A series of film boiling simulations were carried out to validate the new method. Saturated water, R134a and PF5060 at near critical and atmospheric pressure conditions were considered in 2-D and axisymmetric domains. Results show good quantitative and qualitative agreement with existing correlations for the Nusselt number and experimental observation of film boiling shapes. The comparison between two-dimensional and axisymmetric simula-

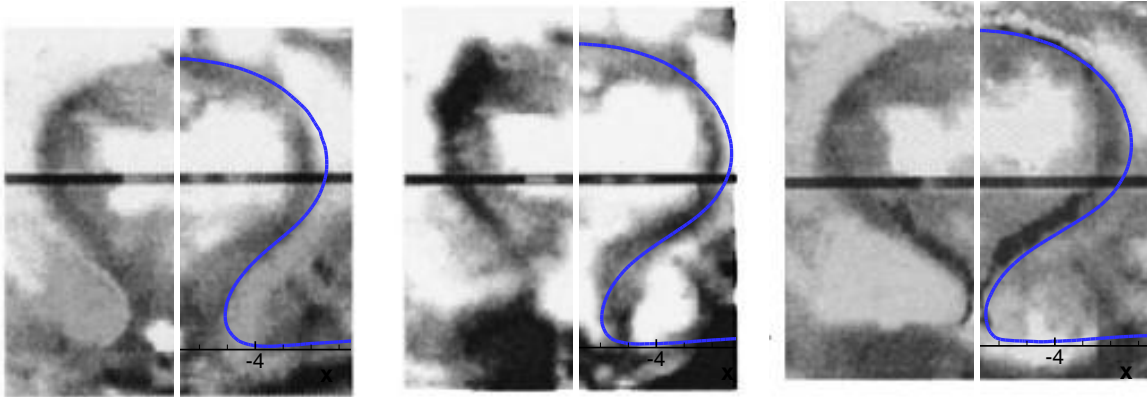


Figure 58: *Case 7.3.* Comparison of bubble shapes between experimental figures [69] and our results for film boiling of saturated PF-5060 at $p = 101.3\text{kPa}$ with $\Delta T = 100\text{K}$ and $\Delta T_{sub} = 10\text{K}$.

tions shows that the axisymmetric case results in higher and thicker film crests and produces smaller bubbles with higher release frequency. Comparison between numerical simulation and a photographic study [69] for the shape of bubble formation shows excellent similarity.

6 Numerical Study on Taylor Bubble Flow with Heat Transfer and Phase Change

6.1 Introduction

Multiphase flow in pipes or channels is characterized by specific patterns of the liquid-gas interface that depend on the fluid properties, the mass fraction of the liquid, the heat transfer rate and the flow rate. The regime of slug flow is often found at low vapor qualities where intermittent bodies of liquid and gas phase are formed. A Taylor bubble refers to elongated bubbles, separated by liquid slugs, that almost fills up the tube leaving a thin liquid film on the wall. The basic physical mechanisms related to Taylor bubble flow arise in many fields of engineering research. The study of the well characterized problem of Taylor bubbles thus enables the understanding of a broad range of the physical phenomenon in practical applications. For example, Horvath et al. [70] showed that significant improvement in the mass transfer rate in a slug flow through circular tube with immobilized enzyme on the inner wall can occur due to radial mixing of slug flow. Oliver and Hoon [71] have reported a significant enhancement of heat transfer in slug flow.

In the application of the Taylor bubble flow for enhanced heat transfer in capillary tubes, both phase change flow and non-phase change flow have been considered. A number of studies of heat transfer phenomena in the slug flow regime have revealed that there is a large increase in the wall heat flux and the Nusselt number increases in 1.2 [72] to 6 [73] times that of a pure liquid flow, depending on the operating condition.

Although both phase change flow and non-phase change have proven to be promising heat transfer technologies in micro scale applications, the dominant mechanisms of heat transfer associated with the two modes are different due to the different role the gas bubble plays.

The dominant heat transfer mechanism for non-evaporating or condensing Taylor bubble flow is related to the recirculating flow field in the liquid slug close to the bubble.

On the other hand for phase changing flow, whether in a superheated liquid or gas, the phase interface provides a sink at the saturation temperature to remove the heat from the wall. Thus, the gas bubble region and the thin liquid film often plays the most critical role in the overall heat transfer and the quick expansion of the gas phase makes the slug and annular regime prevalent. The main advantages of two-phase flow boiling heat transfer over other cooling methods can be summarized as (a) high energy absorption by the latent heat of vaporization, (b) lower mass flow rate and pressure difference required (c) lower temperature gradients due to saturated flow conditions and (d) the increases of heat transfer coefficient as heat flux increase.

6.2 Literature Review

Due to the limitation of experimental methods to measure internal flow and thermal fields in microchannels or tubes, a detailed understanding of the local features of hydrodynamic and heat transfer characteristics of slug flow have begun to emerge recently with the development of accurate DNS methods for multiphase flow. The numerical studies on non-evaporating or condensing flow has been studied in larger amount compared to studies of phase changing Taylor bubble flow. Fukagata et al. [74] carried out a numerical study on the flow and heat transfer characteristics of a bubble flow train without phase change using level set method. They were able to obtain qualitative agreement with experimental results regarding wall temperature and found higher local Nusselt numbers beneath the bubble compared to single-phase flow. Narayanan and Lakehal[75] carried out numerical simulations to study the effect of gravity on the two-phase flow heat transfer in small diameter pipes. They notice that the wall heat transfer is 3 to 4 times greater than that of pure water but the effect of gravity, which increases the bubble breakup frequency, is limited in the case of average

Nusselt numbers. He et al. [76], using phase field method, studied the heat transfer without phase change in a micro tube for slug flow and found that the presence of a gas bubble causes recirculating flow inside a liquid slug, which enhances heat transfer. A heat transfer model as a function of parameters such as slug length, flow rate of gas and liquid was proposed based on negligible gas heat capacity and conductivity and one-dimensional unsteady heat conduction in liquid film. Gupta et al. [77] utilized two commercial codes to compare the VOF method (using Fluent) and the level set method (TransAT) in the study of gas-liquid flows and heat transfer in microchannels with constant wall heat flux and constant wall temperature boundary conditions. They reported around 2.5 times higher Nusselt numbers than for liquid phase flow and claimed that the liquid radial flow at the nose and tail are the basis for enhancement in heat transfer. In their follow up work [78], validation studies were carried out to substantiate their numerical studies with experiments. The conditions varied for Reynolds numbers in the range 22 – 1189 and Capillary number of 0.003 – 0.160 with water/nitrogen and ethylene glycol/nitrogen as working fluids. They found close agreement with regards to bubble dynamics and heat transfer rates. They argued that above Reynolds number of about 1000, the flow is no longer axisymmetric.

With regards to numerical studies of slug flow with phase change, Mukherjee and Kandlikar [79] studied of growing water vapor bubble in microchannels using the level set method. They observed a steady initial bubble growth surrounded by superheated liquid followed by a rapid axial expansion after the bubble fills the channel cross section. The authors also found that the bubble growth increased with the liquid superheat and decreased with an increase in the Reynolds number due to a thicker liquid film and thinner thermal boundary layer. Later, Mukherjee [80] studied nucleating vapor bubbles in a 0.2mm microchannel and compared with nucleate pool boiling. The author found that the decrease in the contact angle suppresses the increase of dry-out area. He argued that the thin film governs heat transfer and bubble growth for such problems. More recently, Mukherjee et al. studied the problem in [80] and reported that wall heat transfer does not depend on the liquid flow rate

and the surface tension. However, their implementation of surface tension and phase change was on the diffused interface, surface force model [38] using the standard diffused mass source term. Such an approach is susceptible to large errors especially in the case of water in micro-scale channel because of large density contrast and high surface tension. Zu et al. [81] used VOF with a pseudo-boiling approximation in Fluent and carried numerical study on bubble nucleation in flow boiling channels. The authors compared their results with experimental observations and 1-D theoretical models and found close agreements. Zhuan and Wang [82] performed VOF simulation of flow boiling for R134a and R22 fluids in a 0.50 mm circular channel. These authors analyzed a wide range of flow pattern such as bubbly flow, bubbly/slug flow, slug flow and slug/semi-annular flow depending on bubble evolution as well as the effect of fluid properties on the location of transition lines. The flow patterns and the bubble frequency distribution at the outlet were compared with experimental observations.

The above studies used the standard VOF method which can suffer from inaccuracies in the computation of the surface tension force [83] and dissipation of interface [82]. Suh et al. [84] used level set based method with the sharp interface approach to study flow boiling of a bubble in parallel microchannels. They demonstrated that a backward bubble expansion causing reverse flow can occur when the bubble formation is not simultaneous in multiple microchannels and it is more pronounced as contact angle decreases and the wall temperature increases. Magnini et al. [85] used the VOF method in Fluent using the Height Function (HF) approach for improved curvature calculation to simulate a single elongated bubble with phase change in circular microchannels. The authors found that the HF method enhanced the curvature calculation greatly. They reported that the bubble accelerates downstream and that the liquid film is the dominant heat transfer mechanism. They argued that the main boiling mechanism in the slug flow regime is not nucleate boiling. A transient-heat-conduction-based boiling heat transfer model for the liquid film region was proposed. A detailed review of numerical studies on the Taylor bubble until 2012 is presented in [86] and a review on the studies of heat transfer with no phase change in [87].

The effects of mixture velocity, gas void fraction, liquid and gas inlet velocities and geometry of the tube or channel have been considered in the literature [75, 77, 85]. However, a fundamental understanding of the heat transfer mechanisms in boiling slug flow is still lacking. Phase change can strongly affect bubble fluid dynamics particularly for large Re and large Ca flows where low surface tension force can lead to stronger interfacial instabilities.

The current research focuses on systematically identifying the detailed effect of each dimensionless parameter, in particular capillary number, Reynolds number and Froude/Bond number and on the heat transfer in Taylor bubble flow with phase change. The utilization of accurate numerical algorithm can also benefits the study.

6.3 Scaling Factors and Dimensionless Parameters

The dimensionless parameters relevant to the current study are the capillary number, Reynold number, Froude number, Stefan number and Prantl number, and they are defined as follow:

$$\begin{aligned} Ca_b &= \frac{\mu_l U_{tb}}{\sigma} \\ Re &= \frac{\rho_l U_{sl} D}{\mu_l} \\ Fr &= \frac{U_{sl}}{\sqrt{gD}} \\ St &= \frac{C_{p,l}(T_{wall} - T_{sat})}{h_{gl}} \\ Pr &= \frac{\mu_l C_{p,l}}{k_l}, \end{aligned} \quad (104)$$

where the scaling factors D , U_{sl} and U_{tb} are tube diameter, the superficial liquid inlet velocity and the bubble tip velocity respectively. The velocity, length, time and pressure in the governing equations are non-dimensionalized using U_{sl} , D , D/U_{sl} and $\rho_l U_{sl}^2$, respectively.

For superheated liquid evaporating condition, the temperature is normalized as

$$T' = \frac{T - T_{sat}}{T_{wall} - T_{sat}} . \quad (105)$$

and the heat transfer rate on the wall can be described with the local Nusselt number as

$$\text{Nu} = \frac{D}{(T_{wall} - T_{sat})} \left. \frac{\partial T}{\partial r} \right|_{r=D/2} , \quad (106)$$

and with the mean Nusselt number as

$$\overline{\text{Nu}} = \frac{1}{L_d} \int_0^{L_d} \text{Nu} \, dx , \quad (107)$$

where T_{wall} and T_{sat} is the wall temperature and the saturation temperature respectively.

6.4 Numerical Methods

The current research aims to study the heat transfer phenomena for the evaporating Taylor bubble flow in a vertical tube with constant wall temperature. The governing equations and the numerical methods are described above in Chapter 2 and 3.

There are two main types of computational domain that have been commonly used to study the Taylor bubble flow: the moving frame and the fixed frame of reference. The moving frame of reference, where the computational domain follows the bubble, requires a much smaller mesh size which lowers the computational cost. It is thus suitable for studying steady or quasi-steady dynamics of a single bubble with streamwise periodicity. Also, it allows the researcher to easily control the bubble and liquid slug length ratio if the focus are on the homogeneous void fraction effect on the flow or heat transfer characteristics. On the other hand, a fixed frame domain typically includes a junction or a nozzle at the inlet region and has been utilized to study the entrance effect such as the liquid-gas inlet mass flux ratio on

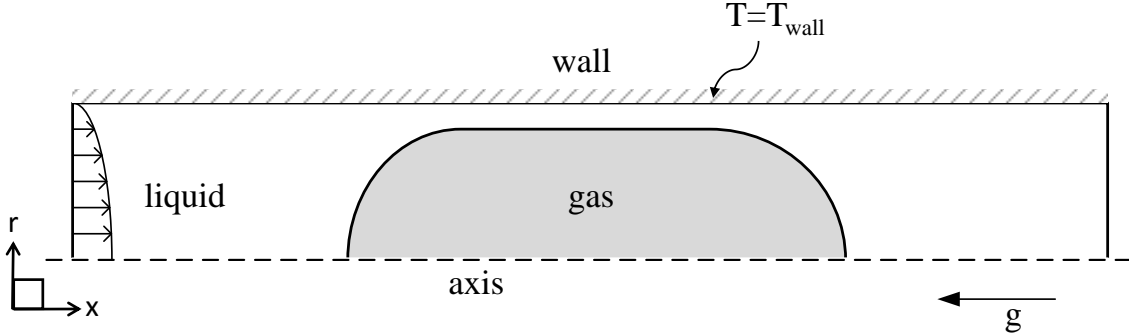


Figure 59: Schematic of computational domain for Taylor bubble flow.

the periodic release of bubbles.

A moving frame of reference is used for the current research in order to efficiently study the long term behaviors of evaporating Taylor bubble as well as a wide range of dimensionless parameters where the length scale and the time scale can differ by orders of magnitude. There are a few approaches to implement the moving computational domain. Here, the moving wall boundary condition is applied in which the bubble tip velocity U_{tb} is used to update the moving wall velocity U_{wall} at each time step as

$$U_{wall}|_{r=R/2} = -U_{tb} , \quad (108)$$

and the inlet velocity as

$$U_{in} = U_{sl} - U_{wall} . \quad (109)$$

where U_{in} is the updated velocity inlet boundary condition. Fig. 59 shows a schematic of the computational domain used here.

The moving axisymmetric computational domain of circular tube has diameter of D and the length is $L_d = 8D$. The bubble is initially placed at the center of the computational

Table 7: Properties of Nitrogen and Ethylene glycol at 294.15K.

Phase	ρ [kg/m ³]	μ [μ Pa· s]	C_p [J/kgK]	k [W/mK]	σ [N/m]
Nitrogen	1.126	21.2	1040	0.0242	
Ethylene glycol	1107	14000	2627	0.2510	0.048

domain thus the bubble entrance effect is not considered in current simulations. Also a single evaporating bubble is taken into account by assuming that neighboring bubbles are far and interference effects are negligible. Due to phase change, the solution is transient in nature and the bubble growth from about $1.74D$ to $4D$ has been considered in current study. The initial bubble shape is a hemispherical cap on each end. The initial bubble length is $4R_b$ and the bubble radius is $R_b = 2/3D$. The radius is defined roughly based on the prediction of liquid film thickness because although the quasi-steady bubble shape is independent of the initial setup, closer initialization can reduce the computational time to reach it.

As mentioned, the inlet boundary condition is set with the inlet velocity U_{in} which varies in time together with the moving wall velocity. A symmetric boundary condition is used at $r = 0$ and a zero pressure boundary condition at outlet. Note that, in some earlier studies, periodic boundary conditions were used at the inlet and outlet. However it is not easily applicable to heat transfer studies due to the energy flow being not the same at the inlet and outlet.

6.5 Validation with Adiabatic Taylor Bubble Flow in Vertical Tube

Simulation of a Taylor bubble flow under isothermal conditions is carried out to validate our method as well as to estimate the required grid resolution for various cases. The adiabatic Taylor bubble flow has been studied extensively by means of experiment and more recently using DNS multiphase methods. Quite a number of predictive models have been developed that estimates the hydrodynamics of the Taylor bubble such as the thickness of the liquid film around the bubble δ , bubble rise velocity U_{tb} , pressure drop, etc, and will be discussed

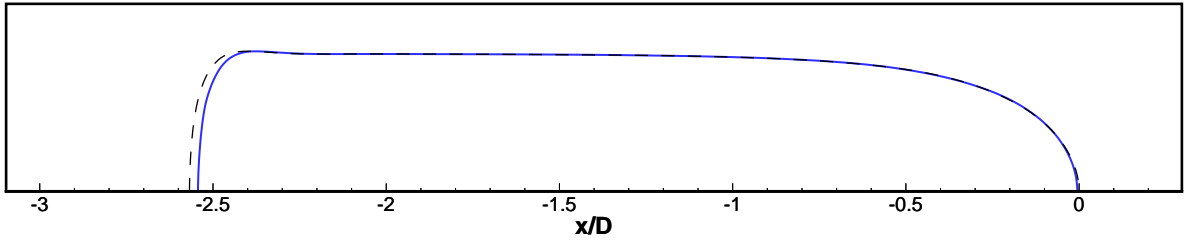


Figure 60: Shape of the bubble for validation case with two grid resolutions (60×960 and 120×1920) at $t = 2$.

with our results.

The validation conditions have been setup as one of the cases in the work of Gupta [78] where both experimental and numerical studies were performed. The properties of the gas and liquid phases are that of nitrogen and ethylene glycol at 294.15K (Table 7). In a tube of radius 0.002m, the velocity of the superficially flowing liquid phase, U_{sl} is 0.37m/s. Grid convergence is tested in Fig. 60 with a 60×960 mesh and a mesh twice as fine. x/D is the normalized distance from the bubble front tip and does not reflect the distance traveled by the bubble. Comparison shows closer match with a small deviation of the bubble tail location but exact match for the bubble thickness and the interface profile. Thus the mesh 60×960 has been used throughout the current research.

Bretherton [88] provided a theoretical work based on the lubrication approximation and predicted the liquid film thickness between the bubble and the wall to be

$$\delta/R = Ca_b^{2/3} . \quad (110)$$

where

$$Ca_b = \frac{\mu_l U_{tb}}{\sigma} . \quad (111)$$

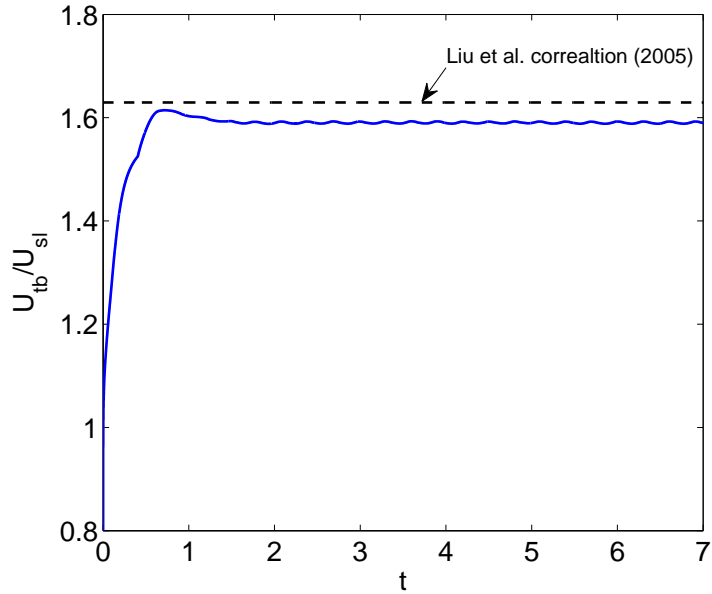


Figure 61: Normalized bubble tip velocity as a function of time for the validation case.

However, it was later found that the film thickness only obeys the Taylors law at small capillary number ($Ca < 0.03$). A more accurate correlation was proposed later by Aussillous and Quere [89] as

$$\delta/R = \frac{1.34 Ca_b^{2/3}}{1 + 1.34 \times 2.5 Ca_b^{2/3}} . \quad (112)$$

where the coefficient 2.5 is empirical. This correlation has been widely used for low Reynold number, $22 < Re < 40$. The thickness obtained from the numerical simulation was $\delta/R = 0.20156$ and the correlation result is 0.2015 while the experimental values from matching capillary number, shown in Fig. 6 of [78], where approximately between 0.21 and 0.22.

A prediction of bubble terminal velocity is given by Liu et al. [90] for upward Taylor flow in vertical channels as

$$U_{tb}/U_{sl} = \frac{1}{1 - 0.61 Ca^{0.33}} . \quad (113)$$

This correlation has been shown to be valid for Ca in range of $0.0002 - 0.39$. Figure 61 shows

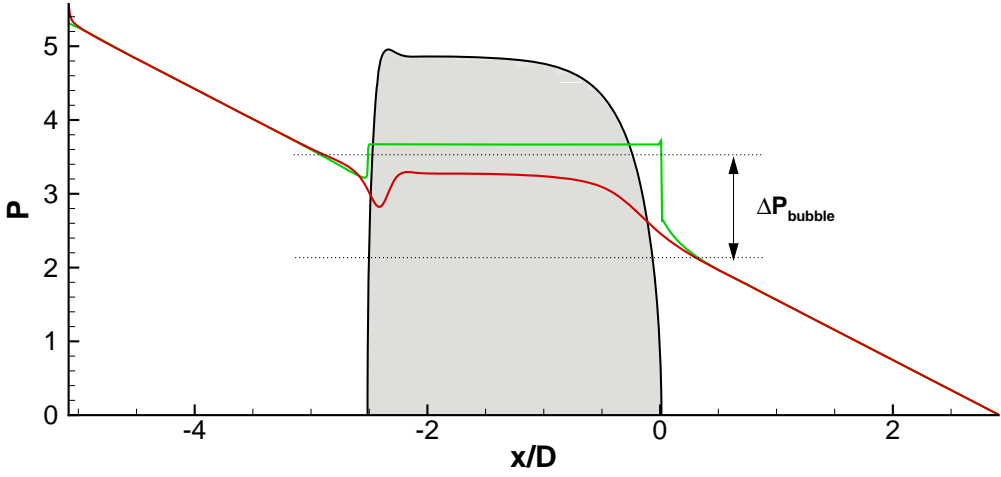


Figure 62: Pressure drop in the tube and sharp pressure jump inside the bubble along the tube center (red) and the wall (green) at $t = 2$.

the bubble rising velocity in time and the result of validation case is in close agreement with the correlation.

In two-phase slug flow the pressure drop increases due to the circulating flow field and the increase of shear stress at the wall. In the liquid slug, the pressure drop is consistent with HagenPoiseuille flow and the shear of the gas phase is negligible within the liquid film region. However, pressure drop over the entire bubble, ΔP_{bubble} , is not zero because the jump at the bubble front is larger than the back. The pressure drop over the computational cell is thus sum of the liquid slug pressure drop and the bubble pressure drop. A pressure drop correlation is given by Kreutzer et al. [91] as

$$\frac{\Delta P}{L_{uc}} = \frac{16}{Re} \left[1 + a \frac{D}{L_s} \left(\frac{Re}{Ca} \right)^{(1/3)} \right] \frac{4}{D} \left(\frac{\rho_l U_{in}^2}{2} \right) \vartheta_l . \quad (114)$$

where L_s is the liquid slug length, ϑ_l is the dynamic liquid hold-up and a is found to be 0.07 for numerical and 0.17 for experimental result. Pressure field along the tube center and the wall is plotted for the current simulation in Fig. 62 at $t = 2$. The above correlation gives the normalized pressure drop over computational domain as 5.635 which is close to the

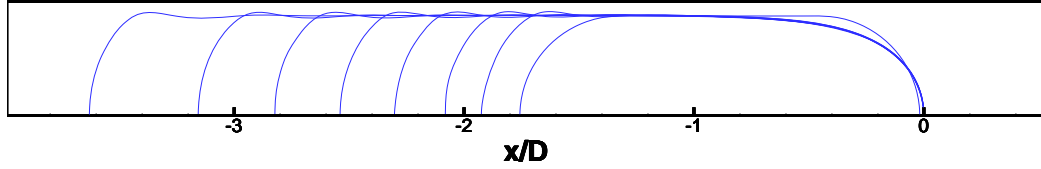


Figure 63: Bubble growing due to evaporation for the reference case. The snap shots are taken at intervals of $\Delta t = 2$.

current simulation result of 5.321. It also shows that the pressure drop along the tube center and the wall is linear in the liquid slug region whereas there is a sharp jump in the pressure due to surface tension force at the bubble. The wall pressure is shown to increase largely at the bubble front and then drops with fluctuation at rear of the bubble. Similar observations were found in [83, 91].

6.6 Results and Discussion

A reference case is setup with: $\rho_g/\rho_l = 0.01$, $\mu_g/\mu_l = 0.01$, $k_g/k_l = 0.02$, $C_{p,g}/C_{p,l} = 0.33$ and the dimensionless number are given as: $\text{Ca} = 0.033$, $\text{Re} = 125$, $\text{Fr} = 2.52$. The length scale corresponds to $D = 0.001\text{m}$ tube diameter and the velocity is scaled with inlet liquid velocity U_{sl} since the bubble tip velocity U_{tb} does not asymptote to a constant value. The properties and the reference scales are varied to setup the conditions to isolate the effects of the dimensionless parameters.

6.6.1 Reference Case

The reference case for the evaporating Taylor bubble is depicted in Fig. 63, where the bubble growth from the initial shape is shown over a time interval of about 10. Here, the bubble quickly forms a stable profile and after that the front and the tail contours are not affected by the growth. Also, the growth rate increases due to an increase in the surface area available for evaporation. In Fig. 64, the normalized bubble tip velocity is plotted as a function of

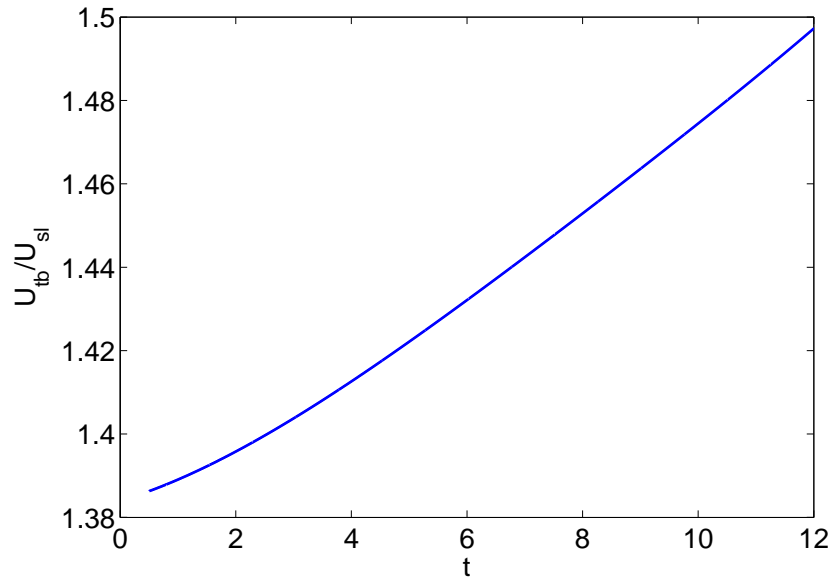


Figure 64: Normalized bubble tip velocity as a function of time for the reference case.

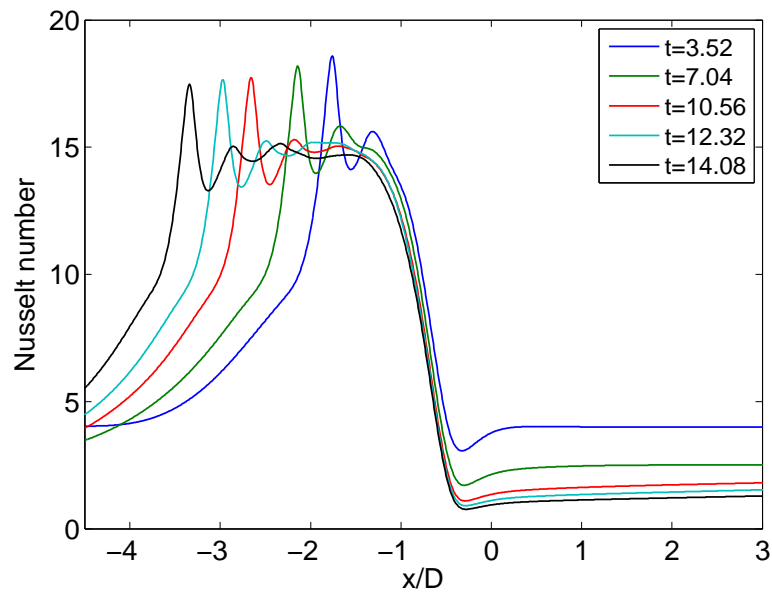


Figure 65: Local Nusselt number evolution in time for the reference case.

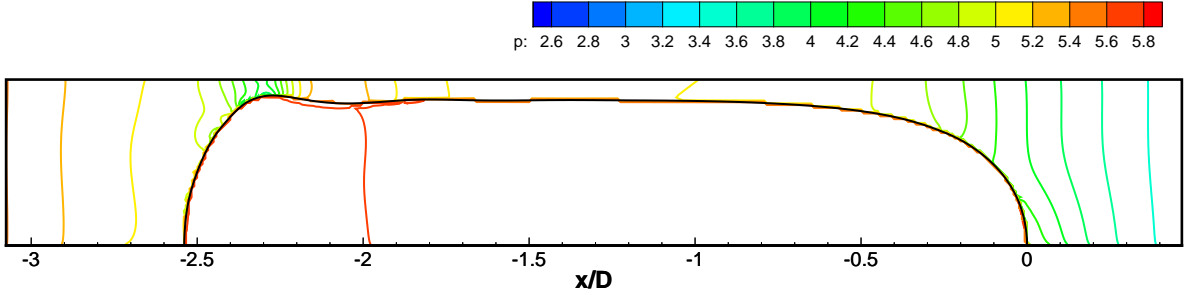


Figure 66: Pressure contours around the reference bubble at $t = 8s$.

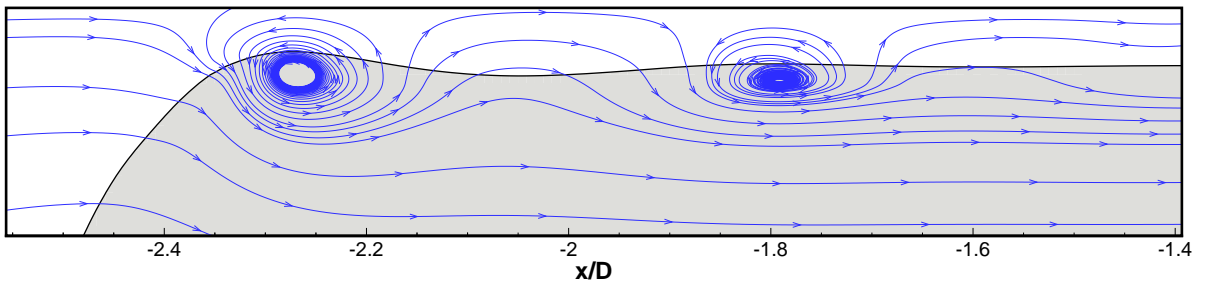


Figure 67: Recirculating flow near the tail of the reference bubble at $t = 8s$.

time. The bubble tip velocity grows exponentially in time due to evaporation and increase in the buoyancy force. In Fig. 65, the local Nusselt number and its development in time is shown. Large jump within the bubble slug can be seen and the major heat transfer occurs due to the thin liquid film. Also, it can be seen here that the characteristic profiles of the Nusselt number are almost identical during the bubble growth with slight decrease due to the thermal boundary development. The fluctuation of the film thickness at the rear of the bubble is due to balance between surface tension and the thin film related momentum flux. The lowest pressure at the exit of liquid film shown in Fig. 66 contributes to the highest crest at the tail. Fig. 65 shows that the maximum wall heat flux at the rear cap of the

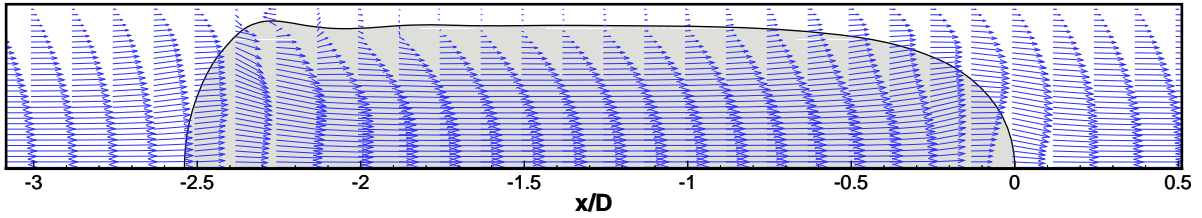


Figure 68: Fluid velocity field of the reference bubble at $t = 8s$.

Taylor bubble as well as smaller fluctuations along the film region to be more amplified than the interface profile. It is found that the location of the trough and the crest of the Nusselt number wave closely match the boundaries and the center of the adjacent vortexes shown in Fig. 67 where the axial velocity is lowest and highest respectively. Similar observations were reported in [77, 92]. In Fig. 68, the fluid velocity field of the reference bubble is shown. Here, it can be seen that the velocity inside the bubble is faster and the velocity at the constant film thickness region is almost stagnant. Thus the gas phase is flowing effectively at a smaller diameter due to the liquid film.

6.6.2 Effect of the capillary number

Results of our parametric study with phase change are discussed next starting with the influence of the capillary number. It is the primary parameter that determines the liquid film thickness concerning microchannel flows. In Fig. 69, the shapes of the bubble in varying capillary numbers are shown. As expected, a monotonic increase in the liquid film thickness and the bubble length is observed. However, the interface profiles of bubble fronts are smooth for all capillary numbers whereas the profiles at near the tails are wavy. A flatter bubble tail can be found as the capillary number increase and at the highest Ca, the thin film thickness decreases almost linearly with out a typical flat region.

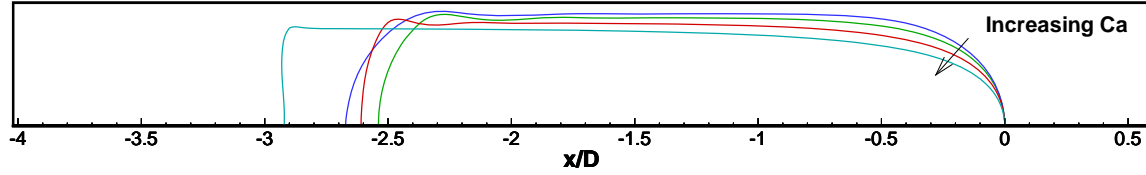


Figure 69: Shape comparison for varying capillary numbers. The colors correspond to the legend in Fig. 70.

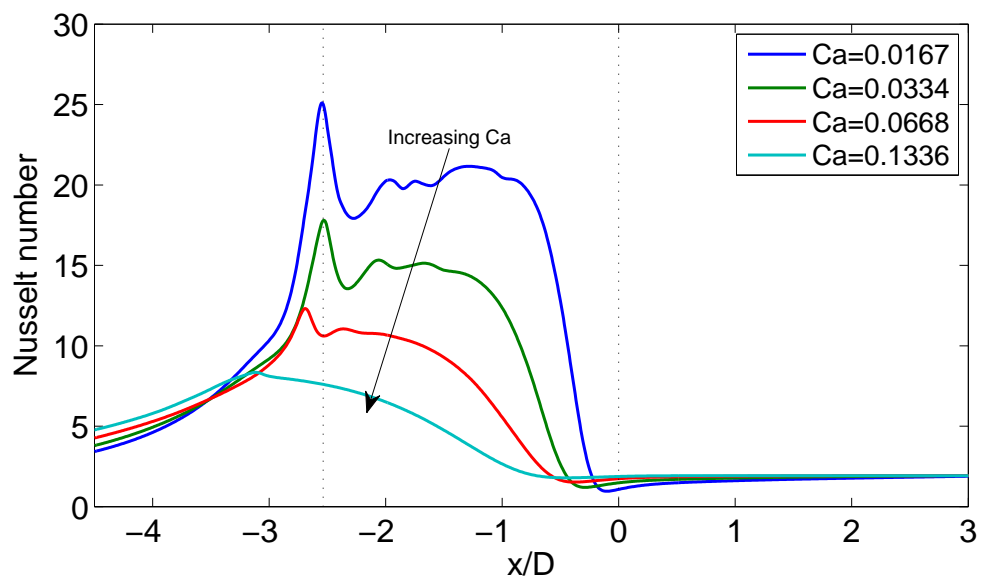


Figure 70: Local Nusselt number distribution within the moving frame of reference with capillary number varying in the range of $0.0167 - 0.1336$. The time is at $t = 8$. Dotted lines show the front and rear of the reference case bubble.

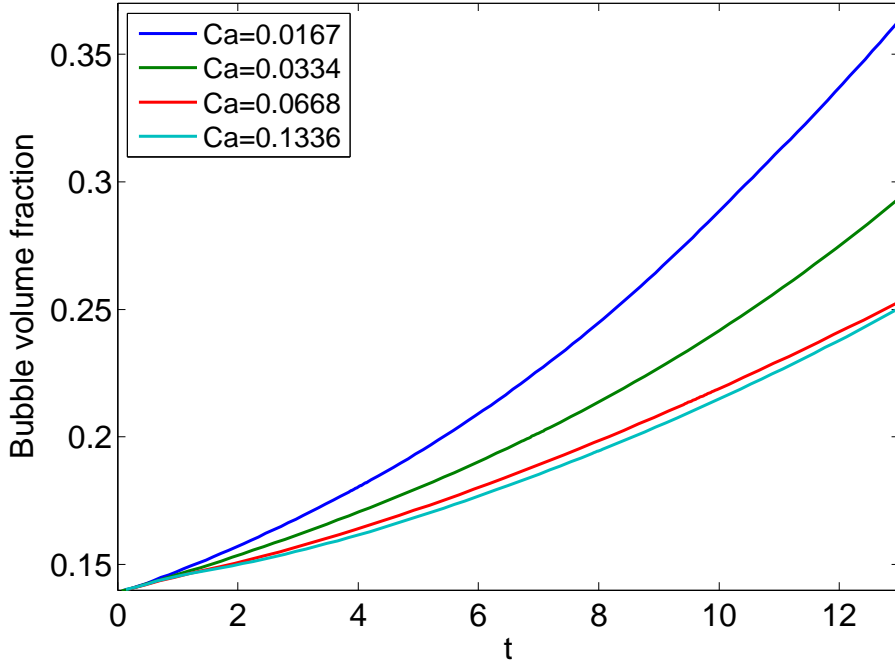


Figure 71: Bubble growth rate for varying Ca . The bubble volume fraction is in reference to the computational domain.

The effect of the capillary number on the local Nusselt number distribution at $t = 8$ is plotted in Fig. 70. First, it shows coordinating result of decrease in the Nusselt number as the capillary number increases which results from the thickening of the liquid film. As the film gets thicker, the Nusselt number fluctuations decrease and vanish for the highest Ca .

Comparison of the bubble growth over time for the varying Ca cases is plotted in Fig. 71. Since the bubble growth rate depends largely on the heat flux at the gas-liquid interface, the lower capillary number exhibits faster growth rate.

6.6.3 Effect of the Reynolds number

Fig. 72 shows the effect of Reynolds number on the local Nusselt number distribution. At low Reynold numbers (< 125), the Nusselt number varies little showing a small decrease near the front of the bubble and a larger peak at the bubble tail as Re is increased. When the Reynolds number is further increased, the jump in Nusselt number becomes flatter and

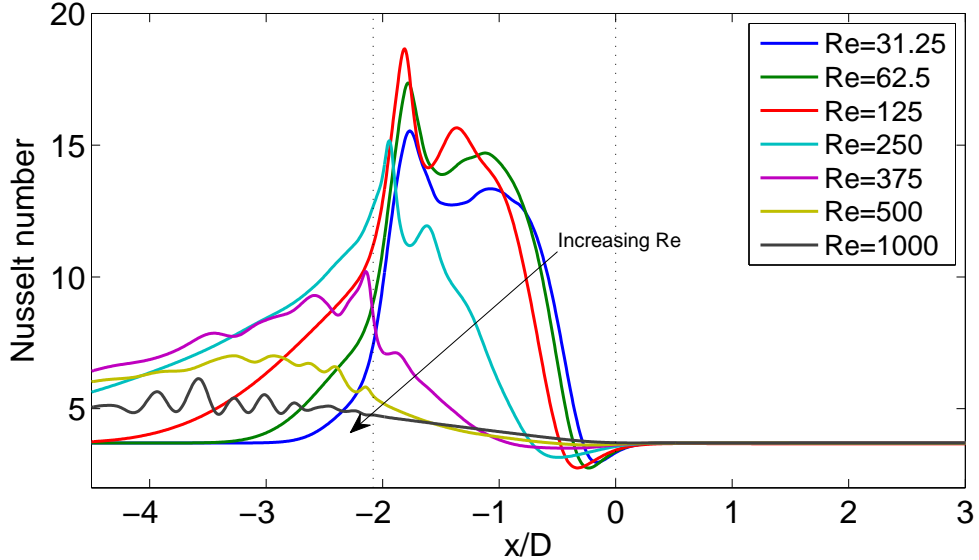


Figure 72: Local Nusselt number distribution within the moving frame of reference with Reynolds number varying in the range of $31.25 - 1000$. The time is at $t = 4$ with respect to the time scale of the reference case, $Re = 125$. Dotted lines show the front and rear of the reference case bubble.

for $Re = 1000$, it becomes completely linear in the gas slug region. For $Re > 500$, the largest Nusselt number distribution at the wall is shifted to the wake of the bubble. The flow instability at the wake grows due to an increase in convection however, it is clear that this cannot by itself account for the large reduction in heat transfer in the liquid film region. In any case, the main mechanism of heat transfer changes from the film to the wake. indicating that beyond this point, the predictive models for boiling slug flow based on the film thickness is not valid. In Fig. 73, the profiles of the bubbles are drawn for varying Re . Again, the bubble front behaves monotonically in response to the Reynolds number. Near the tail of the bubble, however, it develops the wavy profile of the liquid film. Also the shape of the bubble tail changes from hemispherical to a flat shape and then to a concave shape as Re is increased. This is due to a decrease in surface tension and relatively stronger transient recirculation regions in the bubble wake as well as inside the bubble. For $Re > 375$, the wavy profile and the flattened bubble tail begin to show large oscillation.

In order to further investigate the large jump in Nusselt number as well as its decay at

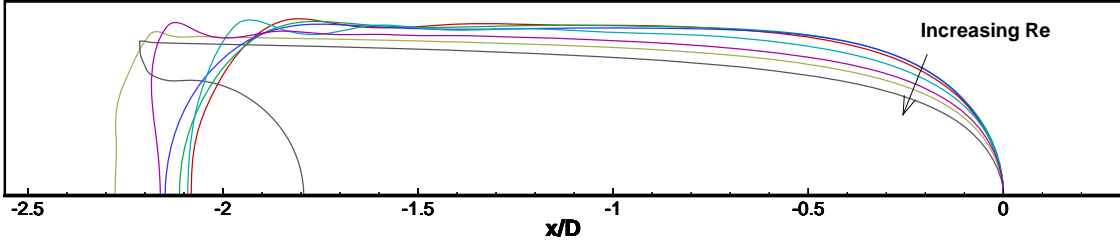


Figure 73: Bubble shape with Reynolds number varying in the range of $31.25 - 1000$. The time is at $t = 4$ with respect to the time scale of the reference case, $Re = 125$. The colors match with the legend in Fig. 72.

high Re , the temperature profiles for the reference case and the $Re = 1000$ are compared in Fig. 74 at the front of the bubble and in Fig. 75 at the tail. First, it can be seen from the streamlines that there is a large recirculating region in front of the reference case bubble and the slight decay of Nusselt number near the bubble tip is attributed to this radial flow field. On the other hand, the case for $Re = 1000$ shows almost no recirculation at all due to the slicker shape of the bubble front. In addition, the bubble tip velocity for the higher Reynolds number was calculated around 48% faster than the reference case and as a consequence, it has much less time to develop the temperature gradient in the liquid film. In Fig. 75, the large peak of Nusselt number at the rear end for the reference case corresponds to the highest crest of the interfacial. A flow instability at the high Reynolds number resulting in vortex shedding can be observed at the bubble tail but as it can be seen from Fig. 72 that its influence on Nu is limited.

Fig. 76 shows the time evolution of the bubble shape and the temperature field for the $Re = 1000$ case. It shows that from the initial setup of bubble, there is a startup effect

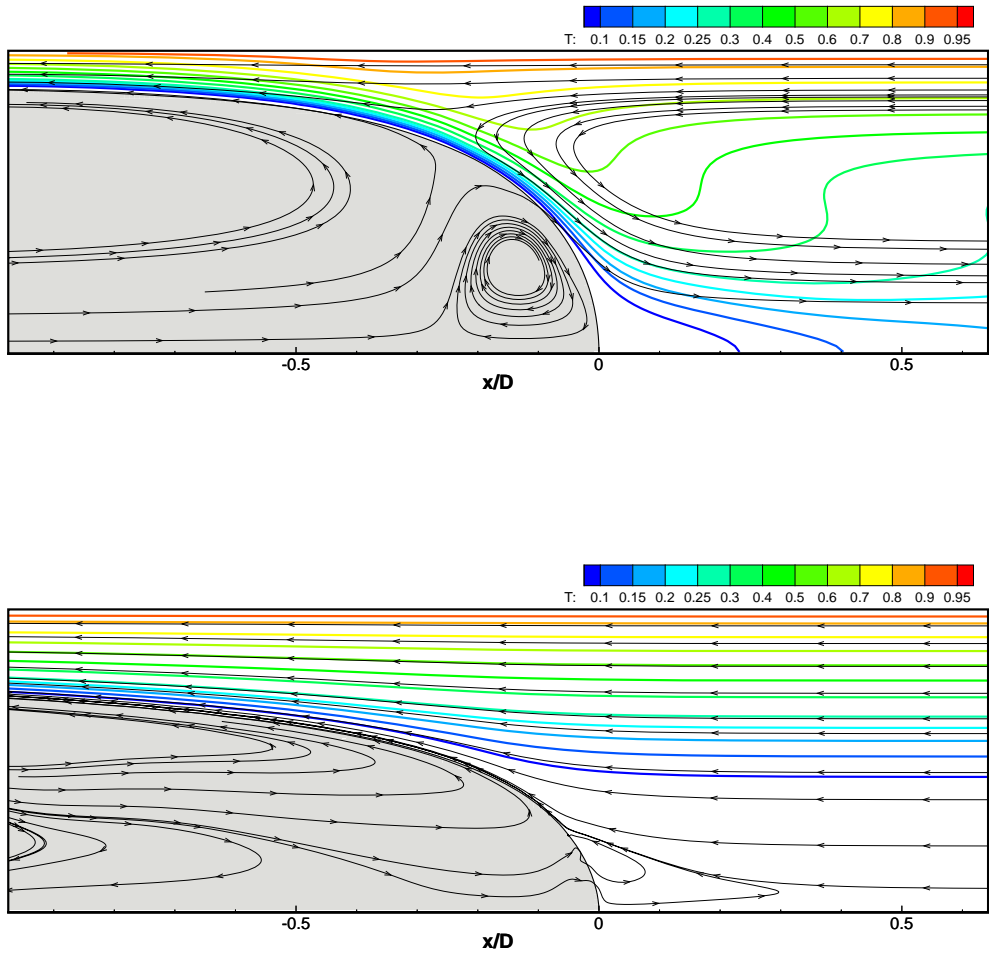


Figure 74: Temperature profiles for the reference (top) and $Re = 1000$ cases (bottom) near the front of the bubbles. The streamlines are based on the velocity relative to the moving frame of reference.

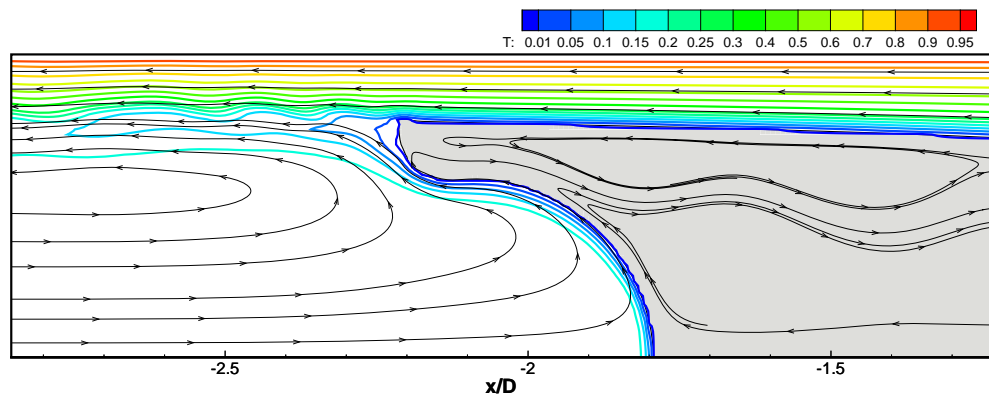
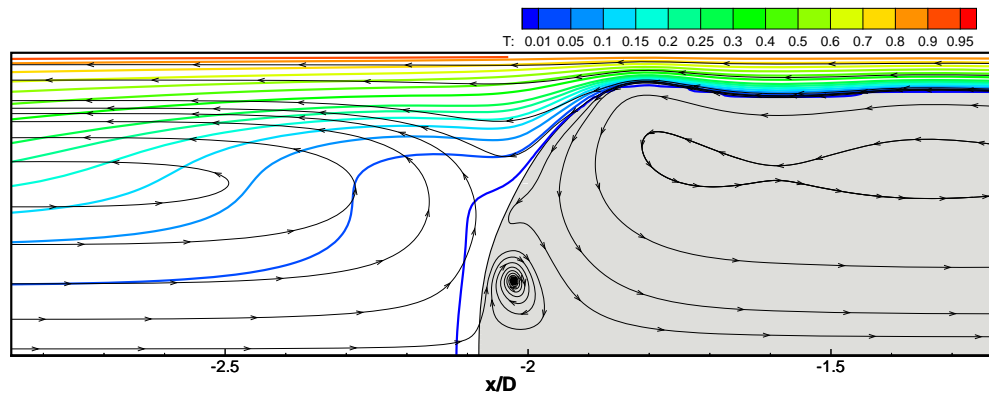


Figure 75: Temperature profiles for the reference case (top) and $Re = 1000$ (bottom) near the tail of the bubble. The streamlines are based on the velocity relative to the moving frame of reference.

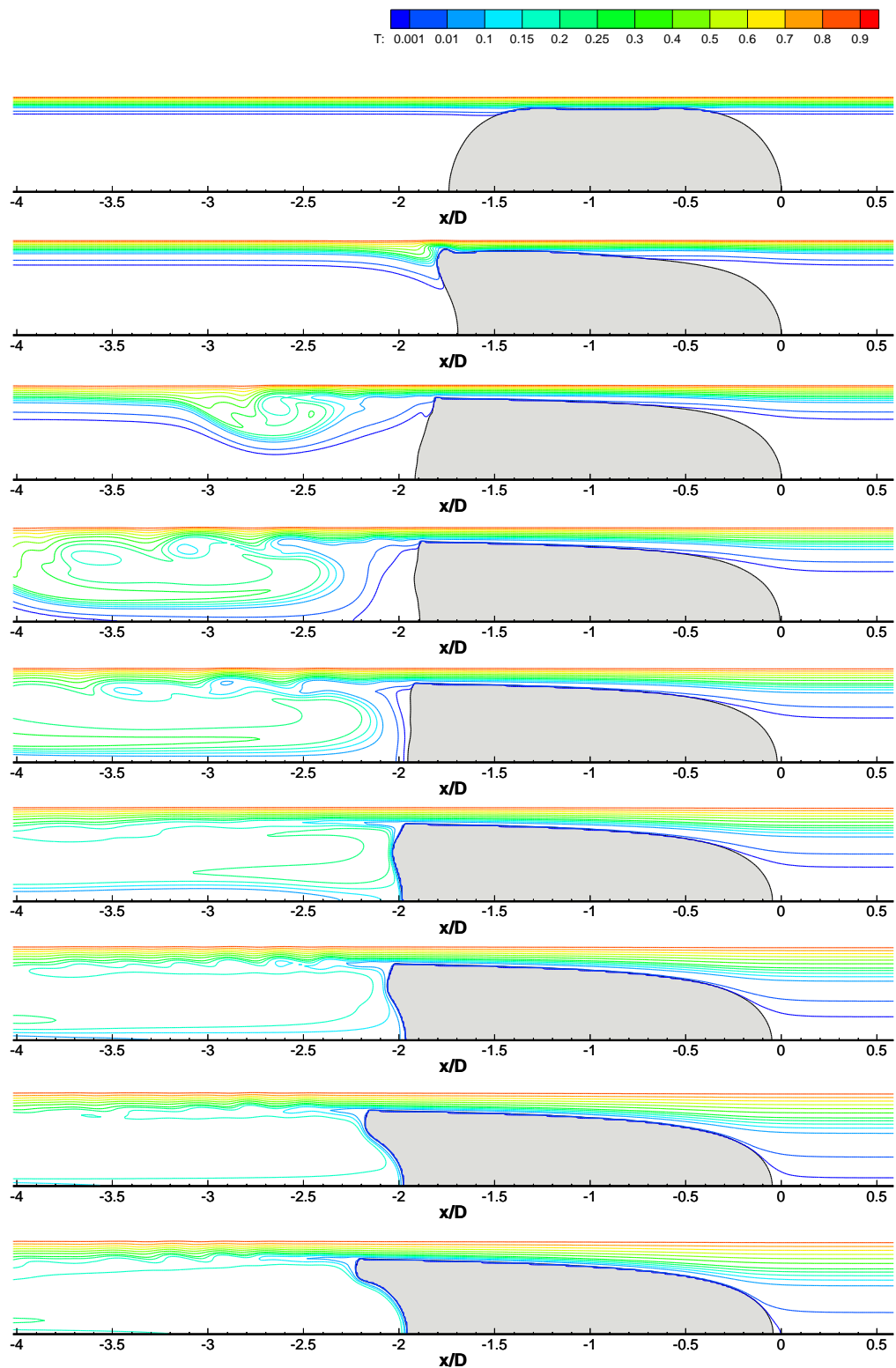


Figure 76: Time evolution of the bubble shape and the temperature contour for $Re = 1000$.

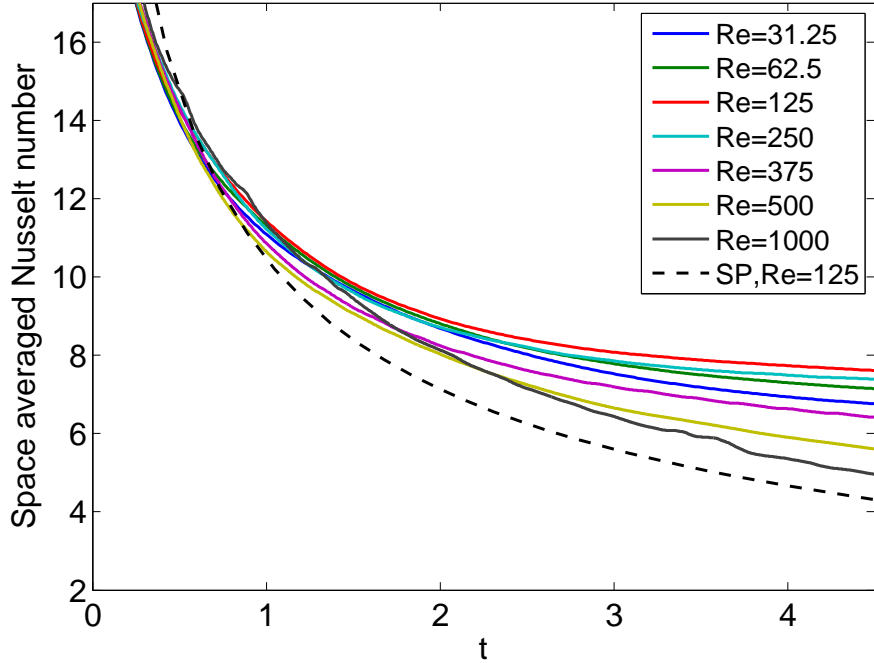


Figure 77: Space averaged Nusselt number evolution in time for varying Re . Dotted line is the Nusselt number of pure liquid flow with constant T_{wall} condition and the domain is moving at the speed of the reference bubble.

causing large recirculating region at the wake. Eventually, the initial effect dissipates and the bubble reaches its terminal characteristic shape.

The space averaged Nusselt number for different Re is plotted against time in Fig. 77 along with the Nusselt number for pure liquid flow. Initially, the space averaged heat flux at the wall decays rapidly and slows down as the thermal boundary layer develops. It is interesting to see that the highest space averaged Nusselt number occurs for the reference case and there is no apparent order to the curves between $Re = 31.25$ to $Re = 375$. This result is in contrast to the monotonic decrease of Nusselt number at the front and at the liquid slug ahead of the bubble. Thus this behavior of space averaged Nusselt number can be attributed to the non-linear effect of wavy shape of the bubble tail region and the oscillation of the bubble rear cap. Fig. 78 shows that the decay of space averaged Nusselt number becomes eventually overwhelmed by the bubble growth and the increase of thin film area.

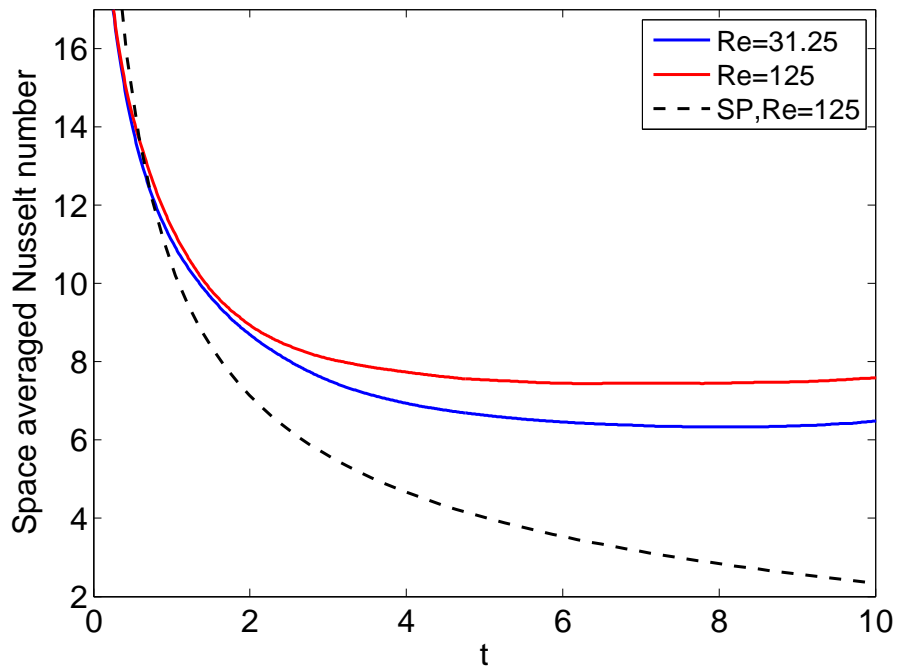


Figure 78: Long term behavior of the space averaged Nusselt number in time. Dotted line is the pure liquid phase with constant T_{wall} condition and the domain is moving at the speed of the reference bubble.

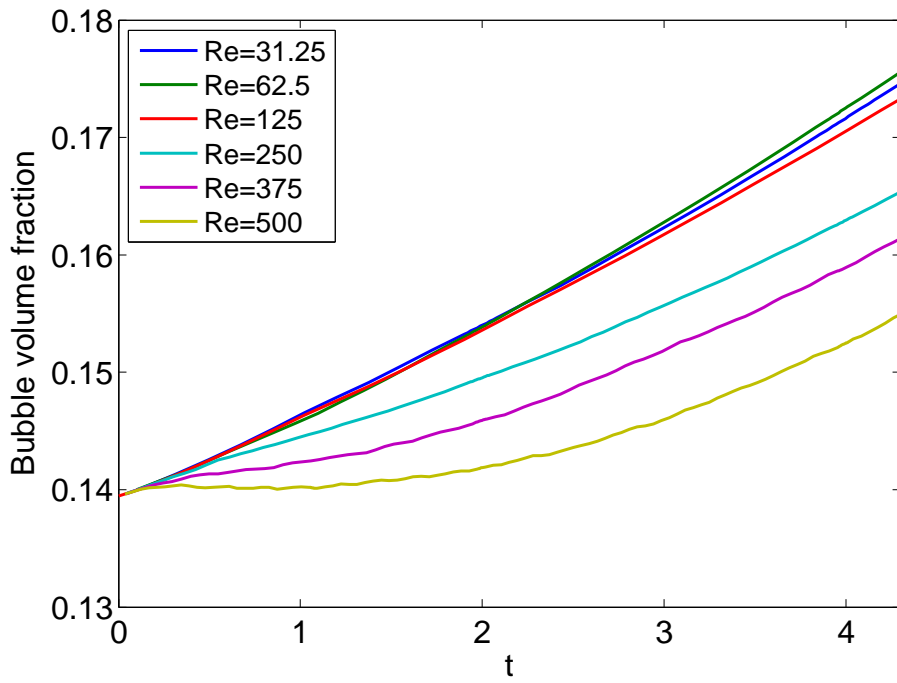


Figure 79: The bubble growth for varying Re . The bubble volume fraction is in reference to the computational domain.

Fig. 79 shows the bubble growth in time. The bubble volume has been normalized with the total volume of the computational domain. The thin film thickness and the characteristic flow field of the low Re cases clearly contributes to higher growth rate and the growth rate increases with time as the interface area increases.

6.6.4 Effect of the Froude number and Other Parameters

The local Nusselt number distributions with respect to the Froude number of half and one fourth of the reference case is plotted in Fig. 80. The effect was found to be minor in comparison to the variation of capillary number and Reynolds number by the same factor but showed clear effect of decrease in the Nusselt number due to increased film thickness.

The difference in the Bond number has been setup with different density contrast unlike the Froude number. The results also showed that the film thickness increases with a relative decrease in the surface tension. The larger growth rate is simply due to the difference in density contrast and thus the different volumetric expansion.

6.7 Conclusions

A study on Taylor bubble flow with heat transfer and phase change in a vertical tube in axisymmetric coordinates has been carried out using the new multiphase, phase change method. A validation case was simulated and a good match was obtained with existing correlations. The influence of dimensionless parameters: the capillary number (Ca), the Reynolds number (Re) and the Froude number (Fr) on the local Nusselt number as well as other two-phase flow characteristics such as the bubble shape, the liquid film thickness and the bubble rise velocity have been investigated. In particular, the results showed that the thin liquid film is indeed the dominant heat transfer mechanism for small Re (<500) but beyond that point the main mechanism has been identified as the flow at the bubble wake.

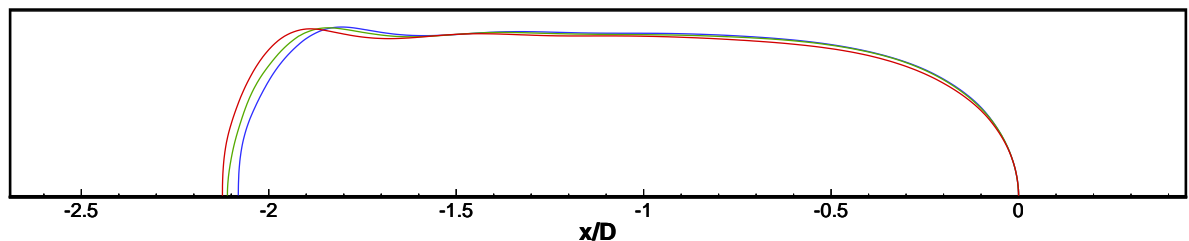
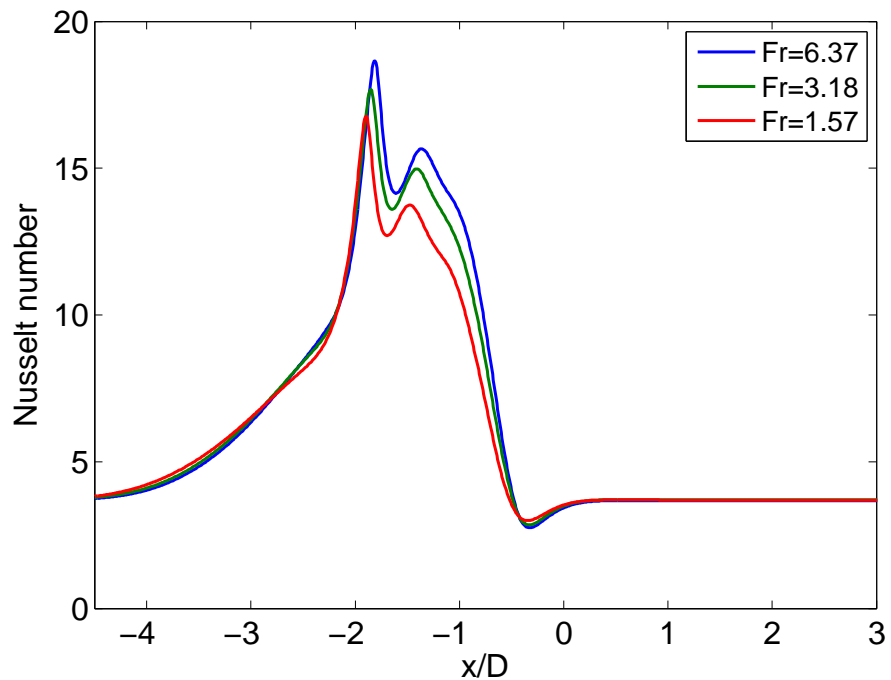


Figure 80: (Top) Local Nusselt number distribution within the moving frame of reference and (Bottom) the bubble shape with Froude number varying in the range of $1.57 - 6.37$. The time is at $t = 4$.

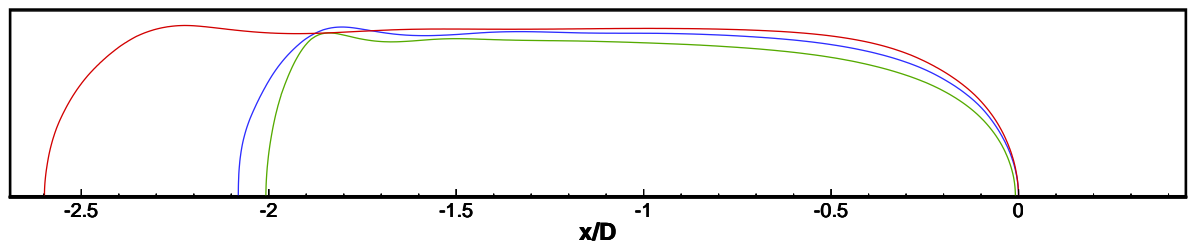
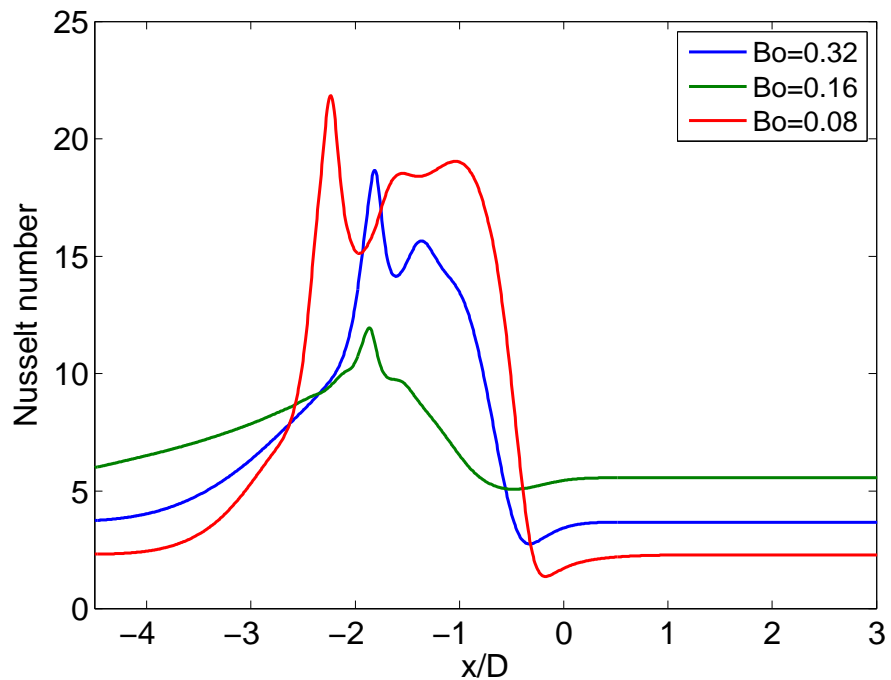


Figure 81: (Top) Local Nusselt number distribution within the moving frame of reference and (Bottom) the bubble shape with Bond number varying in the range of $0.08 - 0.32$. The time is at $t = 4$.

The transition occurs due to the greater liquid film thickness and oscillations at the bubble tail as well as an increase in flow instability at large value of the Reynolds number. The effect of the capillary number is shown to be monotonically analogous to its effect on the liquid film thickness. Consequently, the Nusselt number decreases with an increase in the capillary number. The Froude number has a relatively minor effect on film thickness and the Nusselt number.

7 Conclusions

During the work of present thesis, two main objectives have been achieved. First, a new numerical methods for multiphase, phase change simulation has been developed. Second, the Taylor bubble flow in a small vertical tube with heat transfer and phase change has been investigated.

7.1 Summary of Research Contributions

The major contributions and the conclusions drawn from achieving these two objectives are listed as follows.

1. Although the sharp interface approach is more realistic, the sharp velocity jump implementation [10] is susceptible to oscillatory pressure and spurious interface velocity when considering practical simulation conditions such as large density difference. The primary contribution of the current work is the resolution of these issues featuring (a) continuous velocity and density fields within a thin interfacial region, (b) temporal velocity correction steps to avoid unphysical pressure source terms and (c) mass flux projection correction for improved mass flux conservation.
 - (a) The smoothed velocity jump condition within a thin interfacial region is shown to provide robust and smooth solutions for both the fluid velocity and the interface velocity, particularly for problems with large density contrasts. Also the large spurious velocity field near an interface induced by using the sharp velocity jump condition is avoided, suppressing an unphysical deformation of the phase boundary. In the past, the main drawback of using a diffused interface model has been the lack of accuracy. However, the new diffused method developed in this work is able to achieve the accuracy with respect to phase change by using an asymmetric

average density distribution within the diffused region along with a the new mass flux projection correction scheme. The use of the ghost fluid technique [10, 19] for the diffused velocity jump condition is also important because for large density contrasts, the velocity jumps a large.

- (b) The numerical basis for large pressure oscillations due to phase change has been identified. When the interface crosses a computational cell, it alters the divergence free condition enforced by the previous calculation of the continuity equation. The non-divergence free condition gives rise to an additional source in the computation of pressure which is neither due to the momentum balance nor the pressure jump condition. Additional measures, including update of the velocity field to the new interface location followed by another projection of the velocity field onto the space of divergence free vectors to ensure that the error is not passed on to the next time step. The algorithm thus solves the variable coefficient Poisson equation twice but the additional computational effort is small because the Poisson coefficient matrix does not need to be factorized for this step. This robust approach has been utilized for implementing the pressure dependent interface temperature.
 - (c) One-dimensional and two-dimensional verification problems clearly indicate the role of curvature dependent numerical errors in the calculation of interface velocity. The numerical error is associated with the mass flux projection from the interface to nearby grid points. A correction factor based on curvature ratio is developed to compensate for the difference in the mass flux away from the interface that improves mass conservation during interface advection. The accuracy of the second order derivative in the curvature calculation is generally lowered when the smoothness of the level set function is degraded. The implementation of the advanced reinitialization scheme introduced in [54] is beneficial in this aspect.
2. The new methods developed in this work have been verified in several one-dimensional

and two-dimensional test problems. First, one-dimensional Stefan and sucking interface problems have been solved. Good agreement has been achieved with the exact solutions. The one-dimensional cases validate the utility of the new diffused interface approach. Second, two-dimensional circular bubble condensation and evaporation cases have been studied. A benchmark test between the proposed methods and existing phase change schemes (a sharp interface method and a smooth interface method) shows improved solutions with respect to interface advection, pressure solution and interface deformation. Overall, about second order accuracy in space is achieved for the complete solution algorithm.

3. Validation with film boiling problems shows good quantitative and qualitative agreement with existing correlations for the Nusselt number and experimental profiles of film boiling shape. A comparison between two-dimensional and axisymmetric simulations has been performed. It shows that the axisymmetric case results in higher and thicker film crests and produces smaller bubbles with higher release frequency. Thick stems are caused by the radial effect of mass transfer and the comparable evaporation taking place at the stem interface. Accordingly, there are less fluctuation in the film thickness as well as Nusselt number. Comparison of the bubble formation shape with a photographic study [69] shows excellent similarity.
4. An in-house code with advanced level set schemes, not available in most commercial (ex. Fluent) or open-source (OpenFOAM) softwares, has been developed. Although the level set method provides benefits in interfacial representation over the more commonly used volume of fluid method, there are not many implementations or applications of the level method in commercial codes in the literature at this time. This is primarily due to the fact that level set methods are usually accompanied by high order schemes and sharp interface methods. The development of an in-house code allows significant flexibility in implementing and testing new schemes for consistently evolving methods

like the level set method. However it requires a considerable amount of time and work to develop. The code developed here is applicable to other boiling or condensation problems with minor modifications and also can be extended to more complex problems such as three-dimensional or immersed solid cases.

5. Simulations of Taylor bubble with heat transfer and phase change have been carried out. The characteristics of the Taylor bubble flow with heat transfer and phase change are investigated for a range of dimensionless parameters, including, Reynolds number, Capillary number and Froude number. Particular focus has been on the transition of the main heat transfer mechanism from the thin film to the wake of the bubble. The onset of Kelvin-Helmholtz instability, which is induced by the density and the velocity difference between the bubble and liquid film, has been observed in cases where the Reynolds number was above 500. In case of large relative surface tension forces, the instability is restrained. The averaged Nusselt number within the moving computational domain increases as the bubble evaporates and the growth rate becomes exponential. The effect of the of Ca has shown to be analogous to the film thickness correlation and the bubble growth result in the increase in the flat region only. The Froude number showed insignificant effect on the Nusselt number variation under investigated conditions.

7.2 Publications and Presentations

1. Moon Soo Lee, Amir Riaz, Reinhard Radermacher, Numerical simulation of Taylor bubble flow boiling in vertical tube with heat transfer and phase change, *Under internal review. To be submitted, 2016.*
2. Moon Soo Lee, Amir Riaz, Reinhard Radermacher, Diffused interface method with non-oscillatory pressure for velocity jump condition for incompressible multiphase, phase-change simulations, *To be submitted at Journal of Computational Physics, 2015 November.*
3. Long Huang, Moon Soo Lee, Khaled Saleh, Vikrant Aute, Reinhard Radermacher, A computational fluid dynamics and effectiveness-NTU based co-simulation approach for flow mal-distribution analysis in microchannel heat exchanger headers, *Applied Thermal Engineering 65 (12), 2014, 447457*
4. Moon Soo Lee, Vikrant Aute, Amir Riaz and Reinhard Radermacher, Numerical Simulation of Multiphase Flow with Phase-change, In Proceedings of the 14th International Refrigeration and Air Conditioning Conference at Purdue, 2010.
5. Moon Soo Lee, Amir Riaz, Direct Numerical Simulation of Incompressible Multiphase Flow with Phase Change, Research Symposium on Environmental and Applied Fluid Dynamics Tuesday, May 26, 2015, George Washington University
6. Moon Soo Lee, Amir Riaz, Diffused interface ghost fluid method for incompressible multiphase, phase change simulations, In 66th Annual Meeting of the APS Division of Fluid Dynamics, 58 (18), 2013.

7.3 Future Work

The primary objective of current thesis has been to establish a robust and accurate numerical solution algorithm for solving multiphase flow with phase change. The developed method has been applied to 2-D simulation of evaporation and condensation of bubbles and 2-D film boiling problems mainly for validation purposes. However, the method is developed to be applicable to versatile cases that involves phase change with real physical parameters.

Thus it is logical to consider the opportunities for future work by observing the pool boiling or flow boiling regimes. For pool boiling, the nucleate boiling regime has been studied by many such as in [15, 93, 94, 95, 96] where the implementation of contact angle model and micro-region model beneath the bubble [93] have been the major challenges. The nucleate boiling simulation has also been considered in conjunction with the conjugate heat transfer in the heated wall as well as the effect of wall surface conditions such as micro-groove structures. However, there are still works to be done on where the individual nucleation sites merge to form gas film or where the film experience local dryout. The understanding of transition boiling regime is still very limited due to its chaotic nature and there are much to be investigated such as the burn-out conditions and Leidenfrost point. Three-dimensional simulations are required in order to study more complex and realistic phase change phenomena and consequently, optimization of the computational speed is essential. Thus it requires simultaneous efforts to implement both. High performance computing is achieved by parallelizations of the solution algorithms using either MPI or OpenMP. Ideally, the MPI is desired for higher scalability of multi-core computing but OpenMP is easier to program and can be quickly utilized partially for parallelization expensive loops since most modern solvers for linear system of equations are already parallelized. Adaptive grid meshing technique can also greatly improve the computational efficiency and should be consider a potential future work. Min and Gibou [97] introduced a non-graded adaptive cartesian grids method which gives overall second order accurate level set method.

The simulations of evaporating Taylor bubble in current thesis has revealed other potential studies on the slug flow regime. The parametric studies carried out in current thesis show that there is a transition of the main heat transfer mechanism with respect to variation of Reynolds number which implies the change of governing parameter from the capillary number to the Weber number. A similar trend can be found for example in Fig. 15 of [92] where a drop in the Nusselt can be found after Reynolds number of about 800. The existing correlations for heat transfer have shown inconsistent and limited accuracy [87] and the effect of the Reynolds number at capillary number has been mostly considered monotonic. Another future study can be directed to the critical heat flux. Under evaporating condition, the growing Taylor bubble can become in contact with the heated wall [79]. This local dryout significantly degrades the local wall heat transfer rate and lead to burnout of wall materials depending on the operating conditions. Such phenomena strongly depends on the flow instability, the Laplace force, the rate of evaporation at the liquid film and nucleation at the wall surface. Due to the nature of such study involving thin liquid film and evaporation at the interface, the numerical simulations of such flow require high resolution as well as advanced numerical schemes to obtain accurate solution.

References

- [1] Samuel W. J. Welch. Local Simulation of Two-Phase Flows Including Interface Tracking with Mass Transfer. *Journal of Computational Physics*, 121(1):42–54, 1995.
- [2] G. Son and V.K. Dhir. Numerical Simulation of Saturated Film Boiling on a Horizontal Surface. *Journal of Heat Transfer*, 119(5):25–54, 1997.
- [3] Damir Juric and Grétar Tryggvason. Computations of boiling flows. *International Journal of Multiphase Flow*, 24(3):387–410, April 1998.
- [4] Asghar Esmaeeli and Grétar Tryggvason. Computations of film boiling. part i: numerical method. *International journal of heat and mass transfer*, 47(25):5451–5461, 2004.
- [5] Asghar Esmaeeli and Grétar Tryggvason. Computations of film boiling. Part II: multi-mode film boiling. *International Journal of Heat and Mass Transfer*, 47(25):5463–5476, December 2004.
- [6] Asghar Esmaeeli and Grétar Tryggvason. A front tracking method for computations of boiling in complex geometries. *International Journal of Multiphase Flow*, 30(7-8):1037–1050, July 2004.
- [7] Samuel W.J. Welch and John Wilson. A Volume of Fluid Based Method for Fluid Flows with Phase Change. *Journal of Computational Physics*, 160(2):662–682, May 2000.
- [8] G. Son and V.K. Dhir. Numerical Simulation of film Boiling Near Critical Pressures With a Level Set Method. *Journal of Heat Transfer*, 120(1):183–192, 1998.
- [9] G. Tomar, G. Biswas, a. Sharma, and a. Agrawal. Numerical simulation of bubble growth in film boiling using a coupled level-set and volume-of-fluid method. *Physics of Fluids*, 17(11):112103, 2005.

- [10] Frédéric Gibou, Liguo Chen, Duc Nguyen, and Sanjoy Banerjee. A level set based sharp interface method for the multiphase incompressible NavierStokes equations with phase change. *Journal of Computational Physics*, 222(2):536–555, March 2007.
- [11] Gihun Son and Vijay K. Dhir. Three-dimensional simulation of saturated film boiling on a horizontal cylinder. *International Journal of Heat and Mass Transfer*, 51(5-6):1156–1167, March 2008.
- [12] Woorim Lee, Gihun Son, and Jae Jun Jeong. Numerical analysis of bubble growth and departure from a microcavity. *Numerical Heat Transfer, Part B: Fundamentals*, 58(5):323–342, 2010.
- [13] Woorim Lee, Gihun Son, and Han Young Yoon. Direct numerical simulation of flow boiling in a finned microchannel. *International Communications in Heat and Mass Transfer*, 39(9):1460–1466, 2012.
- [14] Sébastien Tanguy, Thibaut Ménard, and Alain Berlemont. A level set method for vaporizing two-phase flows. *Journal of Computational Physics*, 221(2):837–853, 2007.
- [15] Yohei Sato and Bojan Ničeno. A sharp-interface phase change model for a mass-conservative interface tracking method. *Journal of Computational Physics*, 249:127–161, 2013.
- [16] S. Hardt and F. Wondra. Evaporation model for interfacial flows based on a continuum-field representation of the source terms. *Journal of Computational Physics*, 227(11):5871–5895, May 2008.
- [17] Jan Schlottke and Bernhard Weigand. Direct numerical simulation of evaporating droplets. *Journal of Computational Physics*, 227(10):5215–5237, May 2008.
- [18] Sébastien Tanguy, Michaël Sagan, Benjamin Lalanne, Frédéric Couderc, and Catherine

Colin. Benchmarks and numerical methods for the simulation of boiling flows. *Journal of Computational Physics*, 264:1–22, 2014.

- [19] Duc Q Nguyen, Ronald P Fedkiw, and Myungjoo Kang. A boundary condition capturing method for incompressible flame discontinuities. *Journal of Computational Physics*, 172(1):71–98, 2001.
- [20] Theodore L Bergman, Frank P Incropera, and Adrienne S Lavine. *Fundamentals of heat and mass transfer*. John Wiley & Sons, 2011.
- [21] G Ryskin and LG Leal. Numerical solution of free-boundary problems in fluid mechanics. part 1. the finite-difference technique. *Journal of Fluid Mechanics*, 148:1–17, 1984.
- [22] G Ryskin and LG Leal. Numerical solution of free-boundary problems in fluid mechanics. part 2. buoyancy-driven motion of a gas bubble through a quiescent liquid. *Journal of Fluid Mechanics*, 148:19–35, 1984.
- [23] G Ryskin and LG Leal. Numerical solution of free-boundary problems in fluid mechanics. part 3. bubble deformation in an axisymmetric straining flow. *Journal of Fluid Mechanics*, 148:37–43, 1984.
- [24] Jay P. Boris Elaine S. Oran. *Numerical simulation of reactive flow*. Cambridge University Press, Washington DC, 2nd editio edition, 1987.
- [25] James Feng, Howard H Hu, and Daniel D Joseph. Direct Simulation of Initial Value Problems for the Motion of Solid Bodies in a Newtonian Fluid . Part 2 . Couette adn Poiseuille Flows. *Journal of Fluid Mechanics*, 277:271–301, 1994.
- [26] J Glimm, J W Grove, X L Li, W Oh, and D H Sharp. A critical analysis of Rayleigh–Taylor growth rates. *Journal of Computational Physics*, 169(2):652–677, 2001.

- [27] Francis H Harlow, J Eddie Welch, et al. Numerical calculation of time-dependent viscous incompressible flow of fluid with free surface. *Physics of fluids*, 8(12):2182, 1965.
- [28] Charles S Peskin. Numerical analysis of blood flow in the heart. *Journal of computational physics*, 25(3):220–252, 1977.
- [29] Salih Ozen Unverdi and Grétar Tryggvason. A front-tracking method for viscous, incompressible, multi-fluid flows. *Journal of computational physics*, 100(1):25–37, 1992.
- [30] G. Tryggvason, B. Bunner, a. Esmaeeli, D. Juric, N. Al-Rawahi, W. Tauber, J. Han, S. Nas, and Y.-J. Jan. A Front-Tracking Method for the Computations of Multiphase Flow. *Journal of Computational Physics*, 169(2):708–759, May 2001.
- [31] Stéphane Popinet and Stéphane Zaleski. A front-tracking algorithm for accurate representation of surface tension. *International Journal for Numerical Methods in Fluids*, 30(6):775–793, 1999.
- [32] David Jacqmin. Calculation of two-phase navier–stokes flows using phase-field modeling. *Journal of Computational Physics*, 155(1):96–127, 1999.
- [33] Cyril W Hirt and Billy D Nichols. Volume of fluid (vof) method for the dynamics of free boundaries. *Journal of computational physics*, 39(1):201–225, 1981.
- [34] D. L. Youngs. Time-Dependent Multi-material Flow with Large Fluid Distortion. In *Numerical Methods for Fluid Dynamics*, pages 273–285. 1982.
- [35] O Ubbink and RI Issa. A method for capturing sharp fluid interfaces on arbitrary meshes. *Journal of Computational Physics*, 153(1):26–50, 1999.
- [36] Ruben Scardovelli and Stéphane Zaleski. Direct numerical simulation of free-surface and interfacial flow. *Annual review of fluid mechanics*, 31(1):567–603, 1999.

- [37] Stanley Osher and James A Sethian. Fronts propagating with curvature-dependent speed: algorithms based on Hamilton-Jacobi formulations. *Journal of computational physics*, 79(1):12–49, 1988.
- [38] J.U. Brackbill, D.B. Kothe, and C. Zemach. A continuum method for modeling surface tension. *Journal of Computational Physics*, 100:335–354, 1992.
- [39] Ronald P Fedkiw, Tariq Aslam, Barry Merriman, and Stanley Osher. A Non-oscillatory Eulerian Approach to Interfaces in Multimaterial Flows (the Ghost Fluid Method). *Journal of Computational Physics*, 152(2):457–492, July 1999.
- [40] Ronald P Fedkiw, Tariq Aslam, and Shaojie Xu. The ghost fluid method for deflagration and detonation discontinuities. *Journal of Computational Physics*, 154(2):393–427, 1999.
- [41] Frederic Gibou, Ronald P. Fedkiw, Li-Tien Cheng, and Myungjoo Kang. A Second-Order-Accurate Symmetric Discretization of the Poisson Equation on Irregular Domains. *Journal of Computational Physics*, 176(1):205–227, February 2002.
- [42] Xu-Dong Liu, Ronald P Fedkiw, and Myungjoo Kang. A boundary condition capturing method for Poisson’s equation on irregular domains. *Journal of Computational Physics*, 160(1):151–178, 2000.
- [43] M. Kang, R. P. Fedkiw, and X. D. Liu. A Boundary Condition Capturing Method for Multiphase Incompressible Flow. *Journal of Scientific Computing*, 15:323–360, 2000.
- [44] Duc Q. Nguyen, Ronald P. Fedkiw, and Myungjoo Kang. A Boundary Condition Capturing Method for Incompressible Flame Discontinuities. *Journal of Computational Physics*, 172(1):71–98, September 2001.
- [45] Xiao-Yong Luo, Ming-Jiu Ni, Alice Ying, and MA Abdou. Numerical modeling for

multiphase incompressible flow with phase change. *Numerical Heat Transfer, Part B: Fundamentals*, 48(5):425–444, 2005.

- [46] Gihun Son and Vijay K. Dhir. A Level Set Method for Analysis of Film Boiling on an Immersed Solid Surface. *Numerical Heat Transfer, Part B: Fundamentals*, 52(2):153–177, June 2007.
- [47] Stanley Osher and Ronald P. Fedkiw. Level Set Methods: An Overview and Some Recent Results. *Journal of Computational Physics*, 169(2):463–502, May 2001.
- [48] Mark Sussman, Emad Fatemi, Peter Smereka, and Stanley Osher. An improved level set method for incompressible two-phase flows. *Computers & Fluids*, 27(5-6):663–680, June 1998.
- [49] Y.C. Chang, T.Y. Hou, B. Merriman, and S. Osher. A Level Set Formulation of Eulerian Interface Capturing Methods for Incompressible Fluid Flows. *Journal of Computational Physics*, 124(2):449–464, 1996.
- [50] Gihun Son. A Numerical Method for Bubble Motion with Phase Change. *Numerical Heat Transfer, Part B: Fundamentals: An International Journal of Computation and Methodology*, 39(5):509–523, 2001.
- [51] A. Bourlioux. A Coupled Level-Set Volume-of-Fluid Algorithm for Tracking Material Interfaces. *Proc. 6th Int. Symp. on Computational Fluid Dynamics*, pages 15–22, 1995.
- [52] Mark Sussman and Elbridge Gerry Puckett. A Coupled Level Set and Volume-of-Fluid Method for Computing 3D and Axisymmetric Incompressible Two-Phase Flows. *Journal of Computational Physics*, 162(2):301–337, August 2000.
- [53] Douglas Enright, Ronald Fedkiw, Joel Ferziger, and Ian Mitchell. A Hybrid Particle Level Set Method for Improved Interface Capturing. *Journal of Computational Physics*, 183(1):83–116, November 2002.

- [54] Zhipeng Qin, Keegan Delaney, Amir Riaz, and Elias Balaras. Topology preserving advection of implicit interfaces on cartesian grids. *Journal of Computational Physics*, 290:219–238, 2015.
- [55] Vinesh H. Gada and Atul Sharma. On a Novel Dual-Grid Level-Set Method for Two-Phase Flow Simulation. *Numerical Heat Transfer, Part B: Fundamentals*, 59(1):26–57, January 2011.
- [56] D. K. Agarwal, S. W. J. Welch, G. Biswas, and F. Durst. Planar Simulation of Bubble Growth in Film Boiling in Near-Critical Water Using a Variant of the VOF Method. *Journal of Heat Transfer*, 126(3):329, 2004.
- [57] Francis H. Harlow and J. Eddie Welch. Numerical Calculation of Time-Dependent Viscous Incompressible Flow of Fluid with Free Surface. *Physics of Fluids*, 8(12):2182, 1965.
- [58] Alexandre Joel Chorin. Numerical solution of incompressible flow problems. *Studies in Numerical Analysis*, 2:64–71, 1968.
- [59] Tariq D. Aslam. A partial differential equation approach to multidimensional extrapolation. *Journal of Computational Physics*, 193(1):349–355, January 2004.
- [60] Olaf Schenk, Matthias Bollhöfer, and Rudolf A. Römer. On large-scale diagonalization techniques for the anderson model of localization. *SIAM Rev.*, 50(1):91–112, February 2008.
- [61] Antoine du Chéné, Chohong Min, and Frédéric Gibou. Second-order accurate computation of curvatures in a level set framework using novel high-order reinitialization schemes. *Journal of Scientific Computing*, 35(2-3):114–131, 2008.
- [62] Guang-Shan Jiang and Danping Peng. Weighted ENO schemes for Hamilton-Jacobi equations. *SIAM Journal on Scientific computing*, 21(6):2126–2143, 2000.

- [63] Mark Sussman, Peter Smereka, and Stanley Osher. A level set approach for computing solutions to incompressible two-phase flow. *Journal of Computational physics*, 114(1):146–159, 1994.
- [64] Vasilios Alexiades. *Mathematical modeling of melting and freezing processes*. CRC Press, 1992.
- [65] LE Scriven. On the dynamics of phase growth. *Chemical Engineering Science*, 10(1):1–13, 1959.
- [66] P J Berenson. Film-boiling heat transfer from a horizontal surface. *Journal of Heat Transfer*, 83(3):351–356, 1961.
- [67] VV Klimenko. Film boiling on a horizontal platenew correlation. *International Journal of Heat and Mass Transfer*, 24(1):69–79, 1981.
- [68] D Banerjee and VK Dhir. Study of subcooled film boiling on a horizontal disc: part 2-experiments. *TRANSACTIONS-AMERICAN SOCIETY OF MECHANICAL ENGINEERS JOURNAL OF HEAT TRANSFER*, 123(2):285–293, 2001.
- [69] Vijay K Dhir. Numerical simulations of pool-boiling heat transfer. *AIChE Journal*, 47(4):813–834, 2001.
- [70] Csaba Horvath, Barry A Solomon, and Jean-Marc Engasser. Measurement of radial transport in slug flow using enzyme tubes. *Industrial & Engineering Chemistry Fundamentals*, 12(4):431–439, 1973.
- [71] DR Oliver and A Young Hoon. 2-phase non-newtonian flow. 2. heat transfer. *Transactions of the Institution of Chemical Engineers and the Chemical Engineer*, 46(4):T116, 1968.
- [72] James A Howard, Patrick A Walsh, and Edmond J Walsh. Prandtl and capillary

effects on heat transfer performance within laminar liquid–gas slug flows. *International Journal of Heat and Mass Transfer*, 54(21):4752–4761, 2011.

- [73] Abhik Majumder, Balkrishna Mehta, and Sameer Khandekar. Local nusselt number enhancement during gas–liquid taylor bubble flow in a square mini-channel: an experimental study. *International Journal of Thermal Sciences*, 66:8–18, 2013.
- [74] Koji Fukagata, Nobuhide Kasagi, Poychat Ua-arayaporn, and Takehiro Himeno. Numerical simulation of gas–liquid two-phase flow and convective heat transfer in a micro tube. *International Journal of Heat and Fluid Flow*, 28(1):72–82, 2007.
- [75] Chidambaram Narayanan and Djamel Lakehal. Two-phase convective heat transfer in miniature pipes under normal and microgravity conditions. *Journal of Heat Transfer*, 130(7):074502, 2008.
- [76] Qunwu He, Yosuke Hasegawa, and Nobuhide Kasagi. Heat transfer modelling of gas–liquid slug flow without phase change in a micro tube. *International Journal of Heat and Fluid Flow*, 31(1):126–136, 2010.
- [77] Raghvendra Gupta, David F Fletcher, and Brian S Haynes. Cfd modelling of flow and heat transfer in the taylor flow regime. *Chemical Engineering Science*, 65(6):2094–2107, 2010.
- [78] Azadeh N Asadolahi, Raghvendra Gupta, Sharon SY Leung, David F Fletcher, and Brian S Haynes. Validation of a cfd model of taylor flow hydrodynamics and heat transfer. *Chemical Engineering Science*, 69(1):541–552, 2012.
- [79] Abhijit Mukherjee and Satish G Kandlikar. Numerical simulation of growth of a vapor bubble during flow boiling of water in a microchannel. *Microfluidics and Nanofluidics*, 1(2):137–145, 2005.

- [80] A Mukherjee. Contribution of thin-film evaporation during flow boiling inside microchannels. *International Journal of Thermal Sciences*, 48(11):2025–2035, 2009.
- [81] YQ Zu, YY Yan, S Gedupudi, TG Karayannidis, and DBR Kenning. Confined bubble growth during flow boiling in a mini-/micro-channel of rectangular cross-section part ii: Approximate 3-d numerical simulation. *International Journal of Thermal Sciences*, 50(3):267–273, 2011.
- [82] Rui Zhuan and Wen Wang. Flow pattern of boiling in micro-channel by numerical simulation. *International Journal of Heat and Mass Transfer*, 55(5):1741–1753, 2012.
- [83] Raghvendra Gupta, David F Fletcher, and Brian S Haynes. On the cfd modelling of taylor flow in microchannels. *Chemical Engineering Science*, 64(12):2941–2950, 2009.
- [84] Youngho Suh, Woorim Lee, and Gihun Son. Bubble dynamics, flow, and heat transfer during flow boiling in parallel microchannels. *Numerical Heat Transfer, Part A: Applications*, 54(4):390–405, 2008.
- [85] Mirco Magnini, B Pulvirenti, and John Richard Thome. Numerical investigation of hydrodynamics and heat transfer of elongated bubbles during flow boiling in a microchannel. *International Journal of Heat and Mass Transfer*, 59:451–471, 2013.
- [86] V Talimi, YS Muzychka, and S Kocabiyik. A review on numerical studies of slug flow hydrodynamics and heat transfer in microtubes and microchannels. *International Journal of Multiphase Flow*, 39:88–104, 2012.
- [87] Thilaksiri Bandara, Nam-Trung Nguyen, and Gary Rosengarten. Slug flow heat transfer without phase change in microchannels: A review. *Chemical Engineering Science*, 126:283–295, 2015.
- [88] FP Bretherton. The motion of long bubbles in tubes. *Journal of Fluid Mechanics*, 10(02):166–188, 1961.

- [89] Pascale Aussillous and David Quéré. Quick deposition of a fluid on the wall of a tube. *Physics of Fluids (1994-present)*, 12(10):2367–2371, 2000.
- [90] Hui Liu, Chippla O Vandu, and Rajamani Krishna. Hydrodynamics of taylor flow in vertical capillaries: flow regimes, bubble rise velocity, liquid slug length, and pressure drop. *Industrial & engineering chemistry research*, 44(14):4884–4897, 2005.
- [91] Michiel T Kreutzer, Freek Kapteijn, Jacob A Moulijn, Chris R Kleijn, and Johan J Heiszwolf. Inertial and interfacial effects on pressure drop of taylor flow in capillaries. *AICHE Journal*, 51(9):2428–2440, 2005.
- [92] Djamel Lakehal, Guillaume Larrignon, and Chidambaram Narayanan. Computational heat transfer and two-phase flow topology in miniature tubes. *Microfluidics and nanofluidics*, 4(4):261–271, 2008.
- [93] G Son, VK Dhir, and N Ramanujapu. Dynamics and heat transfer associated with a single bubble during nucleate boiling on a horizontal surface. *Journal of Heat Transfer*, 121(3):623–631, 1999.
- [94] Han Young Yoon, Seiichi Koshizuka, and Yoshiaki Oka. Direct calculation of bubble growth, departure, and rise in nucleate pool boiling. *International Journal of Multiphase Flow*, 27(2):277–298, 2001.
- [95] G Son, N Ramanujapu, and VK Dhir. Numerical simulation of bubble merger process on a single nucleation site during pool nucleate boiling. *Journal of Heat Transfer*, 124(1):51–62, 2002.
- [96] Abhijit Mukherjee and Satish G Kandlikar. Numerical study of single bubbles with dynamic contact angle during nucleate pool boiling. *International Journal of Heat and Mass Transfer*, 50(1):127–138, 2007.

- [97] Chohong Min and Frédéric Gibou. A second order accurate level set method on non-graded adaptive cartesian grids. *Journal of Computational Physics*, 225(1):300–321, 2007.
- [98] S. Ozen Unverdi and Grétar Tryggvason. Computations of multi-fluid flows. *Physica D: Nonlinear Phenomena*, 60(14):70–83, 1992.
- [99] Howard H Hu. Direct simulation of flows of solid-liquid mixtures. *International Journal of Multiphase Flow*, 22(2):335–352, 1996.
- [100] G Tomar, G Biswas, A Sharma, and S W J Welch. Multimode analysis of bubble growth in saturated film boiling. *Physics of Fluids (1994-present)*, 20(9):92101, 2008.
- [101] Vinesh H. Gada and Atul Sharma. On Derivation and Physical Interpretation of Level Set MethodBased Equations for Two-Phase Flow Simulations. *Numerical Heat Transfer, Part B: Fundamentals*, 56(4):307–322, November 2009.
- [102] G. Tryggvason, a. Esmaeeli, and N. Al-Rawahi. Direct numerical simulations of flows with phase change. *Computers & Structures*, 83(6-7):445–453, February 2005.
- [103] Ronald P Fedkiw, Tariq Aslam, Barry Merriman, and Stanley Osher. A Non-oscillatory Eulerian Approach to Interfaces in Multimaterial Flows (the Ghost Fluid Method). *Journal of Computational Physics*, 152(2):457–492, July 1999.
- [104] S. Osher M. Sussman, P. Smereka. A level set approach for computing solutions to incompressible two-phase flow. *Journal of Computational Physics*, 114:146, 1994.
- [105] Marianne M. Francois, Sharen J. Cummins, Edward D. Dendy, Douglas B. Kothe, James M. Sicilian, and Matthew W. Williams. A balanced-force algorithm for continuous and sharp interfacial surface tension models within a volume tracking framework. *Journal of Computational Physics*, 213(1):141–173, March 2006.

- [106] B. Koren and A. Venis. A fed back level-set method for moving materialvoid interfaces. *Journal of Computational and Applied Mathematics*, 101:131–152, 1999.
- [107] Seungwon Shin and Damir Juric. Modeling Three-Dimensional Multiphase Flow Using a Level Contour Reconstruction Method for Front Tracking without Connectivity. *Journal of Computational Physics*, 180(2):427–470, August 2002.
- [108] N Al-Rawahi and G Tryggvason. Numerical Simulation of Dendritic Solidification with Convection: Two-Dimensional Geometry. *Journal of Computational Physics*, 180(2):471–496, August 2002.
- [109] Xiao-Yong Luo, Ming-Jiu Ni, Alice Ying, and M. a. Abdou. Numerical Modeling for Multiphase Incompressible Flow with Phase Change. *Numerical Heat Transfer, Part B: Fundamentals*, 48(5):425–444, November 2005.
- [110] G Ryskin and L G Leal. Numerical solution of free-boundary problems in fluid mechanics. Part 3. Bubble deformation in an axisymmetric straining flow. *Journal of Fluid Mechanics*, 148(-1):37–43, 1984.
- [111] Edip Can and Andrea Prosperetti. A level set method for vapor bubble dynamics. *Journal of Computational Physics*, 231(4):1533–1552, February 2012.
- [112] G. Ryskin and L. G. Leal. Numerical solution of free-boundary problems in fluid mechanics. Part 1. The finite-difference technique. *Journal of Fluid Mechanics*, 148(-1):1, April 2006.
- [113] Gihun Son. a Level Set Method for Incompressible Two-Fluid Flows With Immersed Solid Boundaries. *Numerical Heat Transfer, Part B: Fundamentals*, 47(5):473–489, April 2005.
- [114] Samuel W.J. Welch. Direct simulation of vapor bubble growth, 1998.

- [115] E Ao Farber and RL Scorah. *Heat transfer to water boiling under pressure*. University of Missouri, 1948.
- [116] P.A.M. Dirac. The lorentz transformation and absolute time. *Physica*, 19(1-12):888–896, 1953.
- [117] R.P Feynman and F.L Vernon Jr. The theory of a general quantum system interacting with a linear dissipative system. *Annals of Physics*, 24:118–173, 1963.
- [118] Woorim Lee and Gihun Son. Numerical simulation of boiling enhancement on a microstructured surface. *International Communications in Heat and Mass Transfer*, 38(2):168–173, 2011.
- [119] Damir Juric and Grétar Tryggvason. Computations of boiling flows. *International Journal of Multiphase Flow*, 24(3):387–410, 1998.
- [120] Bruno Lafaurie, Carlo Nardone, Ruben Scardovelli, Stéphane Zaleski, and Gianluigi Zanetti. Modelling merging and fragmentation in multiphase flows with surfer. *Journal of Computational Physics*, 113(1):134–147, 1994.
- [121] Denis Gueyffier, Jie Li, Ali Nadim, Ruben Scardovelli, and Stéphane Zaleski. Volume-of-fluid interface tracking with smoothed surface stress methods for three-dimensional flows. *Journal of Computational Physics*, 152(2):423–456, 1999.
- [122] S Polonsky, D Barnea, and L Shemer. Averaged and time-dependent characteristics of the motion of an elongated bubble in a vertical pipe. *International Journal of Multiphase Flow*, 25(5):795–812, 1999.
- [123] L Shemer, A Gulitski, and D Barnea. On the turbulent structure in the wake of taylor bubbles rising in vertical pipes. *Physics of Fluids (1994-present)*, 19(3):035108, 2007.
- [124] Youngbae Han, Naoki Shikazono, and Nobuhide Kasagi. The effect of liquid film

evaporation on flow boiling heat transfer in a micro tube. *International Journal of Heat and Mass Transfer*, 55(4):547–555, 2012.

- [125] Anthony M Jacobi and John R Thome. Heat transfer model for evaporation of elongated bubble flows in microchannels. *Journal of Heat Transfer*, 124(6):1131–1136, 2002.
- [126] Alex Scammell and Jungho Kim. Heat transfer and flow characteristics of rising taylor bubbles. *International Journal of Heat and Mass Transfer*, 89:379–389, 2015.
- [127] Wael Salman, Asterios Gavriilidis, and Panagiota Angeli. A model for predicting axial mixing during gas–liquid taylor flow in microchannels at low bodenstein numbers. *Chemical Engineering Journal*, 101(1):391–396, 2004.
- [128] JM Van Baten and R Krishna. Cfd simulations of mass transfer from taylor bubbles rising in circular capillaries. *Chemical Engineering Science*, 59(12):2535–2545, 2004.
- [129] A Mukherjee, SG Kandlikar, and ZJ Edel. Numerical study of bubble growth and wall heat transfer during flow boiling in a microchannel. *International Journal of Heat and Mass Transfer*, 54(15):3702–3718, 2011.
- [130] Poychat Ua-Arayaporn, Koji Fukagata, Nobuhide Kasagi, and Takehiro Himeno. Numerical simulation of gas-liquid two phase convective heat transfer in a micro tube. In *ECI International Conference on Heat Transfer and Fluid Flow in Microscale, Castelvecchio Pascoli, Italy, Sept*, pages 25–30, 2005.
- [131] T Taha and ZF Cui. Hydrodynamics of slug flow inside capillaries. *Chemical Engineering Science*, 59(6):1181–1190, 2004.
- [132] John R Thome, J El Hajal, and A Cavallini. Condensation in horizontal tubes, part 2: new heat transfer model based on flow regimes. *International Journal of Heat and Mass Transfer*, 46(18):3365–3387, 2003.

[133] Bruno Agostini, Matteo Fabbri, Jung E Park, Leszek Wojtan, John R Thome, and Bruno Michel. State of the art of high heat flux cooling technologies. *Heat Transfer Engineering*, 28(4):258–281, 2007.